NASA/TP-2009-214643

Further Development of Ko Displacement Theory for Deformed Shape Predictions of Nonuniform Aerospace Structures

William L. Ko and Van Tran Fleischer
NASA Dryden Flight Research Center
Edwards, California

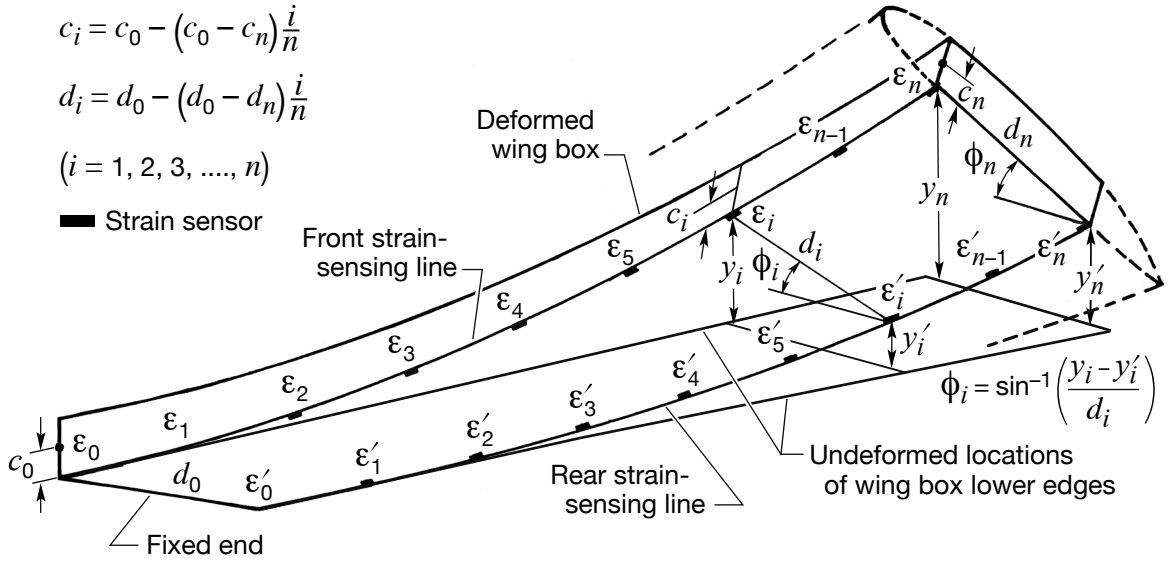

September 2009

NASA STI Program ... in Profile

Since its founding, NASA has been dedicated to the advancement of aeronautics and space science. The NASA scientific and technical information (STI) program plays a key part in helping NASA maintain this important role.

The NASA STI program operates under the auspices of the Agency Chief Information Officer. It collects, organizes, provides for archiving, and disseminates NASA's STI. The NASA STI program provides access to the NASA Aeronautics and Space Database and its public interface, the NASA Technical Report Server, thus providing one of the largest collections of aeronautical and space science STI in the world. Results are published in both non-NASA channels and by NASA in the NASA STI Report Series, which includes the following report types:

- TECHNICAL PUBLICATION. Reports of completed research or a major significant phase of research that present the results of NASA Programs and include extensive data or theoretical analysis. Includes compilations of significant scientific and technical data and information deemed to be of continuing reference value. NASA counterpart of peer-reviewed formal professional papers but has less stringent limitations on manuscript length and extent of graphic presentations.

- TECHNICAL MEMORANDUM. Scientific and technical findings that are preliminary or of specialized interest, e.g., quick release reports, working papers, and bibliographies that contain minimal annotation. Does not contain extensive analysis.

- CONTRACTOR REPORT. Scientific and technical findings by NASA-sponsored contractors and grantees.

- CONFERENCE PUBLICATION. Collected papers from scientific and technical conferences, symposia, seminars, or other meetings sponsored or co-sponsored by NASA.

- SPECIAL PUBLICATION. Scientific, technical, or historical information from NASA programs, projects, and missions, often concerned with subjects having substantial public interest.

- TECHNICAL TRANSLATION. English-language translations of foreign scientific and technical material pertinent to NASA's mission.

Specialized services also include creating custom thesauri, building customized databases, and organizing and publishing research results.

For more information about the NASA STI program, see the following:

- Access the NASA STI program home page at *http://www.sti.nasa.gov*

- E-mail your question via the Internet to help@sti.nasa.gov

- Fax your question to the NASA STI Help Desk at 443-757-5803

- Phone the NASA STI Help Desk at 443-757-5802

- Write to:
  NASA STI Help Desk
  NASA Center for AeroSpace Information
  7115 Standard Drive
  Hanover, MD 21076-1320

NASA/TP-2009-214643

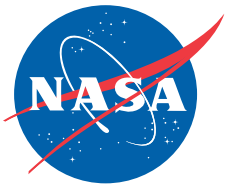

Further Development of Ko Displacement Theory for Deformed Shape Predictions of Nonuniform Aerospace Structures

William L. Ko and Van Tran Fleischer
NASA Dryden Flight Research Center
Edwards, California

National Aeronautics and
Space Administration

Dryden Flight Research Center
Edwards, California 93523-0273

September 2009

The structural shape prediction method described in this report is protected under U.S. Patent No. 7,520,176, issued April 21, 2009. Therefore, those interested in using the method should contact the NASA Innovative Partnership Program Office at the Dryden Flight Research Center for more information.

Cover art: NASA Dryden Flight Research Center, art number 090014.

Available from:

NASA Center for AeroSpace Information
7115 Standard Drive
Hanover, MD 21076-1320
(443) 757-5802

TABLE OF CONTENTS

ABSTRACT

The Ko displacement theory previously formulated for deformed shape predictions of nonuniform beam structures is further developed mathematically. The further-developed displacement equations are expressed explicitly in terms of geometrical parameters of the beam and bending strains at equally spaced strain-sensing stations along the multiplexed fiber-optic sensor line installed on the bottom surface of the beam. The bending strain data can then be input into the displacement equations for calculations of local slopes, deflections, and cross-sectional twist angles for generating the overall deformed shapes of the nonuniform beam. The further-developed displacement theory can also be applied to the deformed shape predictions of nonuniform two-point supported beams, nonuniform panels, nonuniform aircraft wings and fuselages, and so forth. The high degree of accuracy of the further-developed displacement theory for nonuniform beams is validated by finite-element analysis of various nonuniform beam structures. Such structures include tapered tubular beams, depth-tapered unswept and swept wing boxes, width-tapered wing boxes, and double-tapered wing boxes, all under combined bending and torsional loads. The Ko displacement theory, combined with the fiber-optic strain-sensing system, provide a powerful tool for in-flight deformed shape monitoring of unmanned aerospace vehicles by ground-based pilots to maintain safe flights.

NOMENCLATURE

c	half depth of uniform beam (distance from neutral surface to bottom or top surface), in.
CG	center of gravity
c_i	half depth of nonuniform beam at strain-sensing station, x_i (distance from neutral surface to strain-sensing station, x_i), in.
c_n	value of c_i at free end (beam tip) strain-sensing station, x_n, in.
c_n/c_0	beam tip–root depth ratio
$c(x)$	half depth of nonuniform beam at point x, in.
c_0	value of c_i at fixed end (beam root) strain-sensing station, x_0, in.
d	chord-wise distance between two span-wise parallel strain-sensing lines, in.
deg	degree
d_i	chord-wise distance between tapered front and rear strain-sensing stations at $\{x_i, x_i'\}$, in.
E	Young modulus, lb/in^2
e	calculated nonzero deflection error at right fixed end of two-point supported beam, in.
G	shear modulus, lb/in^2
I	moment of inertia, in^4
i	= 0, 1, 2, 3, …, n, strain-sensing station identification number
j	index
l	length of beam, in.
M	bending moment, in-lb
M_i	bending moment at strain-sensing station, x_i, in-lb
n	index associated with the last span-wise strain-sensing station
P	applied load, lb
SPAR	Structural Performance And Resizing
T	applied torque, in-lb
t	thickness of wall, in.
w	width of uniform wing box, in.
w_n	width of wing box tip, in.
w_0	width of wing box root, in.

x, y	Cartesian coordinates (x in beam axial direction, y in vertical direction), in.
x_i	axial coordinate (or symbol) associated with i-th strain-sensing station, in.
y_i	deflection in y-direction at x_i, in.
y_i^B	deflection in y-direction at x_i for two-point supported beam, in.
$y(x)$	deflection in y-direction at axial location, x, in.
α	half of angle, sustained by d, separating two strain-sensing lines on tubular beam, deg
β	wing box swept angle, deg
γ_i	surface shear strain, rad
Δl	$= l/n$, distance between two adjacent strain-sensing stations, in.
ε_i	surface bending strain at strain-sensing station, x_i, in/in.
$\varepsilon(x)$	surface bending strain at axial location, x, in/in.
θ_i	slope of deformed beam at strain-sensing station, x_i, rad or deg
$\theta(x)$	slope of deformed beam at axial location, x, rad or deg
ν	Poisson's ratio
σ_i	axial stress at strain-sensing station, x_i, lb/in^2
$\sigma(x)$	surface bending stress at axial location, x, lb/in^2
ϕ_i	cross-sectional twist angle at axial location, x_i, rad or deg
$( )'$	quantity associated with rear strain-sensing line

INTRODUCTION

Conventional aerospace instrumentation systems, such as those required for in-flight deformed shape monitoring of aircraft, are subject to strict weight and size restrictions. The existing electro-optical flight deflection measurement system (ref. 1) and conventional strain gage measurement system are too heavy (because of strain gage lead wires) for lightweight flying vehicles. The most attractive candidate for an in-flight deformed shape measurement system is the fiber Bragg grating (FBG) sensing system, because the sensing lines are extremely small and lightweight (approximately the size of human hairs), possess excellent flexibility, and can be highly multiplexed with hundreds of sensors located on single fibers at desired sensing intervals.

When these highly multiplexed sensors are installed on beam-like structures (such as aircraft wings), the measured strain data can be input into special algorithms to calculate the deflections and cross-sectional twist angles of the beam-like structure for deformed shape predictions. Special algorithms based on the Ko displacement theory are described in detail in reference 2. In the mathematical formulations, the beam is first discretized into multiple domains. Based on the classical beam theory, the displacement theory (ref. 2) was formulated to predict the deformed shapes (slopes, deflections, and cross-sectional twist angles) of cantilever beams (uniform, tapered, slightly tapered, stepwise tapered) using the fiber-optic measured strain data as inputs.

The Ko displacement equations, combined with the onboard fiber-optic strain-sensing system (called *Method For Real-Time Structure Shape-Sensing,* U.S. Patent No. 7,520,176, issued April 21, 2009; ref. 3), provide a powerful tool for in-flight deformed shape monitoring of unmanned aerospace vehicles by ground-based pilots to maintain safe flights. In addition, the wing shape that is monitored in real time could then be input into the aircraft control system for aeroelastic wing shape control.

In the original formulation of the Ko displacement theory (refs. 2, 3) for nonuniform cantilever beams (for example, tapered, slightly tapered), the displacement equations are written in indicial recursion relationships because of multiple beam domains, and they need to be fully developed into more compact mathematical forms. In this report, the displacement equations for nonuniform beams (cantilever and two-point supported beams) formulated previously (refs. 2, 3) are further developed into more compact mathematical forms so that the beam deflections at each strain-sensing station can be expressed exclusively in terms of inboard geometrical parameters of the beam and inboard surface bending strains. The accuracy of the further-developed displacement theory for nonuniform beams is validated by finite-element analysis of various nonuniform beam structures (tapered tubular beams, such as cantilever and two-point supported beams, depth-tapered unswept and swept wing boxes, width-tapered wing boxes, and double-tapered wing boxes) under different loading conditions.

BASICS OF THE KO DISPLACEMENT THEORY

The formulation of the displacement theories is built upon the classical beam differential equation (elastic curvature of a deformed uniform beam) given by (refs. 4, 5)

$$\frac{d^2y}{dx^2} = \frac{M(x)}{EI} \tag{1}$$

in which y is the vertical deflection, x is the span-wise coordinate, $M(x)$ is the bending moment, E is the Young modulus, and I is the moment of inertia.

At the cross section of the beam, x, the bending moment, $M(x)$ (eq. (1)), induces the bending stress, $\sigma(x)$, at the bottom (or top) fiber of the beam (outermost point from the neutral axis) (refs. 2–5) with the magnitude proportional to $M(x)$ according to

$$\sigma(x) = \frac{M(x)c}{I} \tag{2}$$

in which c is the half depth (distance from the neutral axis to the bottom or top surface) of the uniform beam. The bending stress, $\sigma(x)$, is related to the bending strain, $\varepsilon(x)$, at the same point on the bottom (or top) surface of the beam through Hooke's law as

$$\varepsilon(x) = \frac{\sigma(x)}{E} \tag{3}$$

When equations (2) and (3) are combined, the bending moment, $M(x)$, can be expressed in terms of the bending strain, $\varepsilon(x)$, as

$$M(x) = EI\frac{\varepsilon(x)}{c} \tag{4}$$

In light of equation (4), beam differential equation (1) becomes

$$\frac{d^2y}{dx^2} = \frac{\varepsilon(x)}{c} \tag{5}$$

Note that under the present strain formulation, beam differential equation (5) contains only the half depth of the beam, c, and the bending strain, $\varepsilon(x)$. The flexural rigidity, *EI*, is eliminated.

Beam differential equation (5) for the uniform beam could be used with sufficient accuracy for nonuniform beams for which the cross section is assumed to change gradually (ref. 4, p. 143). Namely, the half depth of the beam, *c*, is no longer constant but is a function of *x* (that is, $c = c(x)$). Hence, for the nonuniform beam, equations (4) and (5) can be modified, respectively, to

$$M(x) = EI\frac{\varepsilon(x)}{c(x)} \tag{6}$$

and

$$\frac{d^2y}{dx^2} = \frac{\varepsilon(x)}{c(x)} \tag{7}$$

The formulation of the Ko displacement theory (ref. 2) for nonuniform beams is based upon modified beam differential equation (7). By discretizing the beam into multiple domains, and assuming $\{ c(x), \varepsilon(x) \}$ to be piecewise linear, one could integrate equation (7) over each domain to yield local slope and deflection equations for generating the overall deformed shape of the beam (ref. 2). The Ko displacement theory requires further mathematical development as described in the subsequent sections.

NONUNIFORM CANTILEVER BEAMS

The nonuniform cantilever beam is defined as a cantilever beam in which the cross section varies slowly along the axis of the beam. This type of beam can also be called a weak nonuniform beam.

Discretization

Figure 1 shows a nonuniform cantilever beam with a length, *l*, and varying depth, $2c(x)$ (for a tubular beam, $c(x)$ is the local radius). Let the fiber-optic strain-sensing line be multiplexed with n +1 (0, 1, 2, 3, …, n) number of equally spaced strain-sensing stations, x_i (i = 0, 1, 2, 3, …, n), at axial locations, $x = x_i$, on the bottom surface of the beam, and let the measured bending strains be denoted by ε_i (i = 0, 1, 2, 3, …, n). Note from figure 1 that the first and last strain-sensing stations, $\{ x_0, x_n \}$, are located at the fixed end ($x = 0$) and at the free end ($x = l$), respectively. The index, i (= 0, 1, 2, 3, …, n), is also used as the identification number of the strain-sensing stations. The nonuniform cantilever beam is now divided into n sections with identical domain length, $\Delta l = l / n$. The nonuniform beam can then be idealized as a piecewise linearly tapered beam (either tapering down or tapering up) between any two adjacent

strain-sensing stations, $\{x_{i-1}, x_i\}$. Under this assumption, the half depth of the beam, $c(x)$, in the region, $x_{i-1} \le x \le x_i$, between the two adjacent strain-sensing stations, $\{x_{i-1}, x_i\}$, can be expressed as a linear function of x as

$$c(x) = c_{i-1} - (c_{i-1} - c_i)\frac{x - x_{i-1}}{\Delta l} \quad ; \quad x_{i-1} \le x \le x_i \tag{8}$$

in which $\{c_{i-1}, c_i\}$ are the values of $c(x)$ at the strain-sensing stations, $\{x_{i-1}, x_i\}$, respectively. Likewise, the bending strain, $\varepsilon(x)$, in the region, $x_{i-1} \le x \le x_i$, between the two adjacent strain-sensing stations, $\{x_{i-1}, x_i\}$, can be assumed to change linearly with x as

$$\varepsilon(x) = \varepsilon_{i-1} - (\varepsilon_{i-1} - \varepsilon_i)\frac{x - x_{i-1}}{\Delta l} \quad ; \quad x_{i-1} \le x \le x_i \tag{9}$$

in which $\{\varepsilon_{i-1}, \varepsilon_i\}$ are the values of $\varepsilon(x)$ at the strain-sensing stations, $\{x_{i-1}, x_i\}$, respectively.

If $c(x)$ is a weak linear function of x (small slope term in eq. (8)), then the bending moment for the nonuniform beam, $M(x) = EI\varepsilon(x)/c(x)$ (eq. (6)), will vary almost linearly between the two adjacent strain-sensing stations, $\{x_{i-1}, x_i\}$, because the higher order terms in the binomial expansion of the denominator, $[c(x)]^{-1}$, can be neglected. This argument may not hold, however, if $c(x)$ is not a weak linear function of x, because the higher order terms in the binomial expansion of the denominator $[c(x)]^{-1}$ must be retained.

For the uniform beam case, $[c(x) = c = \text{constant}]$, the bending moment, $M(x)$, is directly proportional to the bending strain, $\varepsilon(x)$, according to equation (4). Therefore, if the strain, $\varepsilon(x)$, is a linear function of x, then $M(x)$ is also a linear function of x.

Figure 2 shows the slopes, θ_i (i = 0, 1, 2, 3, …, n), and deflections, y_i (i = 0, 1, 2, 3, …, n), at the strain-sensing stations, x_i (i = 0, 1, 2, 3, …, n), on the lower surface of the deformed tubular cantilever beam (using the uniform tubular beam as an example).

Slope Equations

The slope, $\tan\theta(x)$, of the nonuniform beam at the axial location, x, between the two adjacent strain-sensing stations, $x_{i-1} \le x \le x_i$, can be obtained by integrating equation (7) once and enforcing the continuity of slope at the next inboard strain-sensing station, x_{i-1}. Namely,

$$\tan\theta(x) = \underbrace{\int_{x_{i-1}}^{x} \frac{d^2y}{dx^2}\,dx}_{\text{Slope increment}} + \underbrace{\tan\theta_{i-1}}_{\text{Slope at } x_{i-1}} = \int_{x_{i-1}}^{x} \frac{\varepsilon(x)}{c(x)}\,dx + \tan\theta_{i-1} \quad ; \quad x_{i-1} \le x \le x_i \tag{10}$$

in which $\tan\theta_{i-1}$ is the slope at x_{i-1}.

Substituting beam half depth equation (8) and strain equation (9) into slope equation (10), and carrying out the integration to the upper limit, $x = x_i$, causes equation (10) to yield the slope, $\tan\theta_i$ [$\equiv \tan\theta(x_i)$], at the strain-sensing station, x_i, as (see Appendix D of ref. 2)

$$\tan\theta_i = \Delta l\left[\frac{\varepsilon_{i-1}-\varepsilon_i}{c_{i-1}-c_i}+\frac{\varepsilon_{i-1}c_i-\varepsilon_i c_{i-1}}{(c_{i-1}-c_i)^2}\log_e\frac{c_i}{c_{i-1}}\right]+\tan\theta_{i-1} \tag{11}$$

When i = 1, the slope, $\tan\theta_{1-1} = \tan\theta_0$, will be the slope at the left fixed end, which is zero ($\tan\theta_0 = 0$) for the cantilever beam. If the reference left end is simply supported (as in the two-point supported beam case), then the slope, $\tan\theta_0$, is nonzero ($\tan\theta_0 \neq 0$).

Deflection Equations

The deflection, $y(x)$, of the nonuniform beam in the region, $x_{i-1} \le x \le x_i$, between the two adjacent strain-sensing stations, $\{x_{i-1}, x_i\}$, can be obtained by integrating slope equation (10) and enforcing the continuity of deflection at the adjacent inboard strain-sensing station, x_{i-1}. Namely,

$$y(x) = \underbrace{\int_{x_{i-1}}^{x}\tan\theta(x)\,dx}_{\text{Integration of slope}} + \underbrace{y_{i-1}}_{\substack{\text{Deflection}\\ \text{at } x_{i-1}}} = \underbrace{\int_{x_{i-1}}^{x}\int_{x_{i-1}}^{x}\frac{\varepsilon(x)}{c(x)}dx\,dx}_{\text{Deflection increment}} + \underbrace{\int_{x_{i-1}}^{x}\tan\theta_{i-1}dx}_{\substack{\text{Deflection at } x\\ \text{due to } \tan\theta_{i-1}}} + \underbrace{y_{i-1}}_{\substack{\text{Deflection}\\ \text{at } x_{i-1}}} \tag{12}$$

$$(x_{i-1} \le x \le x_i)$$

in which y_{i-1} is the deflection at x_{i-1}.

Carrying out the double and single integrations of deflection equation (12) in light of beam depth equation (8) and strain equation (9), we obtain the deflection, y_i [$\equiv y(x_i)$], at the strain-sensing station, x_i, as (see Appendix D of ref. 2)

$$y_i = (\Delta l)^2\left\{\frac{\varepsilon_{i-1}-\varepsilon_i}{2(c_{i-1}-c_i)}-\frac{\varepsilon_{i-1}c_i-\varepsilon_i c_{i-1}}{(c_{i-1}-c_i)^3}\left[c_i\log_e\frac{c_i}{c_{i-1}}+(c_{i-1}-c_i)\right]\right\}+y_{i-1}+\Delta l\tan\theta_{i-1} \tag{13}$$

When i = 1, the deflection and slope, $\{y_{1-1} = y_0,\ \tan\theta_{1-1} = \tan\theta_0\}$, become the deflection and slope at the reference left fixed end where $\{y_0 = 0, \tan\theta_0 = 0\}$. If the left end is simply supported (as in the two-point supported beam case), the deflection, y_0, is zero ($y_0 = 0$), but the slope, $\tan\theta_0$, is nonzero ($\tan\theta_0 \neq 0$).

FURTHER MATHEMATICAL DEVELOPMENT

Equations (11) and (13) are the recursion formulae. In this section these equations are further developed to more compact mathematical forms expressed explicitly in terms of beam geometry, $\{\Delta l,\ c_i\}$, and bending strains, ε_i (fig. 1).

Slope Equation

Equation (11) is a recursion formula showing that the slope, $\tan\theta_i$, at the strain-sensing station, x_i, is expressed in terms of the slope, $\tan\theta_{i-1}$, at the adjacent inboard strain-sensing station, x_{i-1}. Applying the descending indices relationship causes slope equation (11) to become the summation form as (see Appendix A for details)

$$\tan\theta_i = \Delta l \sum_{j=1}^{i} \left[\frac{\varepsilon_{j-1} - \varepsilon_j}{c_{j-1} - c_j} + \frac{\varepsilon_{j-1} c_j - \varepsilon_j c_{j-1}}{(c_{j-1} - c_j)^2} \log_e \frac{c_j}{c_{j-1}} \right] + \tan\theta_0 \tag{14}$$

in which $\tan\theta_0$ is the slope at the left fixed end (reference strain-sensing station, x_0) and is zero ($\tan\theta_0 \neq 0$). For a simply supported left end (as in the two-point supported beam case), however, the slope, $\tan\theta_0$, is nonzero ($\tan\theta_0 \neq 0$). Note that the slope, $\tan\theta_i$, is determined from the geometrical and strain data evaluated at all the inboard strain-sensing stations ($x_0, x_1, x_2, \ldots, x_i$), including the current strain-sensing station, x_i.

Deflection Equations

Under the present discretization formulation, deflection equation (13) is also a recursion formula showing that the deflection, y_i, at the strain-sensing station, x_i, is expressed in terms of the deflection, y_{i-1}, and the slope, $\tan\theta_{i-1}$, at the adjacent inboard strain-sensing station, x_{i-1}. By applying the successive descending recursion relationships for y_{i-1} in light of equation (13), and writing equation (14) for $\tan\theta_{i-1}$, we could express deflection equation (13) for y_i with two series summations (with different summation limits) containing only the geometrical parameters and bending strains (see Appendix A for derivations). Namely,

$$\begin{aligned} y_i = & \underbrace{(\Delta l)^2 \sum_{j=1}^{i} \left\{ \frac{\varepsilon_{j-1} - \varepsilon_j}{2(c_{j-1} - c_j)} - \frac{\varepsilon_{j-1} c_j - \varepsilon_j c_{j-1}}{(c_{j-1} - c_j)^3} \left[c_j \log_e \frac{c_j}{c_{j-1}} + (c_{j-1} - c_j) \right] \right\}}_{\text{Contributions from deflection terms}} \\ & + \underbrace{(\Delta l)^2 \sum_{j=1}^{i-1} (i-j) \left[\frac{\varepsilon_{j-1} - \varepsilon_j}{c_{j-1} - c_j} + \frac{\varepsilon_{j-1} c_j - \varepsilon_j c_{j-1}}{(c_{j-1} - c_j)^2} \log_e \frac{c_j}{c_{j-1}} \right]}_{\text{Contributions from slope terms}} + y_0 + (i)\Delta l \tan\theta_0 \end{aligned} \tag{15}$$

in which $y_0 = \tan\theta_0 = 0$ at the fixed end (reference strain-sensing station, x_0). For a simply supported left end (as in the two-point supported beam case), however, the slope, $\tan\theta_0$, is nonzero ($\tan\theta_0 \neq 0$). Note that the deflection, y_i, is expressed in terms of the geometrical and strain data evaluated at all the inboard strain-sensing stations ($x_0, x_1, x_2, \ldots, x_i$), including the current strain-sensing station, x_i.

After grouping the terms, we can rewrite equation (15) in an alternative form (see Appendix A for details) as

$$y_i = (\Delta l)^2 \sum_{j=1}^{i} \left\{ [2(i-j)+1] \frac{\varepsilon_{j-1} - \varepsilon_j}{2(c_{j-1} - c_j)} - \frac{\varepsilon_{j-1} c_j - \varepsilon_j c_{j-1}}{(c_{j-1} - c_j)^3} \left[c_j \log_e \frac{c_j}{c_{j-1}} + (c_{j-1} - c_j) \right] \right\}$$
$$+ (\Delta l)^2 \sum_{j=1}^{i-1} (i-j) \left[\frac{\varepsilon_{j-1} c_j - \varepsilon_j c_{j-1}}{(c_{j-1} - c_j)^2} \log_e \frac{c_j}{c_{j-1}} \right] + y_0 + (i) \Delta l \tan\theta_0 \tag{16}$$

in which $y_0 = \tan\theta_0 = 0$ at the fixed end (reference strain-sensing station, x_0).

By inputting the geometrical parameters of the beam and the bending strain data into deflection equation (16), we can calculate the deflection of the beam, y_i, at any strain-sensing station, x_i. Therefore, the overall deformed shape of the nonuniform cantilever beam can be generated without the need to know the flexural rigidity of the beam, *EI*. The ability to generate deformed shapes without this information is a powerful characteristic of the Ko displacement theory, because it does not require the tedious and time-consuming calculations of the moment of inertia *I*(*x*), which changes along the span of a complex beam-like structure such as an aircraft wing.

Note that the fixed-end condition, $y_0 = \tan\theta_0 = 0$, will cause the calculated deflection, y_i (or slope, $\tan\theta_i$), to be relative to the tangent line passing through the reference strain-sensing station, x_0, at the fixed end. Thus, deflection equation (16) is applicable to both stationary and moving cantilever beams such as aircraft wings during flight.

Furthermore, deflection equation (16) is formulated for the nonuniform cantilever beam under lateral loading only (bending). If the beam is also subjected to axial loading, the measured strains, ε_i (i = 0, 1, 2, 3, …, n), will contain both bending and axial-load strain components. To remove the axial-load strain components, an additional strain-sensing line is needed on the upper surface along the axis of the beam. If the neutral axis is located at the half depth of the beam, the axial-load strain components can be removed by averaging the magnitudes of the lower and upper surface strains measured at the same strain-sensing cross section to yield the true magnitude of the bending strains.

Limit–Case Mathematical Problems

The mathematical forms of slope equation (14) and deflection equation (16) cannot be applied directly to the uniform beam, because at the limit of ($c_{i-1} = c_i$), the logarithmic terms and the denominators with ($c_{i-1} - c_i$) factors in equations (14) and (16) will go to zero (that is, $\log_e(c_i/c_{i-1}) = 0$, $c_{i-1} - c_i = 0$), causing equations (14) and (16) to be indeterminate. The way to circumvent this limit-case mathematical problem is to first consider the case of a slightly nonuniform cantilever beam and use the perturbation method to expand the logarithmic terms in series form. The resulting series expansion will contain ($c_{i-1} - c_i$) factors in the numerators, which will cancel out the ($c_{i-1} - c_i$) factors in the denominators. Thus, the modified mathematical forms for equations (14) and (16) will be able to degenerate into the limit-

case expressions for uniform beams, ($c_{i-1} = c_i$). The modified slope and deflection equations for slightly nonuniform cantilever beams are derived in the subsequent sections.

SLIGHTLY NONUNIFORM CANTILEVER BEAMS

When the cantilever beam is slightly tapered (that is, $(c_i/c_{i-1}) \to 1$), the logarithmic terms in the slope and deflection equations (eqs. (14) and (16)) will approach zero (that is, $\log_e(c_i/c_{i-1}) \to 0$). Therefore, the perturbation method must be used to expand the logarithmic term, $\log_e(c_i/c_{i-1})$, in the neighborhood of $(c_i/c_{i-1}) \approx 1$ to obtain nonzero mathematical expressions, so that the slope and deflection equations can degenerate into those for the uniform cantilever beam case, $(c_i/c_{i-1}) = 1$.

Slope Equations

For a slightly tapered beam, the logarithmic term, $\log_e(c_i/c_{i-1})$, in slope equation (11) can be expanded in the neighborhood of $(c_i/c_{i-1}) \approx 1$ (that is, $\log_e(c_i/c_{i-1}) \approx 0$). Carrying out the expansion up to the second-order terms in $(c_{i-1} - c_i)^2$ causes the logarithmic term, $\log_e(c_i/c_{i-1})$, to take on the following form as c_i approaches c_{i-1} $[(c_i/c_{i-1}) \to 1]$ (see Appendix B for details of mathematical expansions; refs. 2, 6):

$$\log_e \frac{c_i}{c_{i-1}} \approx \frac{c_{i-1} - c_i}{2c_{i-1}^2}(c_i - 3c_{i-1}) \quad ; \quad \frac{c_i}{c_{i-1}} \to 1 \tag{17}$$

Substitution of equation (17) into slope equation (11) yields the following slope equation for the slightly nonuniform cantilever beam (ref. 2), with the ($c_{i-1} - c_i$) factor in the denominators eliminated:

$$\tan\theta_i = \frac{\Delta l}{2c_{i-1}}\left[\left(2 - \frac{c_i}{c_{i-1}}\right)\varepsilon_{i-1} + \varepsilon_i\right] + \tan\theta_{i-1} \quad ; \quad c_{i-1} \to c_i \tag{18}$$

Applying the descending recursion relationship causes slope equation (18) to become

$$\tan\theta_i = \frac{\Delta l}{2}\sum_{j=1}^{i}\frac{1}{c_{j-1}}\left[\left(2 - \frac{c_j}{c_{j-1}}\right)\varepsilon_{j-1} + \varepsilon_j\right] + \tan\theta_0 \quad ; \quad c_{i-1} \to c_i \tag{19}$$

Note that slope equations (18) and (19) do not contain the ($c_{i-1} - c_i$) factor and can now be used for the limit case ($c_{i-1} = c_i$) of the uniform beam.

Deflection Equations

When the beam becomes slightly tapered (that is, $c_i \to c_{i-1}$), the term, $\left[c_i \log_e(c_i/c_{i-1}) + (c_{i-1} - c_i)\right]$, in equation (13) can be expanded in the neighborhood of $(c_i/c_{i-1}) \approx 1$ (that is, $\log_e(c_i/c_{i-1}) \approx 0$). Carrying out the expansion up to the third-order terms in $(c_{i-1} - c_i)^3$ causes the term, $\left[c_i \log_e(c_i/c_{i-1}) + (c_{i-1} - c_i)\right]$, to take on the following form as c_i approaches $c_{i-1}[(c_i/c_{i-1}) \to 1]$ (see Appendix B for details of mathematical expansions; refs. 2, 6):

$$\left[c_i \log_e \frac{c_i}{c_{i-1}} + (c_{i-1} - c_i)\right] \approx \frac{(c_{i-1} - c_i)^2}{6c_{i-1}}\left[3 + \frac{(c_{i-1} - c_i)}{c_{i-1}}\right] \quad ; \quad \frac{c_i}{c_{i-1}} \to 1 \tag{20}$$

In light of equation (20), deflection equation (13) becomes

$$y_i = \frac{(\Delta l)^2}{6c_{i-1}}\left[\left(3 - \frac{c_i}{c_{i-1}}\right)\varepsilon_{i-1} + \varepsilon_i\right] + y_{i-1} + \Delta l \tan\theta_{i-1} \quad ; \quad \frac{c_i}{c_{i-1}} \to 1 \tag{21}$$

which contains no $(c_{i-1} - c_i)$ factor in the denominators.

Applying the descending recursion relationship of equation (21) for y_{i-1}, and writing slope equation (19) for $\tan\theta_{i-1}$ causes deflection equation (21) to take on a form that has two series summations (see Appendix C), as

$$y_i = \underbrace{\frac{(\Delta l)^2}{6}\sum_{j=1}^{i}\frac{1}{c_{j-1}}\left[\left(3 - \frac{c_j}{c_{j-1}}\right)\varepsilon_{j-1} + \varepsilon_j\right]}_{\text{Contributions from deflection terms}} + \underbrace{\frac{(\Delta l)^2}{2}\sum_{j=1}^{i-1}\frac{(i-j)}{c_{j-1}}\left[\left(2 - \frac{c_j}{c_{j-1}}\right)\varepsilon_{j-1} + \varepsilon_j\right]}_{\text{Contributions from slope terms}} + y_0 + (i)\Delta l \tan\theta_0 \tag{22}$$

in which $y_0 = \tan\theta_0 = 0$ at the fixed end (reference strain-sensing station, x_0) of the cantilever beam. Note from equation (22) that the two summation upper limits are different.

Through grouping similar terms in the two series summations, we can write equation (22) in a final compact form consisting of only one series summation (see the derivation in Appendix C). Namely,

$$y_i = \frac{(\Delta l)^2}{6}\sum_{j=1}^{i}\frac{1}{c_{j-1}}\left\{\left[3(2j-1) - (3j-2)\frac{c_{i-j+1}}{c_{i-j}}\right]\varepsilon_{i-j} + (3j-2)\varepsilon_{i-j+1}\right\} + y_0 + (i)\Delta l \tan\theta_0 \tag{23}$$

In equation (23), $y_0 = \tan\theta_0 = 0$ for the cantilever beam; therefore, the terms, $y_0 + (i)\Delta l \tan\theta_0$, can be dropped. The $y_0 + (i)\Delta l \tan\theta_0$ terms are purposely kept, however, to make equation (23) applicable to other

beam cases, such as simply supported beams, for which $\{y_0 = 0, \tan\theta_0 \neq 0\}$ at the reference strain-sensing station, x_0 (see the section entitled, "Two-Point Supported Beams"). Note that equation (23) is applicable to both stationary and moving cantilever beams (for example, airborne aircraft wings), because the deflection, y_i, calculated from equation (23) is relative to the tangent line ($\tan\theta_0 = 0$) stemming from the reference strain-sensing station, x_0, which can be either stationary or moving (fig. 2).

For easy visualization of the functional progression with ascending indices, equation (23) can be written out explicitly for different indices, *i* (= 1,2,3, …, *n*), as

$$y_1 = \frac{(\Delta l)^2}{6c_0}\left[\left(3 - \frac{c_1}{c_0}\right)\varepsilon_0 + \varepsilon_1\right] + y_0 + \Delta l \tan\theta_0 \tag{23a}$$

$$y_2 = \frac{(\Delta l)^2}{6}\left\{\frac{1}{c_1}\left[\left(3 - \frac{c_2}{c_1}\right)\varepsilon_1 + \varepsilon_2\right] + \frac{1}{c_0}\left[\left(9 - 4\frac{c_1}{c_0}\right)\varepsilon_0 + 4\varepsilon_1\right]\right\} + y_0 + 2\Delta l \tan\theta_0 \tag{23b}$$

$$y_3 = \frac{(\Delta l)^2}{6}\left\{\frac{1}{c_2}\left[\left(3 - \frac{c_3}{c_2}\right)\varepsilon_2 + \varepsilon_3\right] + \frac{1}{c_1}\left[\left(9 - 4\frac{c_2}{c_1}\right)\varepsilon_1 + 4\varepsilon_2\right] + \frac{1}{c_0}\left[\left(15 - 7\frac{c_1}{c_0}\right)\varepsilon_0 + 4\varepsilon_1\right]\right\} + y_0 + 3\Delta l \tan\theta_0 \tag{23c}$$

$$y_4 = \frac{(\Delta l)^2}{6}\left\{\frac{1}{c_3}\left[\left(3 - \frac{c_4}{c_3}\right)\varepsilon_3 + \varepsilon_4\right] + \frac{1}{c_2}\left[\left(9 - 4\frac{c_3}{c_2}\right)\varepsilon_2 + 4\varepsilon_3\right] + \frac{1}{c_1}\left[\left(15 - 7\frac{c_2}{c_1}\right)\varepsilon_1 + 7\varepsilon_2\right] + \frac{1}{c_0}\left[\left(21 - 10\frac{c_1}{c_0}\right)\varepsilon_0 + 10\varepsilon_1\right]\right\} + y_0 + 4\Delta l \tan\theta_0 \tag{23d}$$

$$y_5 = \frac{(\Delta l)^2}{6}\left\{\frac{1}{c_4}\left[\left(3 - \frac{c_5}{c_4}\right)\varepsilon_4 + \varepsilon_5\right] + \frac{1}{c_3}\left[\left(9 - 4\frac{c_4}{c_3}\right)\varepsilon_3 + 4\varepsilon_4\right] + \frac{1}{c_2}\left[\left(15 - 7\frac{c_3}{c_2}\right)\varepsilon_2 + 7\varepsilon_3\right] + \frac{1}{c_1}\left[\left(21 - 10\frac{c_2}{c_1}\right)\varepsilon_1 + 10\varepsilon_2\right] + \frac{1}{c_0}\left[\left(27 - 13\frac{c_1}{c_0}\right)\varepsilon_0 + 13\varepsilon_1\right]\right\} + y_0 + 5\Delta l \tan\theta_0 \tag{23e}$$

……

$$y_n = \frac{(\Delta l)^2}{6}\sum_{j=1}^{n}\frac{1}{c_{n-j}}\left\{\left[3(2j-1) - (3j-2)\frac{c_{n-j+1}}{c_{n-j}}\right]\varepsilon_{n-j} + (3j-2)\varepsilon_{n-j+1}\right\} + y_0 + n\Delta l \tan\theta_0 \tag{23f}$$

in which the fixed-end condition, $y_0 = \tan\theta_0 = 0$, holds.

Equation (23) explicitly shows that the deflection, y_i, at the strain-sensing station, x_i, is the function of the inboard half depth of the beam ($c_0, c_1, c_2, \ldots, c_i$) and the associated inboard strains ($\varepsilon_0, \varepsilon_1, \varepsilon_2, \ldots, \varepsilon_i$),

including the values of $\{c_i, \varepsilon_i\}$ at the current strain-sensing station, x_i, in which the deflection, y_i, is evaluated. By inputting the geometry of the beam and the measured strain data into deflection equation (23), we can calculate the deflection, y_i, at any strain-sensing station and thereby generate the deformed shape of the slightly nonuniform cantilever beam such as an aircraft wing. Note that deflection equation (23), developed for the slightly nonuniform beam, can now be used for the uniform beam case by setting $c_i = c_{i-1} = c$ as a limit case without creating the mathematical breakdown problem encountered in deflection equations (15) and (16).

UNIFORM CANTILEVER BEAMS

When the nonuniformity of the beam diminishes (that is, $c_i = c_{i-1} = c$; fig. 2), slope equations (18) and (19) and deflection equations (21) and (23), developed for the slightly nonuniform cantilever beam, can degenerate into the limit forms for the uniform cantilever beam.

Slope Equations

For the limit case of a uniform beam, $c_i = c_{i-1} = c$, slope equations (18) and (19) developed for the slightly nonuniform cantilever beam degenerate, respectively, into the following limit forms for the uniform cantilever beam:

$$\tan\theta_i = \frac{\Delta l}{2c}(\varepsilon_{i-1} + \varepsilon_i) + \tan\theta_{i-1} \tag{24}$$

$$\tan\theta_i = \frac{\Delta l}{2c}\sum_{j=1}^{i}(\varepsilon_{j-1} + \varepsilon_j) + \tan\theta_0 \tag{25}$$

Deflection Equations

Also, as the nonuniformity of the beam diminishes (that is, $c_i = c_{i-1} = c$), deflection equations (21) and (23) for the slightly nonuniform cantilever beam degenerate, respectively, into limit forms for the uniform cantilever beam as

$$y_i = \frac{(\Delta l)^2}{6c}(2\varepsilon_{i-1} + \varepsilon_i) + y_{i-1} + \Delta l \tan\theta_{i-1} \tag{26}$$

and

$$y_i = \frac{(\Delta l)^2}{6c}\sum_{j=1}^{i}\left[(3j-1)\varepsilon_{i-j} + (3j-2)\varepsilon_{i-j+1}\right] + y_0 + (i)\Delta l \tan\theta_0 \tag{27}$$

in which $y_0 = \tan\theta_0 = 0$ holds at the left fixed end.

After grouping the strain terms of identical indices, we can modify equation (27) into the following more compact form (see details of derivation in Appendix D):

$$y_i = \frac{(\Delta l)^2}{6c}\left[(3i-1)\varepsilon_0 + 6\sum_{j=1}^{i-1}(i-j)\varepsilon_j + \varepsilon_i\right] + y_0 + (i)\Delta l\tan\theta_0 \tag{28}$$

Equation (28) can be written out explicitly for different indices, i (= 1, 2, 3, …, n), so that the functional progression of equation (28) with the increasing value of i can easily be seen:

$$y_1 = \frac{(\Delta l)^2}{6c}(2\varepsilon_0 + \varepsilon_1) + y_0 + \Delta l\tan\theta_0 \tag{28a}$$

$$y_2 = \frac{(\Delta l)^2}{6c}(5\varepsilon_0 + 6\varepsilon_1 + +\varepsilon_2) + y_0 + 2\Delta l\tan\theta_0 \tag{28b}$$

$$y_3 = \frac{(\Delta l)^2}{6c}\left[8\varepsilon_0 + 6(2\varepsilon_1 + \varepsilon_2) + \varepsilon_3\right] + y_0 + 3\Delta l\tan\theta_0 \tag{28c}$$

$$y_4 = \frac{(\Delta l)^2}{6c}\left[11\varepsilon_0 + 6(3\varepsilon_1 + 2\varepsilon_2 + \varepsilon_3) + \varepsilon_4\right] + y_0 + 4\Delta l\tan\theta_0 \tag{28d}$$

$$y_5 = \frac{(\Delta l)^2}{6c}\left[14\varepsilon_0 + 6(4\varepsilon_1 + 3\varepsilon_2 + 2\varepsilon_3 + \varepsilon_4) + \varepsilon_5\right] + y_0 + 5\Delta l\tan\theta_0 \tag{28e}$$

……

$$y_n = \frac{(\Delta l)^2}{6c}\left[(3n-1)\varepsilon_0 + 6\sum_{j=1}^{n-1}(n-j)\varepsilon_j + \varepsilon_n\right] + y_0 + n\Delta l\tan\theta_0 \tag{28f}$$

If the terms, y_0 and $\Delta l\tan\theta_0$, are removed, then deflection equation (28f) will be identical to deflection equation (12e) of reference 2 for the uniform cantilever beam. Equation (28) explicitly shows that the deflection, y_i, at the strain-sensing station, x_i, is obtained by summing up only the inboard strains ($\varepsilon_0, \varepsilon_1, \varepsilon_2, \ldots, \varepsilon_i$), including the strain, ε_i, at the current strain-sensing station, x_i.

Relative Magnitude of Strain Terms

The tip deflection, y_n, expressed in equation (28f) is the summation of the strain data obtained at all the inboard strain-sensing stations. This section examines the relative magnitude of those strain terms, because each strain term has a different coefficient. The example used is the classical uniform cantilever beam under

tip vertical load, P. For this case, the bending strain, $\varepsilon(x)$, is a linearly decreasing function of the axial coordinate, x, and becomes zero at the beam tip (refs. 4, 5). Namely,

$$\varepsilon(x) = \left(1 - \frac{x}{l}\right)\varepsilon_0 \tag{29}$$

in which l is the length of the beam, and ε_0 is the maximum bending strain at the fixed end ($x = x_0$). Based on the strain function given in equation (29), the beam tip deflections, y_n (eq. (28f)), for different values of n can be calculated as follows (see Appendix E for details):

For n = 1:

$$y_1 = \frac{(\Delta l)^2}{6c}(2\varepsilon_0 + \varepsilon_1) = \frac{l^2}{3c}\varepsilon_0 \tag{30a}$$

For n = 2:

$$\begin{aligned} y_2 &= \frac{(\Delta l)^2}{6c}\left(5\varepsilon_0 + 6\varepsilon_1 + \varepsilon_2\right) \\ &= \frac{l^2}{3c}\varepsilon_0\left(\underbrace{0.625}_{\text{maximum}} + 0.375 + 0\right) = \frac{l^2}{3c}\varepsilon_0 \end{aligned} \tag{30b}$$

For n = 4:

$$\begin{aligned} y_4 &= \frac{(\Delta l)^2}{6c}\left[11\varepsilon_0 + 6\left(3\varepsilon_1 + 2\varepsilon_2 + \varepsilon_3\right) + \varepsilon_4\right] \\ &= \frac{l^2}{3c}\varepsilon_0\left(0.34375 + \underbrace{0.421875}_{\text{maximum}} + 0.1875 + 0.046875 + 0\right) = \frac{l^2}{3c}\varepsilon_0 \end{aligned} \tag{30c}$$

For n = 8:

$$\begin{aligned} y_8 &= \frac{(\Delta l)^2}{6c}\left[23\varepsilon_0 + 6\left(7\varepsilon_1 + 6\varepsilon_2 + 5\varepsilon_3 + 4\varepsilon_4 + 3\varepsilon_5 + 2\varepsilon_6 + \varepsilon_7\right) + \varepsilon_8\right] \\ &= \frac{l^2}{3c}\varepsilon_0\left(0.17969 + \underbrace{0.28711}_{\text{maximum}} + 0.21094 + 0.14648 + 0.09375 + +0.05273 + 0.02344 + 0.00586 + 0\right) \\ &= \frac{l^2}{3c}\varepsilon_0 \end{aligned} \tag{30d}$$

In equations (30b)–(30d), the dominant terms are underlined and labeled, “maximum.”

Figure 3 compares the relative magnitude of the strain terms, inside the brackets of equations (30a)–(30d), for different values of *n*. For *n* = 1–2, the maximum strain term is located at the fixed end (x_0). When *n* is greater than 2 ($n > 2$), the maximum strain term shifts toward the next outboard strain-sensing station, x_1 , which becomes the most dominant strain-sensing station. Thus, the accuracy of measured strain at the dominant strain-sensing station greatly affects the accuracy of the calculated beam deflections using equation (28).

TWO-POINT SUPPORTED BEAMS

For the case of a nonuniform cantilever beam, the fixed end ($y_0 = \tan\theta_0 = 0$) is located at the left-hand side at the reference strain-sensing station, x_0. For a two-point supported beam (simple beam), the two ends can be under any support condition (fixed, simply supported, or elastically supported).

Left End Simply Supported

For a simple beam with a simply supported left end, the deflection is zero ($y_0 = 0$), but the slope is nonzero ($\tan\theta_0 \neq 0$). If deflection equation (23) ($y_0 = \tan\theta_0 = 0$) for the cantilever beam is used to calculate the deflection curve of the simple beam case, the deflection curve will have a zero slope ($\tan\theta_0 = 0$) at the left support, and a maximum deflection ($y_n \neq 0$) at the right end (deflection curve at position A, fig. 4). Thus, to apply cantilever beam deflection equation (23) for the simple beam case, the unknown slope, $\tan\theta_0$, at the left support point must be determined first. By setting the right-end deflection, y_n, to zero ($y_n = 0$) in equation (23f), we can determine the unknown slope, $\tan\theta_0$, at the simply supported left end as

$$\tan\theta_0 = -\frac{\Delta l}{6n}\sum_{j=1}^{n}\frac{1}{c_{j-1}}\left\{\left[3(2j-1)-(3j-2)\frac{c_{n-j+1}}{c_{n-j}}\right]\varepsilon_{n-j}+(3j-2)\varepsilon_{n-j+1}\right\} \equiv -\frac{1}{n\Delta l}y_n \tag{31}$$

in which the y_n is the deflection of the cantilever beam tip given by

$$y_n = \underbrace{\frac{(\Delta l)^2}{6}\sum_{j=1}^{n}\frac{1}{c_{j-1}}\left\{\left[3(2j-1)-(3j-2)\frac{c_{n-j+1}}{c_{n-j}}\right]\varepsilon_{n-j}+(3j-2)\varepsilon_{n-j+1}\right\}}_{\text{Equation (23-f); } y_0=\tan\theta_0=0} \tag{32}$$

which is equation (23f) with the terms, $y_0 + n\Delta l \tan\theta_0$, removed, because $y_0 = \tan\theta_0 = 0$ for the cantilever beam.

With $\tan\theta_0$ determined in equation (31), deflection equation (23) for the cantilever beam can be modified to calculate the deflection, y_i^B, of the simple beam with a simply supported left end (the right end can be under any support condition) as

$$y_i^B = \underbrace{\frac{(\Delta l)^2}{6}\sum_{j=1}^{i}\frac{1}{c_{j-1}}\left\{\left[3(2j-1)-(3j-2)\frac{c_{i-j+1}}{c_{i-j}}\right]\varepsilon_{i-j}+(3j-2)\varepsilon_{i-j+1}\right\}}_{y_i\,[\text{equation (23)};\ y_0=\tan\theta_0=0]} - \underbrace{\frac{i}{n}y_n}_{\text{Shift factor}} \tag{33}$$

In equation (33), the last term, $(i/n)y_n$ (i = 1, 2, 3, …, n), is a linearly increasing shifting factor (with increasing i) for vertical downward shifting of the cantilever beam deflection curve from position A to position B, to convert it into the simple beam deflection curve (fig. 4; zero shift at the left end). Namely, the downward shifting is equivalent to the clockwise rotation of the inclined reference line 0A, with respect to the left support point 0, by θ_0 deg to the horizontal position 0B with the length slightly shrunk (fig. 4). For easy visualization of the functional progression with increasing i, equation (33) is written out for different strain-sensing stations as

$$y_1^B = \frac{(\Delta l)^2}{6c_0}\left[\left(3-\frac{c_1}{c_0}\right)\varepsilon_0+\varepsilon_1\right]-\frac{1}{n}y_n \tag{33a}$$

$$y_2^B = \frac{(\Delta l)^2}{6}\left\{\frac{1}{c_1}\left[\left(3-\frac{c_2}{c_1}\right)\varepsilon_1+\varepsilon_2\right]+\frac{1}{c_0}\left[\left(9-4\frac{c_1}{c_0}\right)\varepsilon_0+4\varepsilon_1\right]\right\}-\frac{2}{n}y_n \tag{33b}$$

$$y_3^B = \frac{(\Delta l)^2}{6}\left\{\frac{1}{c_2}\left[\left(3-\frac{c_3}{c_2}\right)\varepsilon_2+\varepsilon_3\right]+\frac{1}{c_1}\left[\left(9-4\frac{c_2}{c_1}\right)\varepsilon_1+4\varepsilon_2\right]+\frac{1}{c_0}\left[\left(15-7\frac{c_1}{c_0}\right)\varepsilon_0+4\varepsilon_1\right]\right\}-\frac{3}{n}y_n \tag{33c}$$

$$\begin{aligned} y_4^B = \frac{(\Delta l)^2}{6}\Bigg\{&\frac{1}{c_3}\left[\left(3-\frac{c_4}{c_3}\right)\varepsilon_3+\varepsilon_4\right]+\frac{1}{c_2}\left[\left(9-4\frac{c_3}{c_2}\right)\varepsilon_2+4\varepsilon_3\right]+\frac{1}{c_1}\left[\left(15-7\frac{c_2}{c_1}\right)\varepsilon_1+7\varepsilon_2\right]\\ &+\frac{1}{c_0}\left[\left(21-10\frac{c_1}{c_0}\right)\varepsilon_0+10\varepsilon_1\right]\Bigg\}-\frac{4}{n}y_n \end{aligned} \tag{33d}$$

$$\begin{aligned} y_5^B = \frac{(\Delta l)^2}{6}\Bigg\{&\frac{1}{c_4}\left[\left(3-\frac{c_5}{c_4}\right)\varepsilon_4+\varepsilon_5\right]+\frac{1}{c_3}\left[\left(9-4\frac{c_4}{c_3}\right)\varepsilon_3+4\varepsilon_4\right]+\frac{1}{c_2}\left[\left(15-7\frac{c_3}{c_2}\right)\varepsilon_2+7\varepsilon_3\right]\\ &+\frac{1}{c_1}\left[\left(21-10\frac{c_2}{c_1}\right)\varepsilon_1+10\varepsilon_2\right]+\frac{1}{c_0}\left[\left(27-13\frac{c_1}{c_0}\right)\varepsilon_0+13\varepsilon_1\right]\Bigg\}-\frac{5}{n}y_n \end{aligned} \tag{33e}$$

……

$$y_n^B = \frac{(\Delta l)^2}{6}\sum_{j=1}^{n}\frac{1}{c_{j-1}}\left\{\left[3(2j-1)-(3j-2)\frac{c_{n-j+1}}{c_{n-j}}\right]\varepsilon_{n-j}+(3j-2)\varepsilon_{n-j+1}\right\}-\frac{n}{n}y_n=0 \tag{33f}$$

If the right end is also simply supported, the right-end slope, $\tan\theta_n$, at the strain-sensing station, x_n, is nonzero ($\tan\theta_n \neq 0$), and slope equation (19) can be used to determine the unknown right-end slope, $\tan\theta_n$, in terms of the left-end slope, $\tan\theta_0$, calculated from equation (32) as

$$\begin{aligned}\tan\theta_n &= \frac{\Delta l}{2}\sum_{j=1}^{n}\frac{1}{c_{j-1}}\left[\left(2-\frac{c_j}{c_{j-1}}\right)\varepsilon_{j-1}+\varepsilon_j\right]+\tan\theta_0 \\ &= \frac{\Delta l}{2}\sum_{j=1}^{n}\frac{1}{c_{j-1}}\left[\left(2-\frac{c_j}{c_{j-1}}\right)\varepsilon_{j-1}+\varepsilon_j\right]-\frac{1}{n\Delta l}y_n\end{aligned} \tag{34}$$

Note that the right-end slope, $\tan\theta_n$, does not appear in deflection equation (33); therefore, the knowledge of $\tan\theta_n$ is not needed in the deflection calculations.

Left End Fixed

Deflection equation (23) for the nonuniform cantilever beam is also applicable to the nonuniform simple beam with the left end fixed (the right end can be either fixed or simply supported). The deflection, y_n, at the right end, calculated from cantilever beam deflection equation (23f) with exact strain inputs, theoretically should be zero. If the calculated right-end deflection, y_n, should show a small nonzero error, e ($y_n = e << 1$), however, then deflection equation (23) for the cantilever beam ($y_0 = \tan\theta_0 = 0$) must be corrected for the present case as

$$y_i^B = \underbrace{\frac{(\Delta l)^2}{6}\sum_{j=1}^{i}\frac{1}{c_{j-1}}\left\{\left[3(2j-1)-(3j-2)\frac{c_{i-j+1}}{c_{i-j}}\right]\varepsilon_{i-j}+(3j-2)\varepsilon_{i-j+1}\right\}}_{y_i\ [\text{equation (23)};\ y_0=\tan\theta_0=0]} - \underbrace{\frac{i}{n}e}_{\substack{\text{Correction}\\ \text{term}}} \tag{35}$$

Similar to figure 4, equation (35) is used to proportionally shift the calculated deflection curve slightly downward or upward depending on the sign of e to make the right-end deflection zero ($y_n^B = 0$). Keep in mind that the degree of shifting for the present case is minuscule compared with the previous case (left end simply supported, eq. (33)).

TWO–LINE STRAIN–SENSING SYSTEM

The two-line strain-sensing system proposed by Ko (ref. 2) is a powerful method for simultaneously monitoring the bending and torsional deformation of nonuniform cantilever beams under combined bending and torsion. The two-line strain-sensing system eliminates the need for installing the shear strain sensors to measure the surface distortions through which the cross-sectional rotations of the beam can be determined.

Sensor Installation Examples

Installation of the two-line strain-sensing system for typical beam-like structures is discussed in the succeeding sections. These typical beam-like structures include a wing box and cantilever tubular beam.

Wing Box

Figure 5 shows the first example of applying the two-line strain-sensing system to a wing box structure under combined bending and torsion. The two strain-sensing lines (front and rear) can be installed along the lower edges (front and rear) of the wing box with chord-wise separation distance, d_i, at the strain-sensing cross section, $x = x_i$. The two strain-sensing lines can be parallel (d_i = constant) or tapered with the separation distance, d_i, decreasing toward the wingtip according to the horizontal taper rate of the wing.

Cantilever Tubular Beam

Figure 6 shows another example of the application of the two-line strain-sensing system to a tapered cantilever tubular beam under bending and torsion. The front and rear strain-sensing lines can be installed at a symmetrical angular location of $\pm\alpha$ measured from the bottom of the tube. To obtain larger bending strain data, a smaller value of α is desired. But to obtain more accurate cross-sectional twist data, a larger α (that is, a larger separation distance) is desired. Therefore, $\alpha = \pm 30°$ may be a good compromise, because the separation distance, d_i, between the two strain-sensing lines will be equal to the tube radius. The magnitude of the strains measured at $\alpha = \pm 30°$ location (numerators of equation (23)) will be $\cos\alpha$ times the strains (numerators of equation (23)) measured at the bottom of the beam. The vertical distance, c_i, from the neutral axis to the strain-sensing stations (denominators of equation (23)), however, will be $\cos\alpha$ times the tube radius, thereby canceling out the effect of $\cos\alpha$. Therefore, the averaged deflection curve generated by using the two-line strain-sensing system at $\alpha = \pm 30°$ will be equivalent to the deflection curve generated by using a single strain-sensing line along the bottom surface of the tube.

Deflections

The deflections, $\{y_i, y_i'\}$, of the front and rear strain-sensing stations lying at the sensing cross section, $x = x_i$ (i = 0, 1, 2, 3, …, n) (figs. 5, 6), can be calculated from deflection equation (23), which is rewritten (terms $y_0 + (i)\Delta l \tan\theta_0$ removed) in the following forms for the front and rear strain-sensing stations, respectively:

For the front strain-sensing line,

$$y_i = \frac{(\Delta l)^2}{6} \sum_{j=1}^{i} \frac{1}{c_{i-j}} \left\{ \left[3(2j-1) - (3j-2)\frac{c_{i-j+1}}{c_{i-j}} \right] \varepsilon_{i-j} + (3j-2)\varepsilon_{i-j+1} \right\} \quad ; \quad (i = 1, 2, 3, \ldots, n) \qquad (36)$$

For the rear strain-sensing line,

$$y_i' = \frac{(\Delta l)^2}{6} \sum_{j=1}^{i} \frac{1}{c_{i-j}} \left\{ \left[3(2j-1) - (3j-2)\frac{c_{i-j+1}}{c_{i-j}} \right] \varepsilon_{i-j}' + (3j-2)\varepsilon_{i-j+1}' \right\} \quad ; \quad (i = 1, 2, 3, \ldots, n) \qquad (37)$$

By averaging the front and rear deflections, $\{y_i, y_i'\}$, calculated from equations (36) and (37), respectively, we can eliminate the torsional effect to yield the true bending deflections of the wing box.

Cross-Sectional Twists

If d_i denotes the chord-wise separation distance between the front and rear strain-sensing cross section at $x = x_i$ (figs. 5, 6), then the cross-sectional twist angle, ϕ_i, at the strain-sensing cross section, $x = x_i$, can be calculated from the cross-sectional twist angle equation

$$\phi_i = \sin^{-1}\left(\frac{y_i - y_i'}{d_i}\right) \quad ; \quad (i = 0, 1, 2, 3, \ldots, n) \tag{38}$$

in which $\phi_0 = 0$ at the wing root. The deflections, $\{y_i, y_i'\}$, can be calculated from deflection equations (36) and (37), respectively, using the measured bending strain data as inputs.

For an aircraft wing (fig. 5), when the value of d_i is much larger than the wing depth, equation (38) could give sufficiently accurate ϕ_i without the need to install distortion sensors (see the section entitled, "Tapered Wing Boxes"), because the effect of surface shear strains on the bending strains is negligible. For the tubular structure (fig. 6) for which d_i is in the order of the radius, however, equation (38) may lose accuracy, because the surface shear strains will influence the bending strains (see the section entitled, "Tapered Tubular Beams"). An alternative method to obtain the cross-sectional twist angles, ϕ_i, for a tubular structure is to install a surface shear strain-sensing line for measurement of surface distortion angles, from which ϕ_i can be calculated. This alternative method is discussed in reference 2.

APPLICATION TO FREE–FREE BEAMS

The fuselage of an aircraft during flight is a good example of a free-free unsupported beam (fig. 7). The fuselage is a tubular structure with varying cross sections and can be considered as a nonuniform beam so that deflection equations (16) and (23), developed for nonuniform and slightly nonuniform cantilever beams, respectively, can be applied. For monitoring the deflections of the airborne fuselage under either vertical or horizontal bending, the strain-sensing line can be installed axially on the bottom (belly) surface or on the side of the fuselage (fig. 7).

Before deflection equation (16) or (23) is applied for the deformed shape predictions of the fuselage, some basics of equations (16) and (23) must be understood. Remember that in the formulation of deflection equations (16) and (23), the reference strain-sensing station, x_0, is located at the built-in end. With the built-in condition, $y_0 = \tan\theta_0 = 0$, imposed, equations (16) and (23) are also applicable to the moving cantilever beams, because the deflection, y_i, calculated from equation (23) is relative to the tangent line ($\tan\theta_0 = 0$) stemming from the reference strain-sensing station, x_0, at the built-in end (fig. 7). Equations (16) and (23) can be applied to the free-free unsupported moving fuselage case using the following approach.

The fuselage can be considered two nonuniform cantilever beams joined together at the center-of-gravity (CG) cross section (fig. 7). During flight, the CG cross section has the least movement compared with other fuselage cross sections. For practical purpose, it is best to choose the reference strain-sensing station, x_0, at the CG cross section and divide the strain-sensing line into two segments (fig. 7). One segment is for the fore section and the other for the aft section of the fuselage. Thus, by imposing

$y_0 = \tan\theta_0 = 0$ at the reference strain-sensing station, x_0 (considered as a built-in end), deflection equations (16) and (23) for the cantilever beam can be used to calculate the deflections of the fore and aft sections of the fuselage. The calculated deflection, y_i, will then be the relative deflection with respect to the tangent line passing though the reference strain-sensing station, x_0, which moves (translates and rotates) with the fuselage (fig. 7).

APPLICATION TO STRUCTURAL PANELS

Deflection equations (33) and (35) developed for slightly nonuniform simple beams can also be used for deformed shape predictions of structural panels (for example, flat, cylindrical, shallow spherical, and wing panels). For the shape sensing of structural panels, multiple biaxial strain-sensing lines are required (fig. 8). The panel strip region lying beneath each strain-sensing line will behave as an embedded beam (cantilever or simple beam, depending on the panel edge support conditions); therefore, deflection equations (33) and (35) are applicable. Each surface strain sensor will then sense the bending strain of the fictitious beam embedded beneath the strain-sensing line and not sense the bending strain of an isolated beam. As such, each strain output is the true panel bending strain with a biaxial effect. Keep in mind that the bending strain of the beam that is embedded in the panel will increase if the embedded beam is isolated. Therefore, the one-dimensional beam strain does not need to be corrected into a two-dimensional panel strain. This feature is a powerful characteristic of the Ko displacement theory, which is applicable whether the structure is one-dimensional and beam-like or two-dimensional and panel-like. The deflection equations previously developed for uniform beams (cantilever and two-point supported; ref. 2) were used for the deformed shape predictions of uniform-thickness square panels (four edges simply supported or four edges clamped), and were quite accurate in the panel shape predictions.

VALIDATION OF KO DISPLACEMENT THEORY

To examine the accuracy of the further-developed Ko displacement theory for nonuniform beams, several beam structure cases were chosen: (1) tapered tubular beams (cantilever and two-point supported), and (2) wing boxes (depth-tapered unswept, depth-tapered swept, width-tapered unswept, and double-tapered unswept). The Structural Performance And Resizing (SPAR) finite-element computer program (ref. 7) was then used to generate both the nodal strains and nodal displacements for these example structures. All the structures considered were made of aluminum material.

Input Strains

To test the accuracy of the displacement theory for nonuniform beams, the fiber-optic measured strain data were needed for input to the deflection equations for the calculations of beam deflections. Because the measured bending strain data were not yet available from the experiments, the SPAR program was used to generate the bending strains. The SPAR bending strains were generated as follows.

If σ_i is the axial stress at the strain-sensing station, x_i, obtained from the SPAR nodal stress outputs, then the corresponding bending strain, ε_i, for input to the deflection equations can be calculated from Hooke's law,

$$\varepsilon_i = \frac{\sigma_i}{E} \tag{39}$$

Using the finite-element generated strains (eq. (39)), we can calculate the structural deflections and then compare them with the corresponding nodal displacements obtained from the SPAR displacement outputs for validating the accuracy of the Ko displacement theory.

Alternatively, using the SPAR displacement outputs, we can also obtain the bending strain, ε_i, by dividing the element axial length change by the undeformed length of the element at the strain-sensing station, x_i (ref. 2). This element displacement method gives bending strains that are practically identical to those obtained from the nodal stress method (eq. (39)) in the region of small deflections, but it starts to lose accuracy in the highly bent region near the free end. The SPAR displacement outputs are referred to the undeformed beam axis, and at increasing deflections near the highly bent beam tip, the true tensile strains (positive value) along the deformed beam axis, when projected on the undeformed beam axis, may appear as compressive strains (negative value). Thus, in the calculations of strains using the element displacement method, y-displacement components must be considered. Therefore, the simpler nodal stress method (eq. (39)) was used in generating the input strains.

Tapered Tubular Beams

Each of the tapered tubular beams (cantilever, two-point supported) used in the SPAR analysis has a radius that linearly decreases from one end toward the other end. The tapered tubular beam tapers down not only in the vertical and horizontal planes, but also in any radial plane because of circular cross sections. Table 1 lists the dimensions of each aluminum tapered tubular beam considered.

Table 1. Dimensions of aluminum tapered tubular beams.

l, in.	c_0, in.	c_n, in.	c_n / c_0
100.5	4	4	1.00 (uniform)
100.5	4	3	0.75
100.5	4	2	0.50
100.5	4	1	0.25

Cantilever Beams

Figure 9 shows the finite-element model for a tapered cantilever tubular beam. The beam is subjected to a tip vertical load of P = 100 lb (fig. 9a), and a combined tip vertical load and tip torque of P = 100 lb and $T = 400 \times c_n$ in-lb, respectively (fig. 9b).

Bending Only

Figure 10 shows the strain curves for different tapered cantilever tubular beams under bending only, calculated from equation (39), using the SPAR element stress outputs. The strain curve is a straight line for the classical uniform beam case ($c_n / c_0 = 4/4$) but becomes bow shaped as the depth ratio, c_n / c_0, decreases. When the depth ratio reaches a minimum of $c_n / c_0 = 1/4$, the strain curve is deeply bent by nearly 100°.

Figure 11 shows the beam deflection curves for different tapered cantilever tubular beams, calculated from deflection equation (16) (eq. (23) for the uniform beam), using the strain data at the strain-sensing stations shown in figure 10 (solid curves with solid circular symbols). For comparison, the deflections calculated from the SPAR program are also plotted (dashed curves with open circular symbols). The excellent correlation between the two sets of deflection curves shows the high degree of accuracy of the displacement theory (eqs. (16) and (23)) formulated for the nonuniform cantilever beams.

Keep in mind that in the formulation of the Ko displacement theory (ref. 2), the distribution of bending strains along the discretized cantilever beam was assumed to be piecewise linear as described by equation (9). Therefore, the strain curves associated with this theory are the piecewise linear approximations (connecting the strain data points at the strain-sensing stations with straight lines) of the smooth strain curves shown in figure 10. Note from figure 10 that for slightly bent strain curves, the piecewise linear approximation could be quite accurate, but in a highly bent region of the strain curve for the lowest depth ratio, $c_n / c_0 = 1/4$, the piecewise linear approximation may lose some accuracy locally. In spite of this shortcoming, the Ko displacement theory (eqs. (16) and (23)) still predicts highly accurate deflections for the whole range of depth ratios, $4/4 \geq c_n / c_0 \geq 1/4$ (fig. 11). The same arguments also hold for the remaining examples presented in the succeeding sections.

Bending and Torsion

Figure 12 shows the SPAR-generated strain curves for the front (fig. 12a) and rear (fig. 12b) strain-sensing lines for different tapered cantilever tubular beams under combined bending and torsion. The front (left) and rear (right) strain-sensing lines are 60° apart as shown in figure 6. The front and rear strain curves are very similar because of the proximity of the two strain-sensing lines. Note from figure 12 that the strain curves for the tapered tubes ($c_n / c_0 < 4/4$) are bow shaped, and the degree of bend increases as the depth ratio, c_n / c_0, decreases. When the depth ratio reaches a minimum of $c_n / c_0 = 1/4$, the front and rear strain curves are deeply bent by nearly 100°, similar to the strain curves in the bending only cases (fig. 10). For the classical uniform cantilever beam case ($c_n / c_0 = 4/4$, fig. 12), the front and rear bending strain curves are linear except in the beam tip region. The abnormal deviation of bending strains (especially for the front strain curve) near the beam tip region could be attributed to the increasing local element distortions caused by the concentrated tangential loads applied at selected points at the beam tip to create torsion. Keep in mind that the bending strains have been calculated from the finite-element stresses.

If torsion is removed, the front and rear strain curves of the classical uniform cantilever beam case ($c_n / c_0 = 4/4$) will be perfectly straight lines as shown with dashed lines in figure 12 (see also fig. 10 for the $c_n / c_0 = 4/4$ case). With torsion added, each bending strain curve for the $c_n / c_0 = 4/4$ case (fig. 12) gradually deviates from the corresponding strain curve for bending only (dashed lines, fig. 12), and the deviation increases slightly toward the beam tip.

Figure 13 shows the deflection curves along the front and rear strain-sensing lines for different tapered cantilever tubular beams, calculated from deflection equation (16) (eq. (23) for the uniform beam), using the strain data shown in figure 12 (solid curves with solid circular symbols). For comparison, the deflections calculated from the SPAR program are also plotted (dashed curves with open circular symbols. The excellent correlation between the two sets of deflection curves demonstrates the high accuracy of the displacement theory (eqs. (16) and (23)) formulated for nonuniform cantilever beams.

Figure 14 shows the cross-sectional twist angles, ϕ_i, for different tapered cantilever tubular beams, calculated from equation (38) using the deflection data, $\{ y_i, y_i' \}$, along the front and rear strain-sensing lines shown in figure 13. Graphically, the agreement between the twist angles calculated from the displacement theory and those calculated from the SPAR program does not appear as good as the agreement between the deflection curves (fig. (13)). It must be understood that the values of ϕ_i are quite small (less than 1°) because of the proximity ($1-4$ in. apart) of the front and rear strain-sensing lines, and because of a low twisting moment, $T = 400 \times c_n$ in-lb. Therefore, slight differences (almost graphically inconspicuous) between the Ko displacement theory and SPAR program deflection data of figure (13) have a strong effect on the values of ϕ_i calculated from equation (38). Table 2 lists the beam tip deflections, $\{ y_n , y_n' \}$, of the

front and rear strain-sensing lines, and the cross-sectional rotation angles, ϕ_i, calculated from the SPAR program and Ko displacement theory.

Table 2. Comparison of displacement data calculated from SPAR program with those calculated from Ko displacement theory for different tapered cantilever tubular beams; $l = 100.5$ in., $P = 100$ lb, $T = 400 \times c_n$ in-lb.

		y_n, in.		y_n', in.		ϕ_n, deg	
c_0, in.	c_n, in.	SPAR	Ko	SPAR	Ko	SPAR	Ko
4.0*	4.0*	0.72027	0.72677	0.70249	0.71001	0.25468	0.24007
4.0	3.0	0.88400	0.88706	0.86854	0.87291	0.29526	0.27025
4.0	2.0	1.16457	1.16199	1.15133	1.15148	0.37930	0.30109
4.0	1.0	1.78962	1.77362	1.77859	1.76628	0.63197	0.42056

* Uniform beam.

Note from table 2 that the differences between the ϕ_n values calculated from the SPAR program and those calculated from the Ko theory are minuscule, in the range of {0.0146, 0.0250, 0.0782, 0.2114} deg, for the depth ratios, $c_n/c_0 = \{4/4,\ 3/4,\ 2/4,\ 1/4\}$, respectively. As seen in the subsequent wing box cases, in which the values of ϕ_i are larger because of greater distances between the front and rear strain-sensing lines, the prediction of ϕ_i turns out to be quite good.

Two–Point Supported Beams

Two cases of simple beams (two-point supported beams) were considered. Figure 15 shows the SPAR models of the two cases of tapered tubular simple beams, one with both ends simply supported (fig. 15a), and one with both ends fixed (fig. 15b). Each simple beam is subjected to a downward load of P = –200 lb at the center of the beam.

Simply Supported Ends

Figure 16 shows the strain curves, calculated from equation (39) using the SPAR element stress outputs, for different tapered tubular simply supported beams subjected to a downward force of P = –200 lb at the center of the beam. The strain curve is roof shaped for the classical uniform beam ($c_n / c_0 = 4/4$). For the depth ratio, $c_n / c_0 < 4/4$, the strain curves are slightly concave in the left-hand region but convex (bow shaped) in the right-hand region with the degree of bow bend increasing with the decreasing depth ratio, c_n / c_0. At the lowest depth ratio of $c_n / c_0 = 1/4$, the strain curve in the right-hand region (decreasing radius) is deeply bent by nearly 90°.

Figure 17 shows the beam deflection curves for different tapered tubular simply supported beams, calculated from simply supported beam deflection equation (33) using the strain data shown in figure 16 (solid curves with solid circular symbols). These deflection curves are compared with the deflection curves calculated from the SPAR program (dotted curves with open circular symbols). The SPAR program gives slightly larger deflections, because the transverse shear effect is accounted for in the SPAR program. Note from figure 17 that the transverse shear effect (difference between the two sets of deflection curves) is quite small for the uniform beam, $c_n / c_0 = 4/4$, and gradually grows larger as the depth ratio, c_n / c_0, decreases.

At the lowest depth ratio, $c_n / c_0 = 1/4$, the transverse shear effect at the center of the beam amounts to 3.63 percent of the beam center deflection. Remember, for the tapered cantilever tubular beam cases (fig. 11), the transverse shear is practically inconspicuous for the whole range of depth ratios, $4/4 \geq c_n / c_0 \geq 1/4$.

To show that the difference between the deflections calculated from the SPAR program and those calculated from the displacement theory is caused by the transverse shear effect, the shear modulus, *G*, was set very large ($G \to \infty$) in the SPAR program to eliminate the transverse shear effect. As expected, the resulting SPAR deflection curves (dashed curves with open square symbols, fig. 17) practically fall on top of the corresponding Ko deflection curves (solid curves with solid circular symbols, fig. 17), thus proving the argument. The excellent deflection predictions based on deflection equation (33) for the simply supported beam validate the accuracy of the Ko displacement theory developed for slightly nonuniform beams.

Fixed Ends

Figure 18 shows the strain curves generated from the SPAR program (equation (39)), for different tapered tubular simple beams with two ends fixed, subjected to a central downward load of P = –200 lb. The strain curve is again roof shaped for the classical uniform beam ($c_n / c_0 = 4/4$). For the depth ratio, $c_n / c_0 < 4/4$, the strain curves are slightly concave in the left-hand region but convex in the right-hand region, with the degree of convexity increasing as the depth ratio, c_n / c_0, decreases. At the lowest depth ratio of $c_0 / c_n = 1/4$, the strain curve in the right-hand region is deeply bent.

Figure 19 shows the beam deflection curves for the fixed-end simple beams, calculated from cantilever beam deflection equation (16) (eq. (23) for the uniform beam), using the strain data shown in figure 18 (solid curves with solid circular symbols). These deflection curves are compared with the deflection curves calculated from the SPAR program (dotted curves with open circular symbols). Note that equations (16) and (23) give $y_n = 0$ at the right end, and therefore it is not necessary to use the error correction equation (35) for the $y_n \neq 0$ case. Note from figure 19 that the correlation between the two sets of deflection curves is reasonably good. Similar to the simply supported case, the SPAR program gives slightly larger deflections, because the transverse shear effect is considered in the SPAR program. Note that the transverse shear effect (difference between each set of SPAR and Ko deflection curves) increases slightly as the depth ratio, c_n / c_0, decreases. At the lowest depth ratio, c_n / c_0 = 1/4, the transverse shear effect at the center of the beam amounts to 10.29 percent of the beam center deflection. Again, by setting the shear modulus, *G*, very large ($G \to \infty$) in the SPAR program, the transverse shear effect was removed, and the resulting SPAR deflection curves (dashed curves with open square symbols) fall nearly on top of the corresponding Ko deflection curves (solid curves with solid circular symbols) for the whole range of depth ratios, $4/4 \geq c_n / c_0 \geq 1/4$. Thus, if the transverse shear effect is ignored, then cantilever beam deflection equations (16) and (23) are quite accurate when applied to the fixed-end tapered simple beam, even down to the lowest depth ratio of $c_0 / c_n = 1/4$.

Tapered Wing Boxes

For numerical validation of Ko displacement theory, three different types of wing boxes were considered: (1) depth-tapered wing boxes (unswept and swept), (2) width-tapered unswept wing boxes, and (3) double-tapered unswept wing boxes. The two strain-sensing lines for each wing box case are installed at the front and rear lower edges of the wing box.

Depth–Tapered Wing Boxes

The depth-tapered wing boxes considered are unswept (fig. 20a) and swept (swept angle, β, deg; fig. 20b). All depth-tapered wing boxes have a constant width, with the depth tapering off toward the free end (vertically tapered). Table 3 lists the dimensions of the depth-tapered unswept and swept wing boxes. Each wing box is subjected to vertical load of P = 100 lb and a torque of $T = 50 \times w$ in-lb (clockwise) at the tip of wing box (fig. 20). For the swept wing boxes, a counterclockwise torsion of $T = -50 \times w$ in-lb was also considered.

Table 3. Dimensions of depth-tapered unswept and swept wing boxes.

l, in.	c_0, in.	c_n, in.	w, in.	β, deg	
				(unswept)	(swept)
100.0	2.0	2.0 (uniform)	17.0	0.0	10.0
100.0	2.0	1.5	17.0	0.0	10.0
100.0	2.0	1.0	17.0	0.0	10.0
100.0	2.0	0.5	17.0	0.0	10.0

Unswept Wing Boxes

Figure 21 shows the plots of the strains along the front and rear strain-sensing lines, calculated from the SPAR element stress outputs, for different depth-tapered unswept wing boxes subjected to a vertical load of P = 100 lb and a torque of $T = 50 \times w$ in-lb at the wing box tip (fig. 20). The front-edge and rear-edge strain curves for the nontapered uniform wing box ($c_n / c_0 = 2/2$; fig. 21) are practically straight lines like those in the classical cantilever beam case. For the tapered wing boxes, the front-edge strain curves (fig. 21a) become bow shaped with the bend increasing as the taper depth ratio, c_n / c_0, decreases (very similar to the tapered cantilever beam cases, fig. 10). When the taper depth ratio reaches a minimum of c_n / c_0 = 0.5/2, the strain curve becomes deeply bent by more than 90°. The rear-edge strain curves for the tapered wing boxes are almost straight except in the wing root and wingtip regions. As the taper depth ratio, c_n / c_0, decreases, the strain curves become more tilted.

Figure 22 shows the front-edge and rear-edge deflections, $\{ y_i, y_i' \}$, for different depth-tapered unswept wing boxes, calculated from deflection equations (36) and (37), respectively, using the strain data shown in figure 21 as inputs (solid lines with solid circular symbols). For comparison, the deflections obtained from the SPAR nodal displacement outputs are also plotted (dashed lines with open circular symbols). The excellent correlation between the two sets of deflection curves reinforces the high degree of accuracy of the Ko displacement theory (eqs. (16) and (23)) formulated for nonuniform cantilever beams.

Note that under the combined bending and torsional loading, the front-edge and rear-edge deflection curves shown in figure 22 contain torsional components. To obtain an overall bending deflection curve for the wing box, the torsional effect must be removed by averaging the front-edge and rear-edge deflection curves of figure 22.

Figure 23 shows the cross-sectional twist angles, ϕ_i, for different depth-tapered unswept wing boxes, calculated from equation (38) using the deflection data, $\{ y_i, y_i' \}$, along the front and rear strain-sensing lines. Again the agreement between the displacement theory and SPAR program is quite good. Interestingly, at the taper depth ratios of c_n / c_0 = 0.5/2 and c_n / c_0 = 1/2, the cross-sectional twist angle, ϕ_i (under combined loading), in the inboard region has the opposite sign of the wingtip torque, T. This sign change

of ϕ_i could result from the lack of cross-sectional shear stiffness, because the SPAR wing box models are hollow with no interior shear reinforcements. It was found that if rib and spar reinforcement elements were added to the hollow SPAR models, the cross-sectional twist angle, ϕ_i, at any point along the wingspan, would follow the sign of the wingtip torque, T.

Swept Wing Boxes

Figure 24a shows the plots of the strains along the front strain-sensing line, calculated from the SPAR element stress outputs, for different depth-tapered swept wing boxes subjected to a vertical load of P = 100 lb and a torque of $T = 50 \times w_n$ in-lb (clockwise, looking toward the wing root) at the wing box tip (fig. 20b). Overall the shapes of the front-edge strain curves are similar to those for the unswept wing boxes cases (fig. 21) except in the wing root regions where the strain curves have saddle-shaped areas. The front-edge strain curve for the uniform wing box ($c_n / c_0 = 2/2$; fig. 24a) is a straight line except in the wing root region. For the depth-tapered swept wing boxes, the front-edge strain curves become bow shaped (except in the wing root region), with the bend increasing as the taper depth ratio, c_n / c_0, decreases (very similar to the depth-tapered unswept wing box cases, fig. 21). When the taper depth ratio reaches a minimum of c_n / c_0 = 0.5/2, the strain curve becomes deeply bent by more than 90°.

Figure 24b shows the plots of the strains along the rear-edge strain-sensing line, calculated from the SPAR element stress outputs, for different depth-tapered swept wing boxes. Overall the rear-edge strain curves are almost linear like those for the unswept wing boxes cases (fig. 21) except in the wing root regions where the strains increase sharply. The rear-edge strain curve for the uniform wing box ($c_n / c_0 = 2/2$) is almost a straight line except in the wing root and wingtip regions. For the tapered swept wing boxes, the strain curves are nearly straight except in the wing root and wingtip regions. As the taper depth ratio, c_n / c_0, decreases, the strain curves become more tilted.

Figure 25 shows the front-edge and rear-edge deflections, $\{y_i, y_i'\}$, for different depth-tapered swept wing boxes under bending and clockwise torsion, calculated from deflection equations (36) and (37), using the strain data shown in figure 24 as inputs (solid lines with solid circular symbols). For comparison, the deflections obtained from the SPAR nodal displacement outputs are also plotted (dashed lines with open circular symbols). Note that the correlation between the Ko and SPAR deflection curves is excellent, providing confidence in the Ko displacement theory (eqs. (16) and (23)) formulated for nonuniform cantilever beams.

Figure 26 shows the cross-sectional twist angles, ϕ_i (with respect to airstream), for different depth-tapered swept wing boxes (clockwise torsion cases), calculated from equation (38) using the deflection data, $\{y_i, y_i'\}$, along the front-edge and rear-edge strain-sensing lines. Similar to the unswept wing cases (fig. 23), at the taper depth ratios, c_n / c_0 = 0.5/2 and c_n / c_0 = 1/2, the cross-sectional twist angle, ϕ_i, in the inboard region has the opposite sign of the wingtip torque, T, because the SPAR wing box models are hollow, having no interior reinforcements (no cross-sectional shear stiffness). The peculiar behavior of ϕ_i (under combined loading) disappeared if the interior shear reinforcement elements were added in the hollow SPAR models. Overall the agreement between the Ko displacement theory and the SPAR program is excellent for the swept wing boxes.

Figures 27, 28, and 29 show sets of strain curves, deflection curves, and cross-sectional twist angle curves, respectively, for the swept wing boxes under combined bending and counterclockwise torsion. Notice that by reversing the direction of torsion, the shapes of the front and rear strain and deflection curves do not become the interchanged versions of the corresponding curves for the clockwise torsion cases

(figs. 24, 25, 26) but have slight variations resulting from the swept effect near the wing root and wingtip. The most conspicuous difference between the two torsion cases is that the front-edge strain curve of c_n = 0.5 in. for the counterclockwise torsion case (fig. 27b) does not have a saddle-shaped area near the wing root like the rear-edge strain curve of c_n = 0.5 in. for the clockwise torsion case (fig. 24a). The excellent agreement shown in figures 28 and 29 reinforces the high degree of accuracy of the Ko displacement theory (eqs. (16) and (23)) formulated for nonuniform cantilever beams.

Width–Tapered Wing Boxes

Figure 30 shows the unswept width-tapered wing box with a constant half depth, $c_0 = c_n$ = 0.5 in., and a decreasing width toward the free end (horizontally tapered). The strain-sensing lines are located at the lower front and rear edges. Each beam is subjected to a vertical load of P = 100 lb and a torque of $T = 50 \times w_n$ in-lb (clockwise) at the wing box tip (fig. 30). Table 4 lists the dimensions of each width-tapered unswept wing box.

Table 4. Dimensions of width-tapered unswept wing boxes.

l, in.	c_0, in.	c_n, in.	w_0, in.	w_n, in.	β, deg
60.0	0.5	0.5	30.0	30.0 (uniform)	0.0
60.0	0.5	0.5	30.0	20.0	0.0
60.0	0.5	0.5	30.0	10.0	0.0
61.0	0.5	0.5	30.0	5.0	0.0

Figure 31 shows the strain curves generated from the SPAR element stress outputs for different width-tapered wing boxes subjected to a vertical load of P = 100 lb and a torque of $T = 50 \times w_n$ in-lb (clockwise) at the wing box tip (fig 30).

Figure 32 shows the deflection curves for different width-tapered unswept wing boxes, calculated from deflection equation (23), using the associated input strain data of figure 31 (solid lines with solid circular symbols). For comparison, the deflection curves obtained from the SPAR nodal displacement outputs are also plotted (dashed lines with open circular symbols). The excellent correlation between the two sets of deflection curves validates the high degree of accuracy of the Ko displacement theory (eq. (23)) formulated for nonuniform cantilever beams. Figure 33 compares the cross-sectional twist angles, ϕ_i, calculated from equation (38) with those generated from the SPAR program, for different width-tapered wing boxes. Again the agreement is excellent.

Double–Tapered Wing Boxes

The double-tapered wing box (fig. 34) is unswept and has both a width and depth (horizontally and vertically) that taper down toward the free end. The front and rear strain-sensing lines are located at the front and rear lower edges, respectively, of the wing box. Table 5 lists the dimensions of the double-tapered wing box. The wing box is subjected to a vertical load of P = 100 lb and a torque of $T = 50 \times w_n$ in-lb (clockwise) at the wing box tip.

Table 5. Dimensions of double-tapered unswept wing box.

l, in.	c_0, in.	c_n, in.	w_0, in.	w_n, in.	β, deg
100.0	2.0	1.0	34.0	17.0	0.0

Figure 35 shows the strain curves generated from the SPAR element stress outputs for the front and rear oblique strain-sensing lines at the lower edges of the double-tapered wing box. The strain curves are deeply bent because of the double tapering effect. Remember that for the classical uniform cantilever beam, the strain curve is a straight line.

Figure 36 shows the deflection curves along the two oblique strain-sensing lines, calculated from deflection equation (16), using the strain data generated from the SPAR program shown in figure 35 (solid lines with solid circular symbols). For comparison, the deflections calculated from the SPAR program are also plotted (dashed lines with open circular symbols). The excellent correlation between the two sets of deflection curves validates the high degree of accuracy of the Ko displacement theory (eq. (16)) formulated for nonuniform cantilever beams.

Figure 37 compares the cross-sectional twist angles, ϕ_i, calculated from equation (38) with those calculated from the SPAR program, for the double-tapered wing box. The Ko and SPAR curves for ϕ_i practically fall on top of each other, showing the surprisingly high degree of accuracy of the Ko displacement theory.

EXACT AND EXPANDED DEFLECTION EQUATIONS

All the deflection curves for vertically tapered beams predicted from the Ko displacement theory, as shown in the preceding sections, were calculated using the exact deflection equation (16) formulated for nonlinear beams (for example, tapered beams). Because deflection equation (16) breaks down for the uniform beams, the deflection curves for the uniform beam cases had to be calculated from the expanded deflection equation (23), which was obtained from the exact deflection equation (16) by expanding the logarithmic term, $\log_e(c_i / c_{i-1})$, in the neighborhood of $(c_i / c_{i-1}) \approx 1$. The preceding examples demonstrate that equation (16) provides quite accurate shape predictions for tapered beams with all the taper depth ratios down to $c_n / c_0 = 1/4$.

To examine the deflection prediction accuracy, expanded deflection equation (23) was used to calculate the deflections of tapered cantilever tubular beams with different taper depth ratios, as shown in figure 11. Table 6 compares the beam tip deflections calculated from the SPAR program with those calculated from the exact deflection equation (16) and those calculated from the expanded deflection equation (23).

Note from table 6 that the two sets of deflection data calculated from deflection equations (16) and (23) are very close, with a peak difference of only 0.5293 percent for the lowest depth ratio, $c_n / c_0 = 1/4$. Thus, if the deflection data of equation (23) are plotted out in figure 11, the deflection curve will fall practically on top of the deflection curve calculated from equation (16) (fig. 11). This observation indicates that the expanded deflection equation (23) is quite accurate for the whole range of depth ratios, $4/4 \geq c_n / c_0 \geq 1/4$.

Table 6. Comparison of beam tip deflections, y_n, of tapered cantilever tubular beams calculated from SPAR program with those calculated from displacement equations (16) and (23); l =100.5 in., P =100 lb, n = 8.

c_0, in.	c_n, in.	y_n, in.			Percent difference between eq. (16) and eq. (23)
		SPAR	Eq. (16) (exact)	Eq. (23) (expanded)	
4.0	4.0 (uniform)	0.711620	Not applicable	0.702304	--------
4.0	3.0	0.876340	0.865681	0.866592	0.1052
4.0	2.0	1.158010	1.145292	1.145487	0.0170
4.0	1.0	1.784170	1.762277	1.752950	–0.5293

CONCLUDING REMARKS

The Ko displacement theory, originally formulated (in recursion formats) for shape predictions of nonuniform cantilever beams, was further developed into more compact mathematical forms. The accuracy of the further-developed Ko displacement theory was validated by finite-element analyses of various beam structures. The principal findings are as follows:

1. In the further-developed Ko displacement theory for the nonuniform cantilever beam, the deflections at the strain-sensing stations were expressed explicitly in terms of geometrical parameters of the beam and bending strains at all the inboard strain-sensing stations.

2. The exact deflection equations for nonuniform cantilever beams were expanded for slightly nonuniform cantilever beams so that the expanded deflection equations could degenerate into the limit case for uniform cantilever beams without encountering mathematical breakdown problems.

3. For tapered cantilever tubular beams with different taper rates, the deflections calculated from the expanded deflection equations were only 0.017–0.529 percent off from those calculated from the exact deflection equations formulated for nonuniform cantilever beams.

4. The further-developed displacement equations for nonuniform cantilever beams were used to formulate the displacement equations for nonuniform two-point supported beams and could be used for shape predictions of nonuniform structural panels.

5. The proposed two-line strain-sensing system provided a powerful method for simultaneously monitoring the bending and torsional deformations of nonuniform cantilever beams such as wing boxes. The two-line strain-sensing system eliminated the need to install shear strain sensors to measure the surface distortions for monitoring cross-sectional rotations of the beam.

6. A finite-element computer program was used to generate simulated strain data for input to the further-developed displacement equations. The displacement equations were then used to calculate deflections and cross-sectional twist angles, at discreet strain-sensing stations of the beam-like structure, for constructing the overall deformed shape of the whole structure.

7. The high degree of accuracy of the further-developed displacement theory for nonuniform beams was validated by finite-element analyses of various types of nonuniform beam structures (tapered tubular beams, such as cantilever and two-point supported beams; depth-tapered unswept and swept

wing boxes; width-tapered wing boxes; and double-tapered wing boxes) under combined bending and torsion.

8. For tapered beams, the bending strain distribution along the axis of the beam was nonlinear, and the nonlinearity increased with increasing taper rate. The piecewise linear approximation of strain distributions was adequate to obtain highly accurate deflection curves for the whole range of beam taper rates.

9. The Ko displacement theory, combined with the onboard strain-sensing system, form a powerful tool for in-flight deformed shape monitoring of unmanned aerospace vehicles (by ground-based pilots) to maintain safe flights. In addition, the real-time wing shape could be input to the aircraft control system for aeroelastic wing shape control.

FIGURES

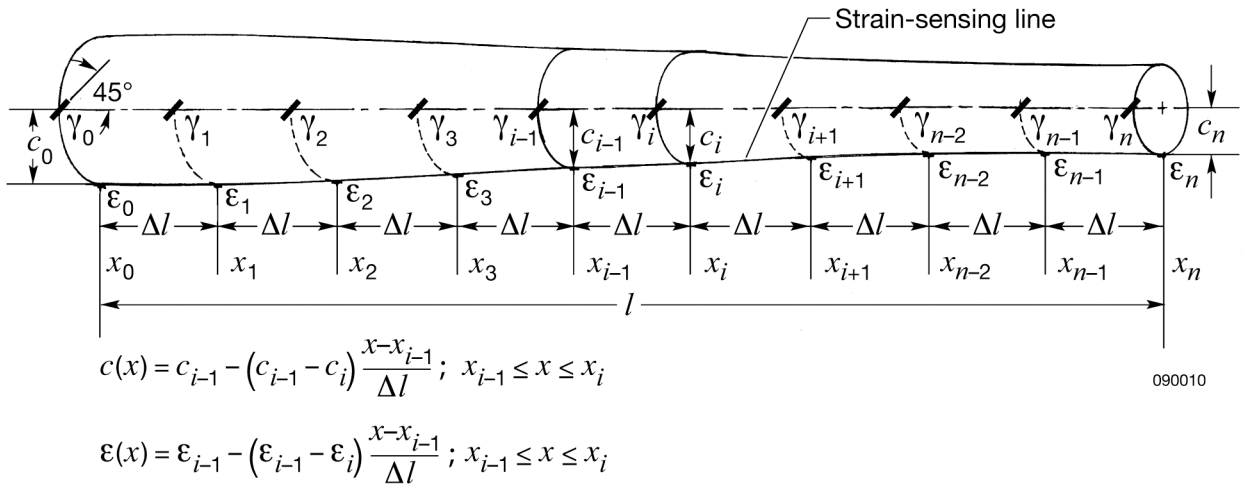

Figure 1. Nonuniform cantilever beam instrumented with bending and distortion strain sensors.

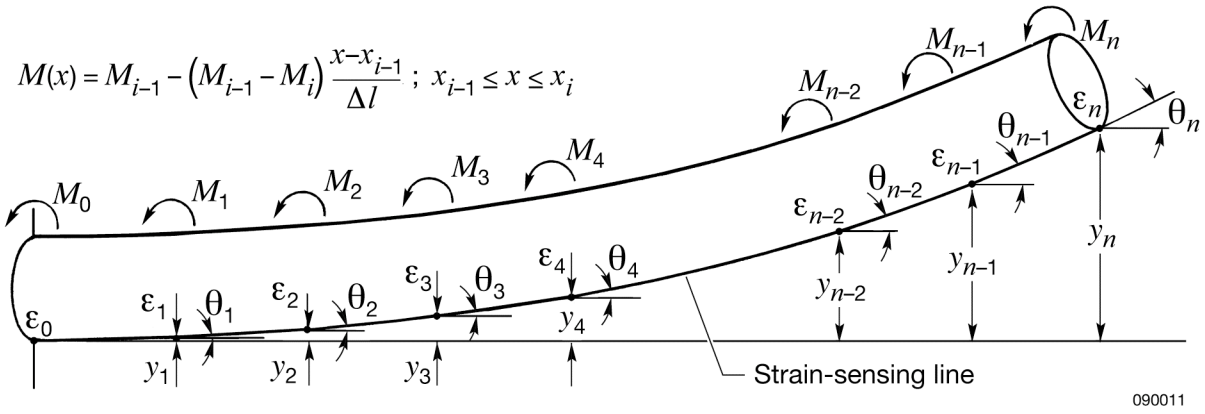

Figure 2. Deformed cantilever tubular beam showing slopes, θ_i, and deflections, y_i, at strain-sensing stations, x_i (i = 0, 1, 2, 3, …, n).

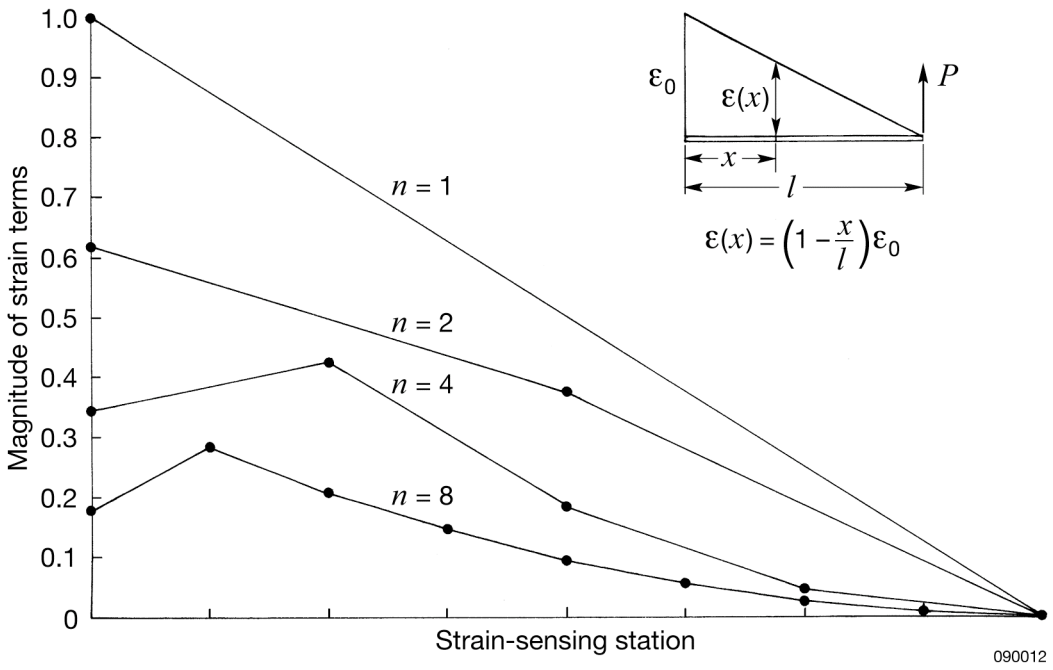

Figure 3. Relative magnitude of strain terms in deflection equation for a uniform cantilever beam.

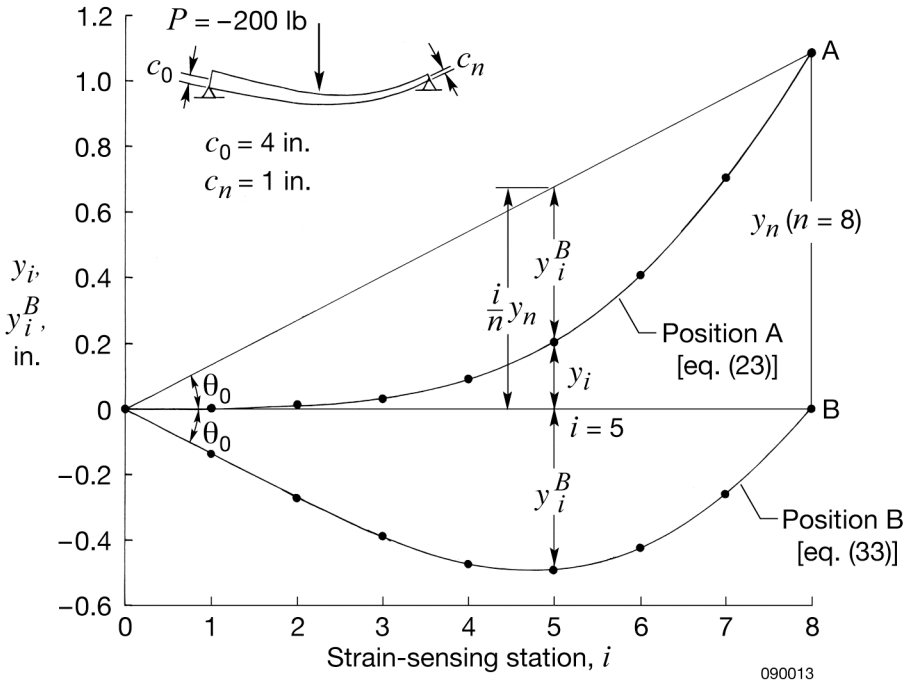

Figure 4. Linearly increasing downward shifting of deflection curve from cantilever beam position A to simple beam position B; zero shift at left end.

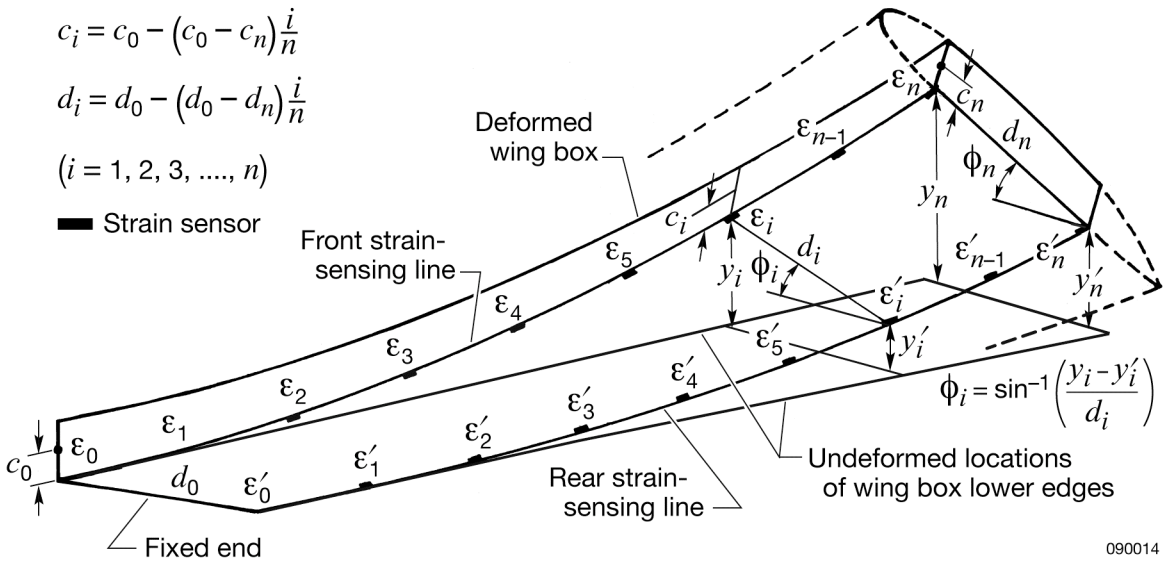

Figure 5. Tapered wing box instrumented with a two-line strain-sensing system.

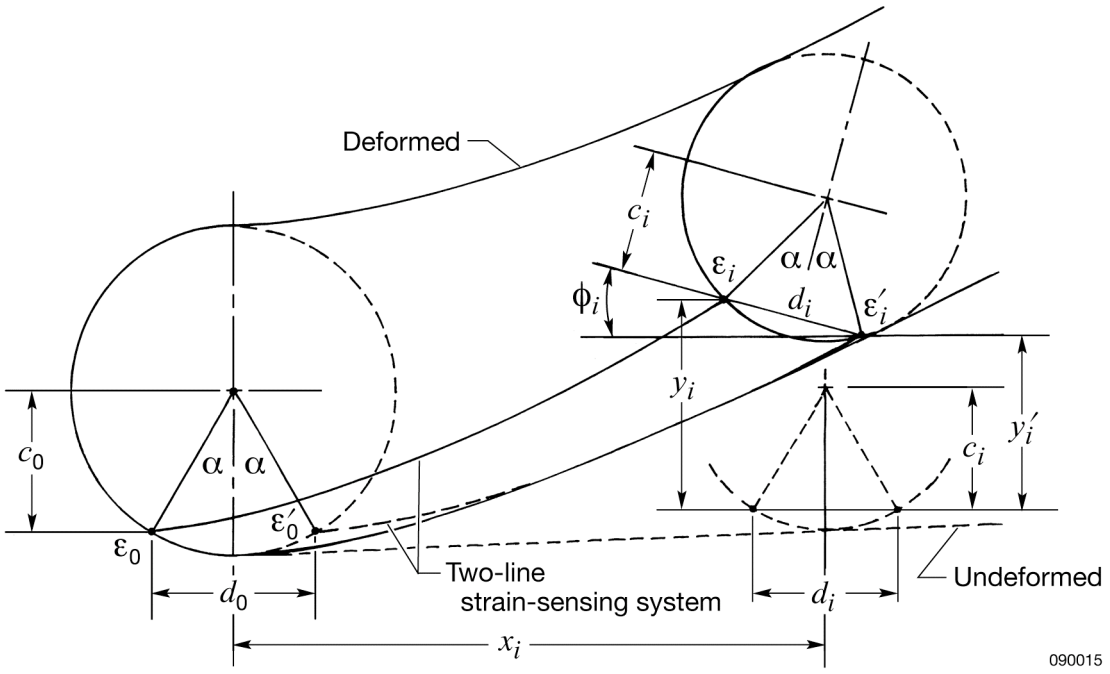

Figure 6. Tapered cantilever tubular beam instrumented with a two-line strain-sensing system.

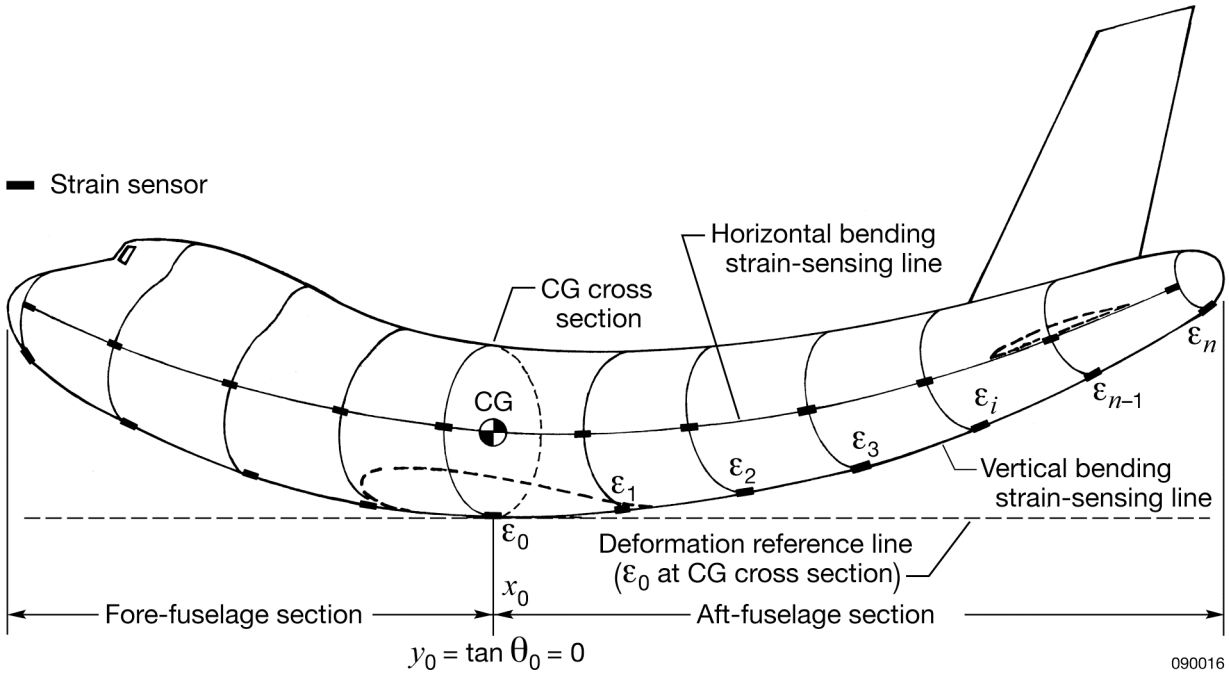

Figure 7. Aircraft fuselage instrumented with a two-line strain-sensing system.

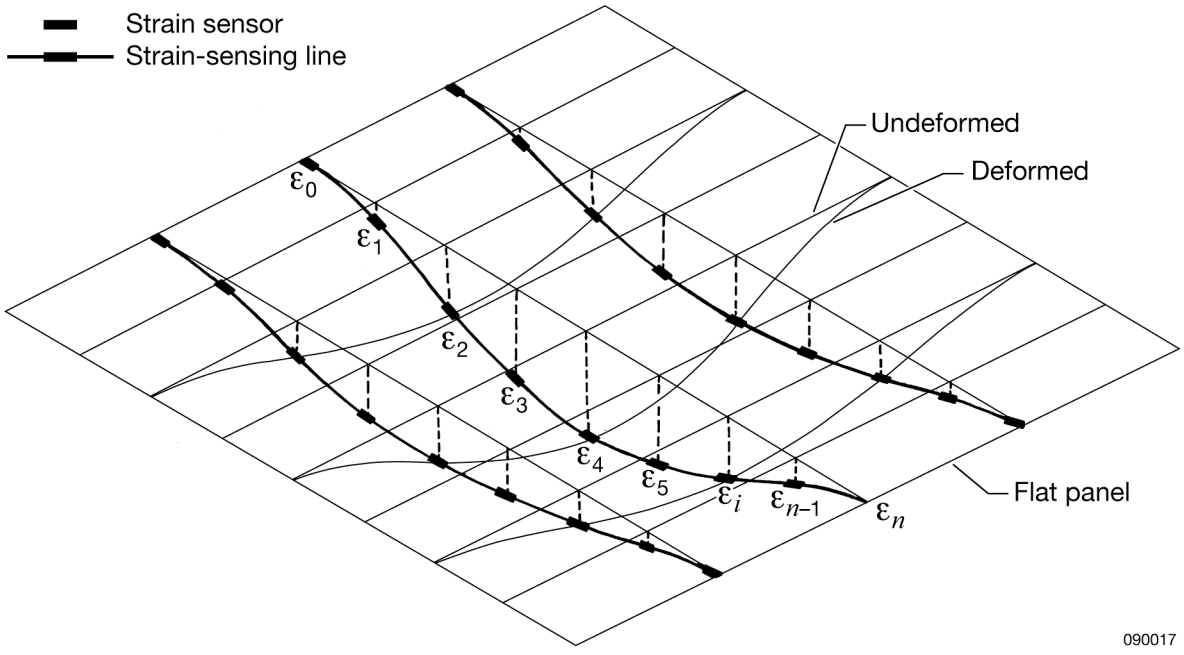

Figure 8. Structural panel instrumented with multiple biaxial strain-sensing lines.

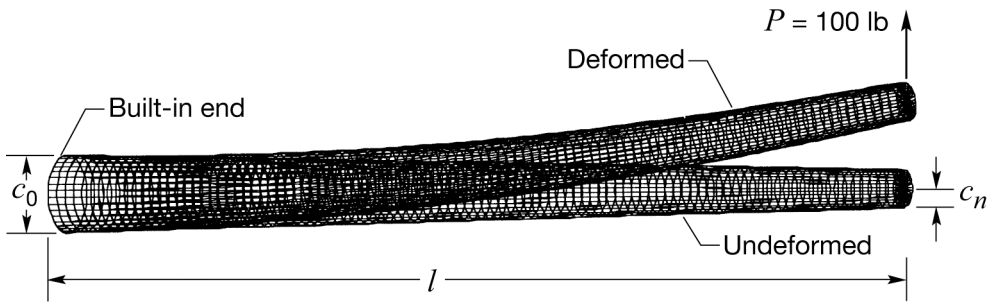

l	= 100.5 in.	Nodes	3673
t	= 0.02296 in.	Four-node elements	3636
c_0	= 4 in.	Three-node elements	36
c_n	= 1, 2, 3, 4 in.		

090018

(a) Tip vertical load of $P = 100$ lb; tip twisting moment of $T = 0$.

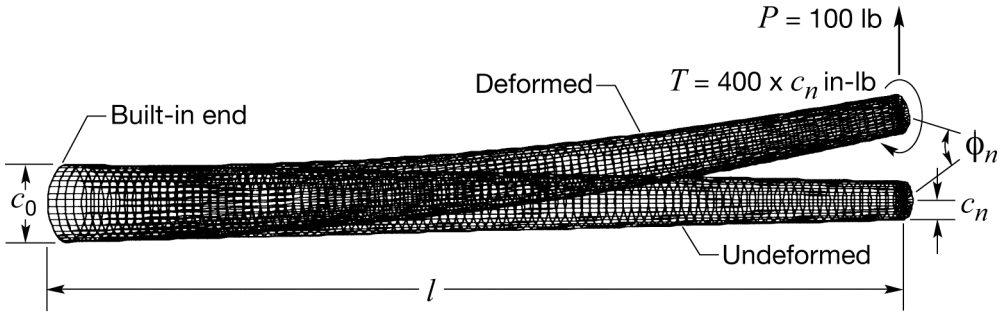

l	= 100.5 in.	Nodes	3673
t	= 0.02296 in.	Four-node elements	3636
c_0	= 4 in.	Three-node elements	36
c_n	= 1, 2, 3, 4 in.		

090019

(b) Tip vertical load of $P = 100$ lb; tip twisting moment of $T = 400 \times c_n$ in-lb.

Figure 9. Finite-element model for a tapered cantilever tubular beam subjected to different tip loading conditions.

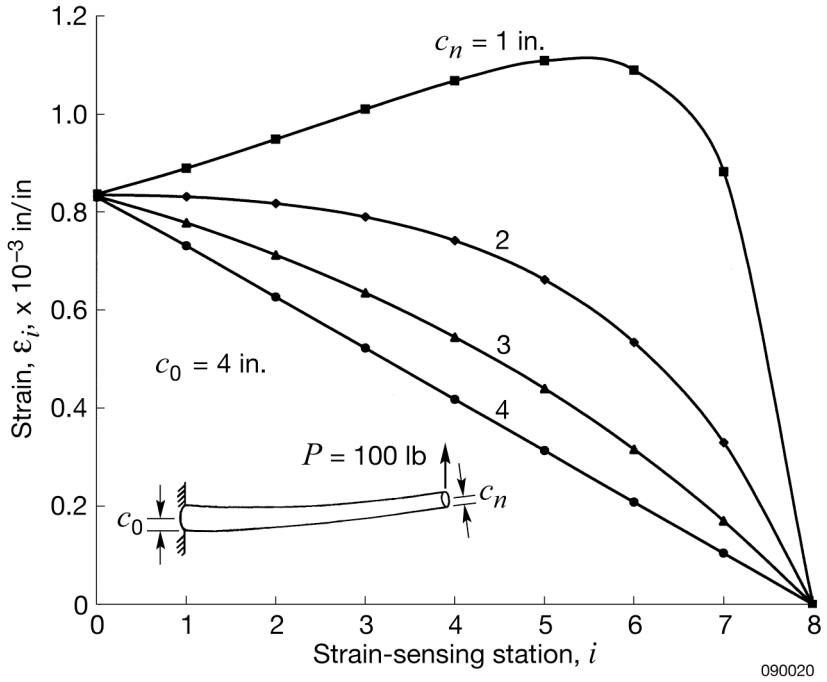

Figure 10. Bending strains calculated from SPAR element stress outputs for different tapered cantilever tubular beams; n = 8; P = 100 lb.

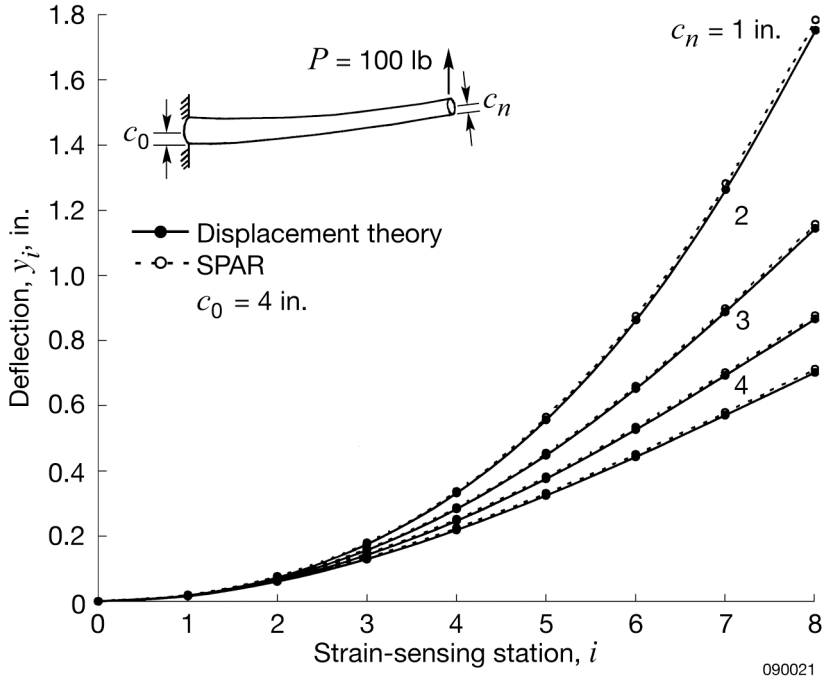

Figure 11. Comparison of deflections calculated from Ko displacement theory with those calculated from SPAR program for different tapered cantilever tubular beams; n = 8; P = 100 lb.

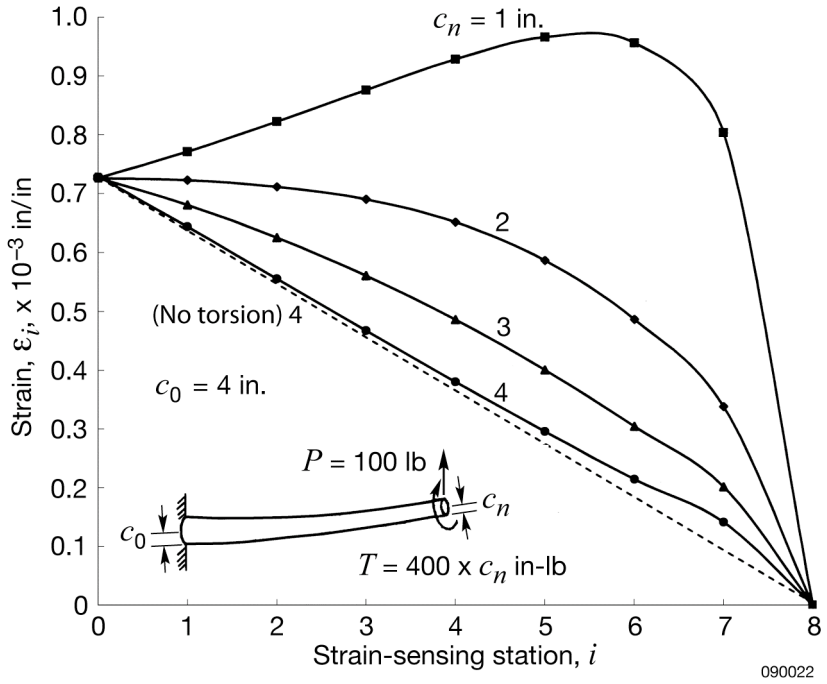

(a) Front strain-sensing line.

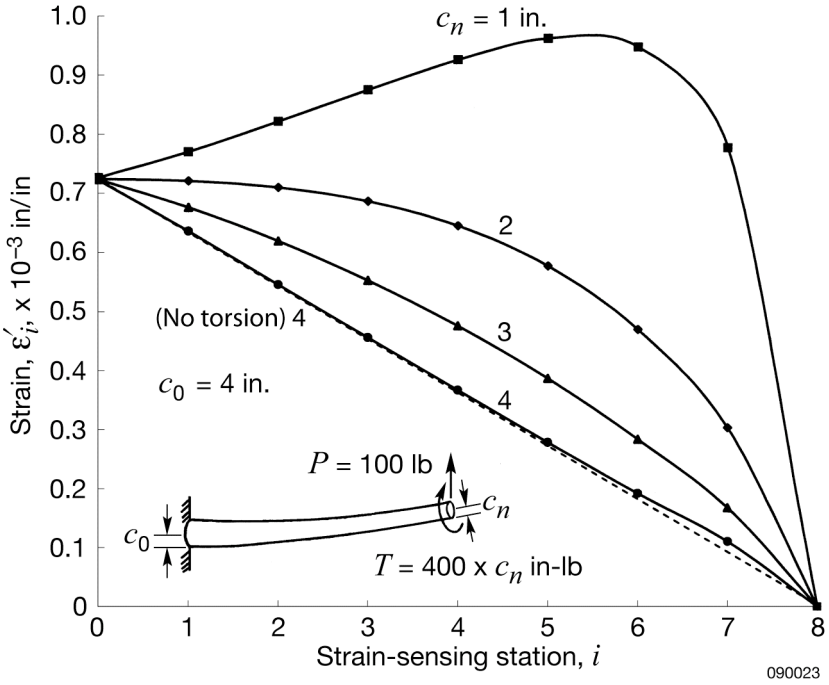

(b) Rear strain-sensing line.

Figure 12. SPAR-generated strains, $\{\varepsilon_i, \varepsilon'_i\}$, along front and rear strain-sensing lines on different tapered cantilever tubular beams; n = 8; P = 100 lb, $T = 400 \times c_n$ in-lb.

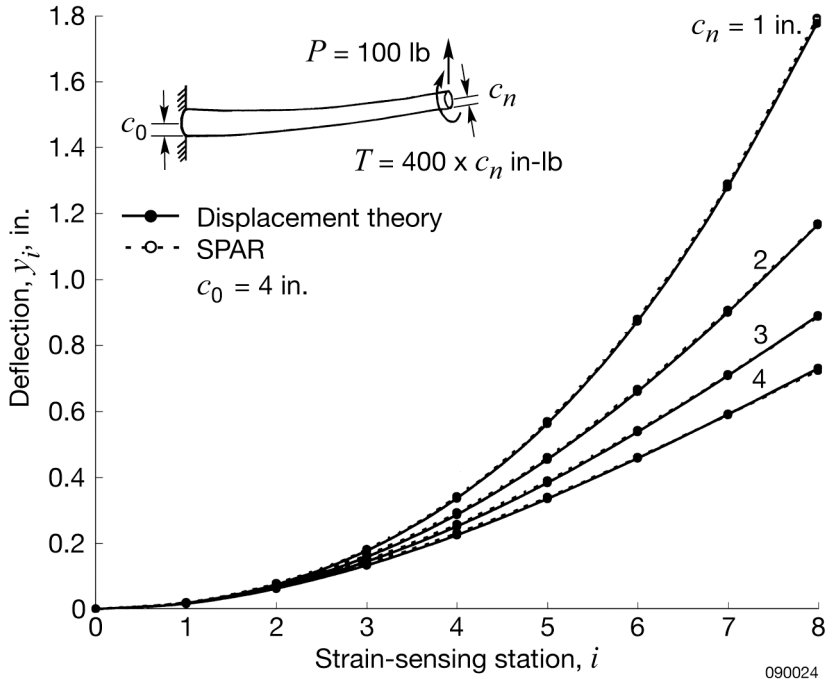

(a) Front strain-sensing line.

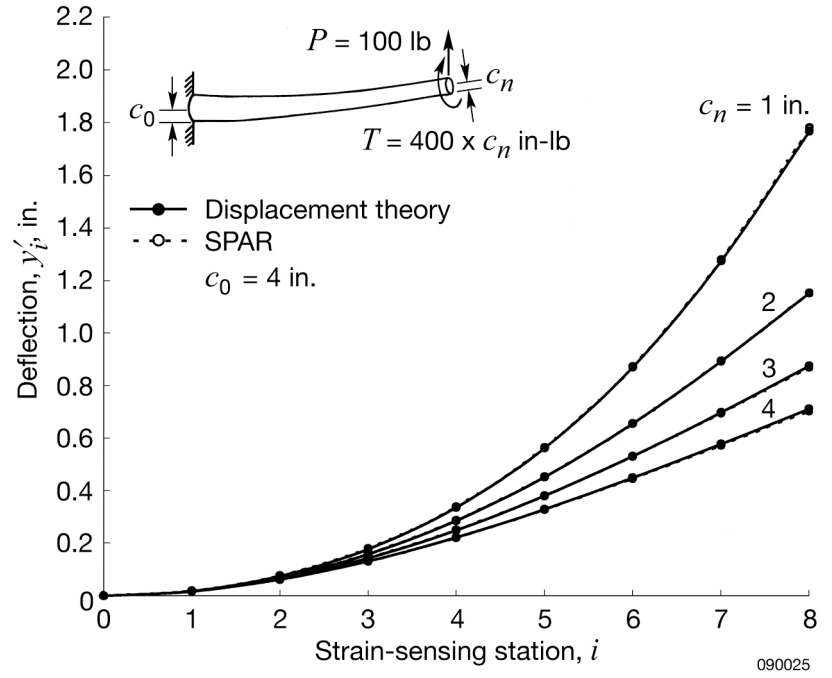

(b) Rear strain-sensing line.

Figure 13. Comparison of deflections along strain-sensing lines calculated from Ko displacement theory with those calculated from SPAR program for different tapered cantilever tubular beams; n = 8; P = 100 lb, $T = 400 \times c_n$ in-lb.

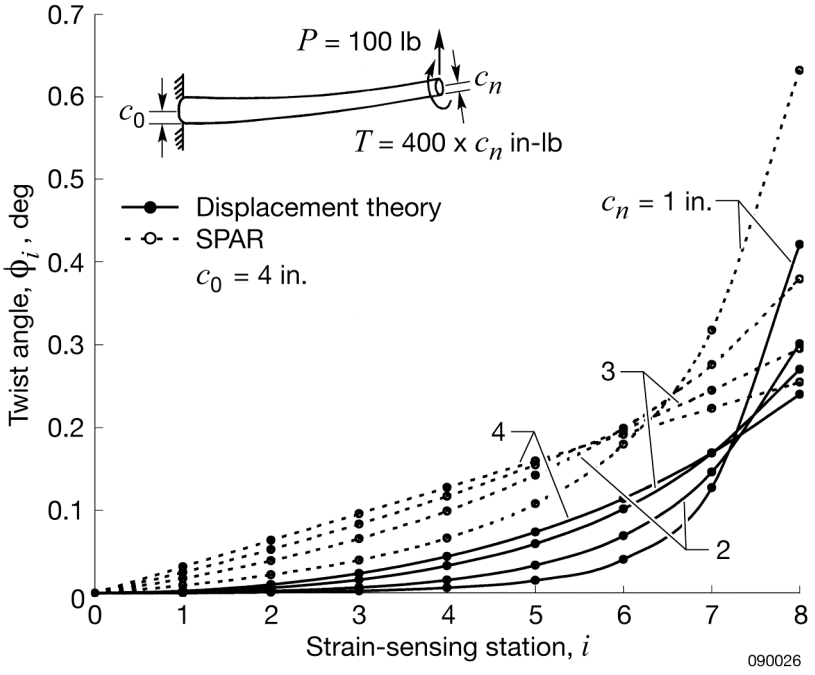

Figure 14. Comparison of cross-sectional twist angles calculated from Ko displacement theory with those calculated from SPAR program for different tapered cantilever tubular beams; $n = 8$; $P = 100$ lb, $T = 400 \times c_n$ in-lb.

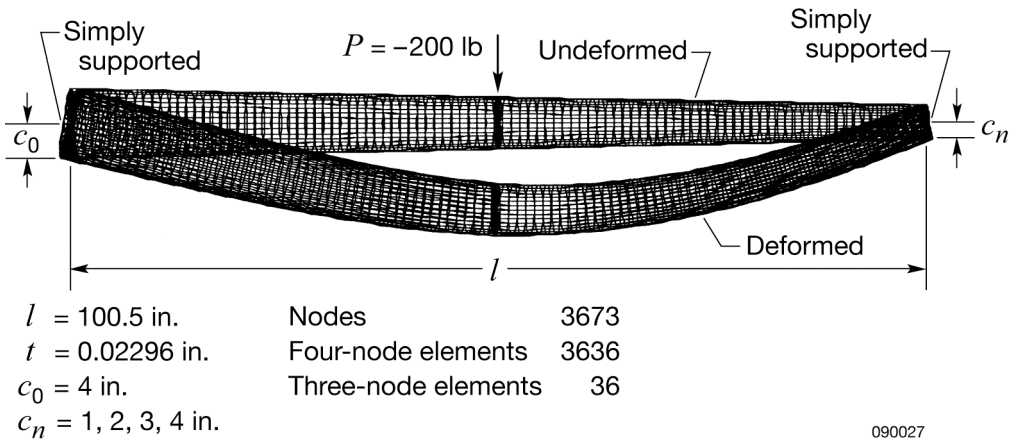

l	= 100.5 in.	Nodes	3673
t	= 0.02296 in.	Four-node elements	3636
c_0	= 4 in.	Three-node elements	36
c_n	= 1, 2, 3, 4 in.		

090027

(a) Both ends simply supported.

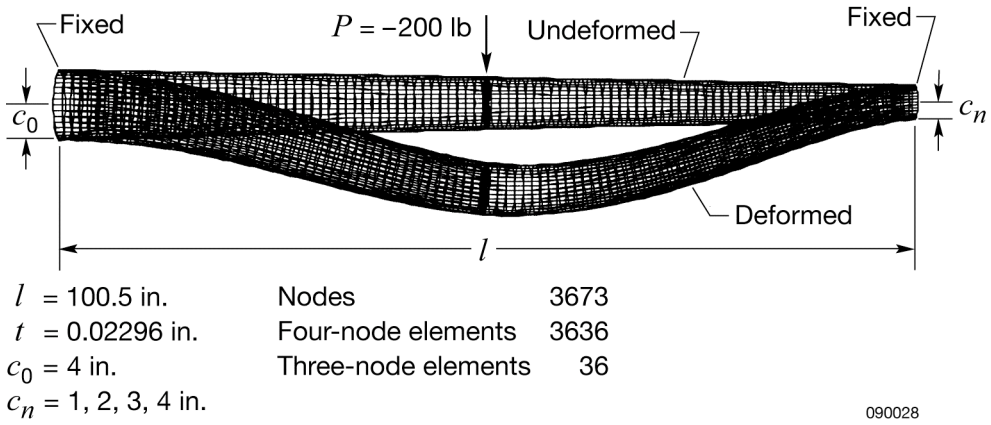

l	= 100.5 in.	Nodes	3673
t	= 0.02296 in.	Four-node elements	3636
c_0	= 4 in.	Three-node elements	36
c_n	= 1, 2, 3, 4 in.		

090028

(b) Both ends fixed.

Figure 15. Finite-element model for tapered tubular simple beam subjected to central downward vertical load of P = –200 lb.

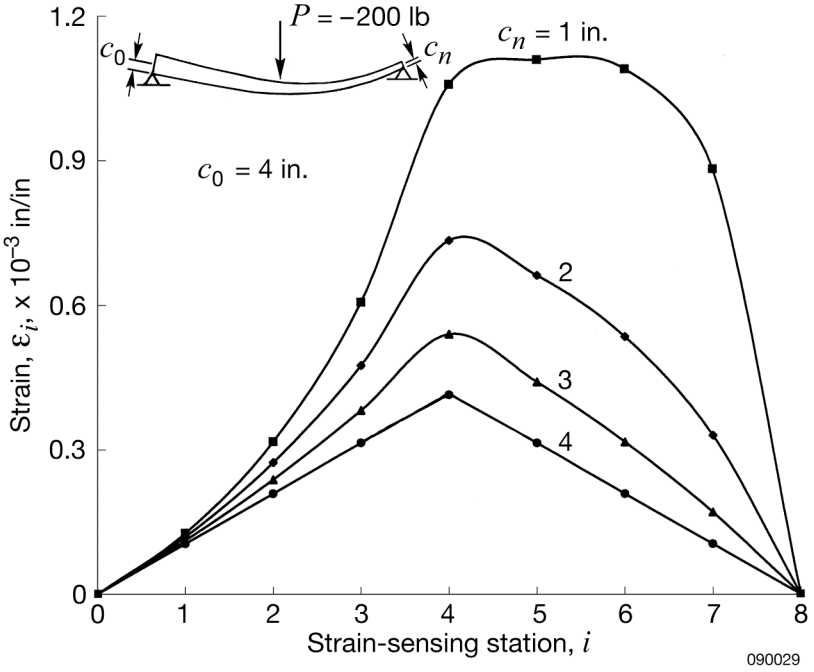

Figure 16. Bending strains calculated from SPAR element stress outputs for different tapered tubular simple beams; n = 8; two ends simply supported; P = 100 lb.

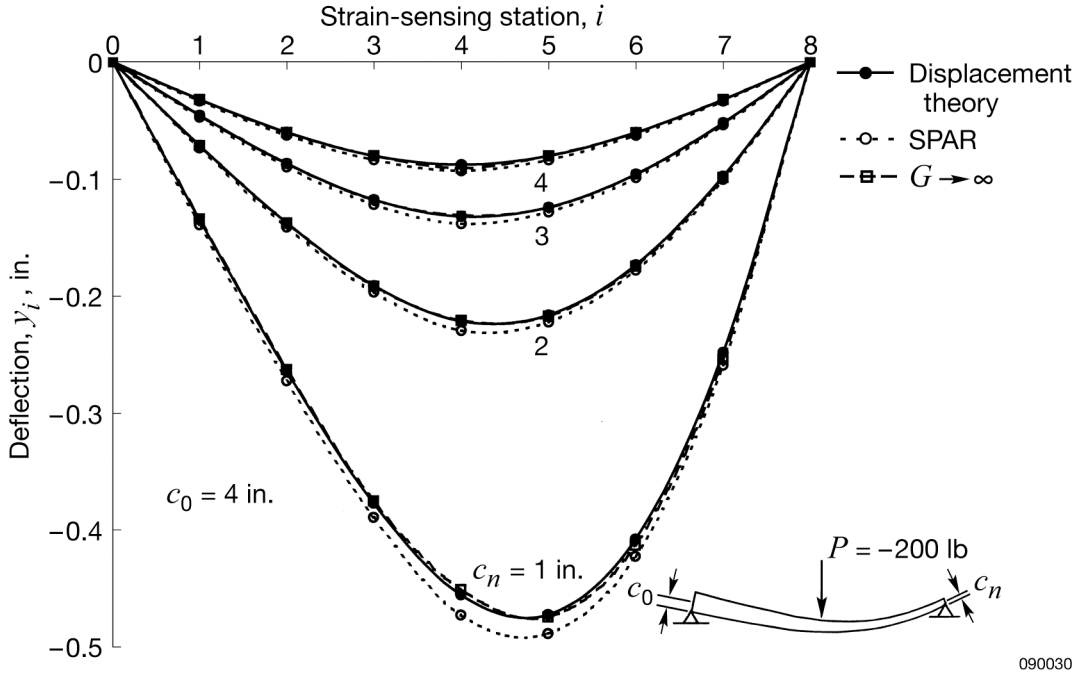

Figure 17. Comparison of deflections calculated from Ko displacement theory with those calculated from SPAR program for different tapered tubular simple beams; two ends simply supported; n = 8; P = 100 lb.

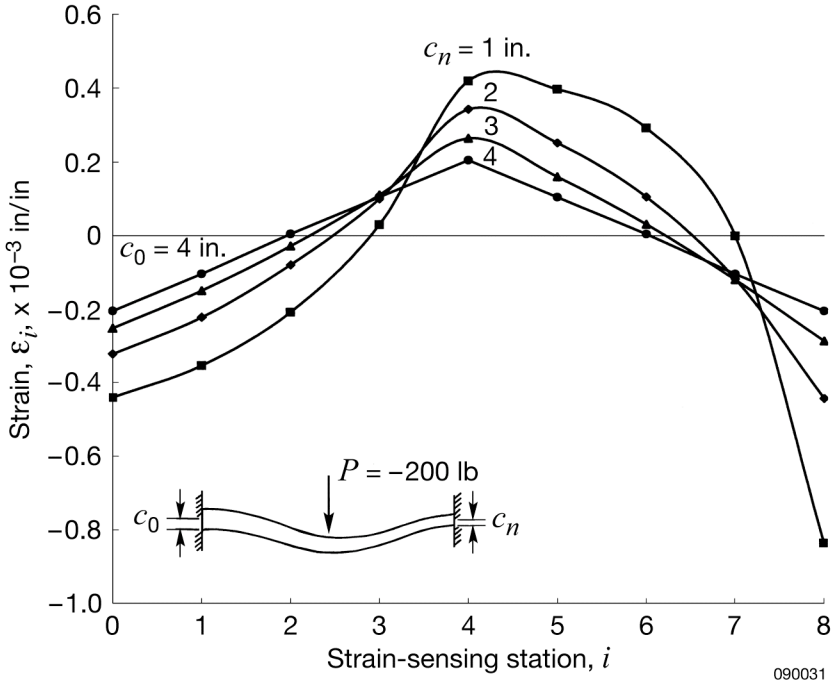

Figure 18. Bending strains calculated from SPAR element stress outputs for different tapered tubular simple beams; two ends fixed; n = 8; P = 100 lb.

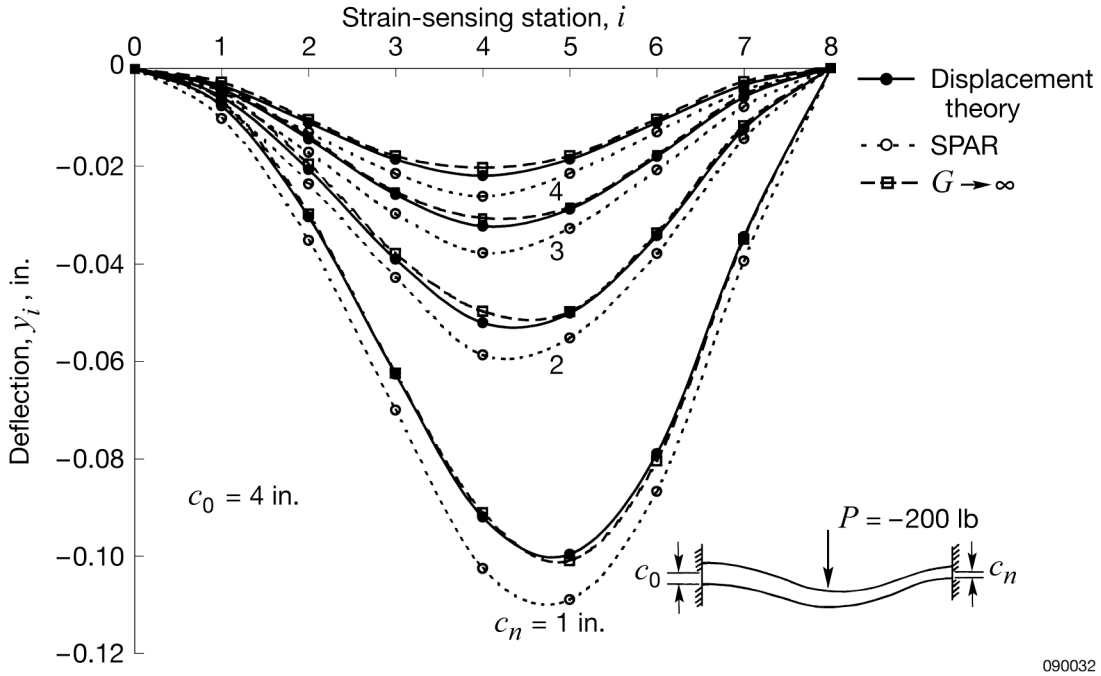

Figure 19. Comparison of deflections calculated from Ko displacement theory with those calculated from SPAR program for different tapered tubular simple beams; two ends fixed; n = 8; P = 100 lb.

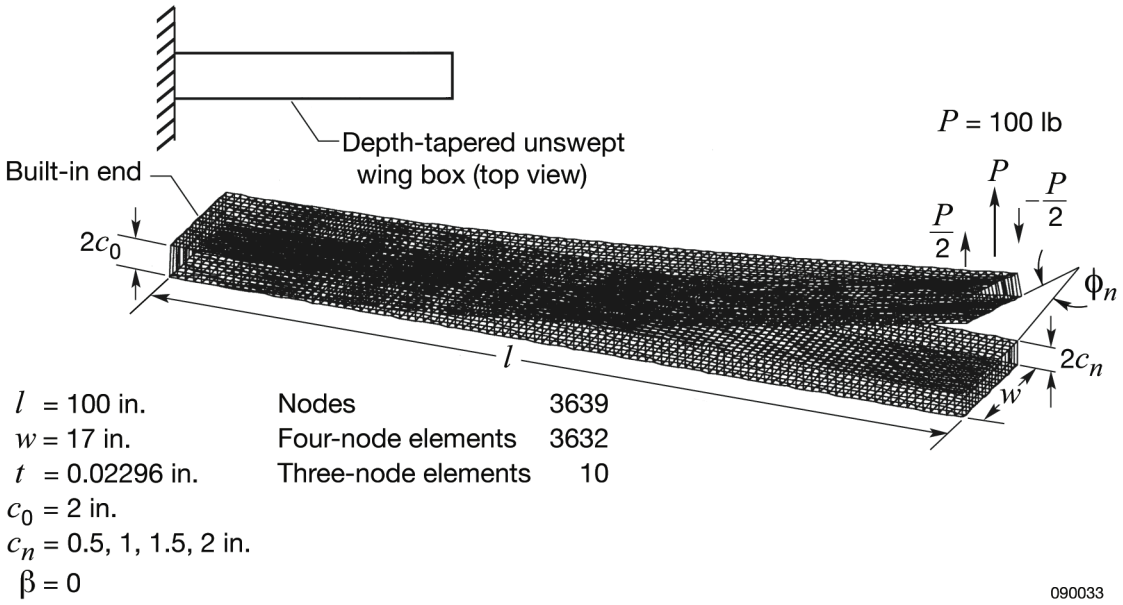

(a) Unswept wing box.

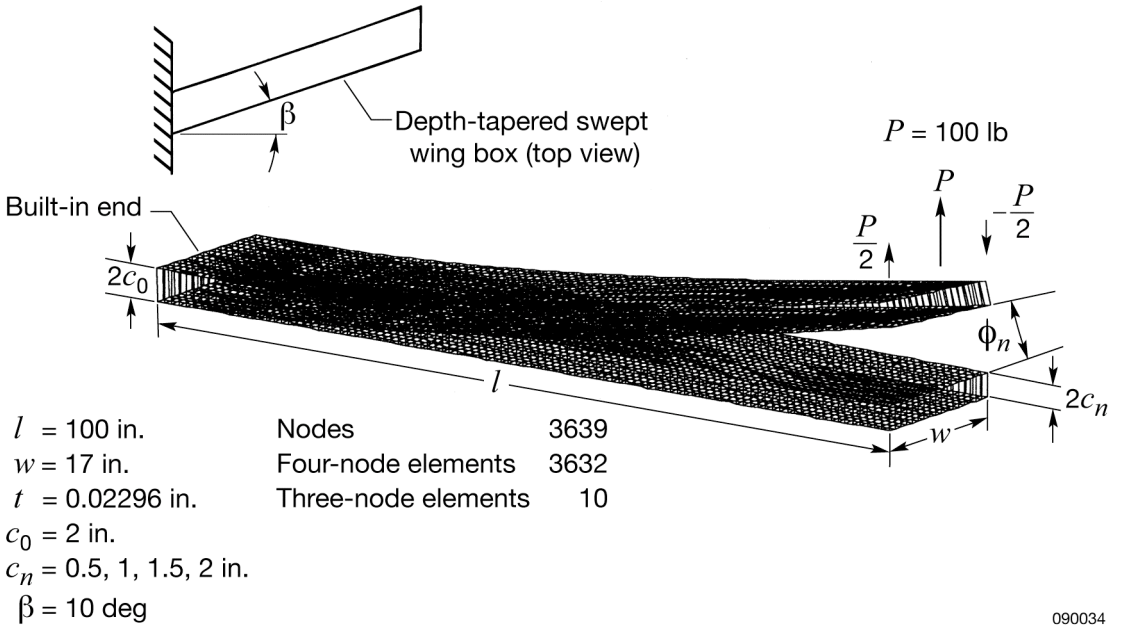

(b) Swept wing box.

Figure 20. Finite-element models for depth-tapered wing boxes subjected to bending and torsion; $P = 100$ lb; $T = 50 \times w$ in-lb.

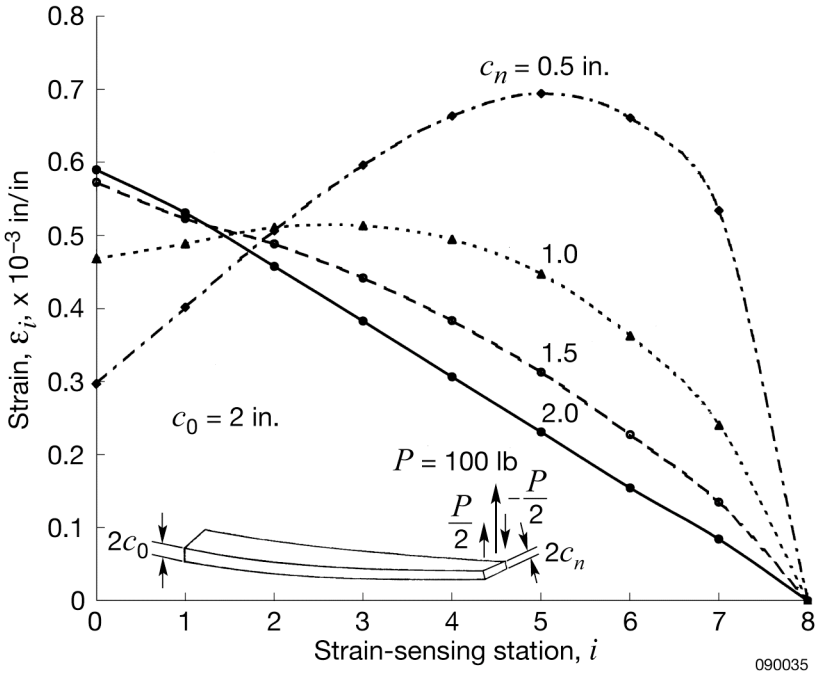

(a) Front strain-sensing line.

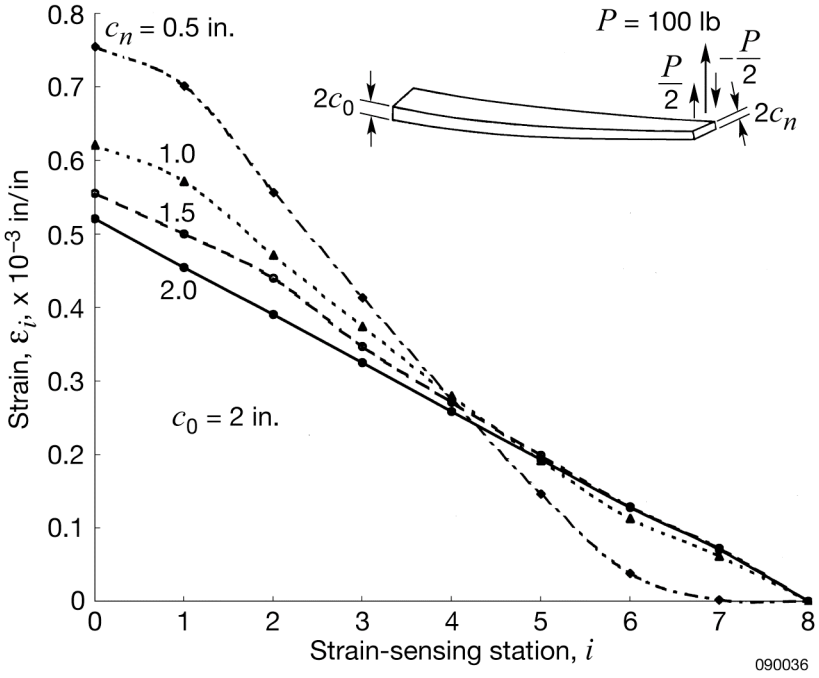

(b) Rear strain-sensing line.

Figure 21. SPAR-generated strains, $\{\varepsilon_i, \varepsilon_i'\}$, along front and rear strain-sensing lines on different depth-tapered unswept wing boxes; $n = 8$; $P = 100$ lb; $T = 50 \times w$ in-lb (clockwise).

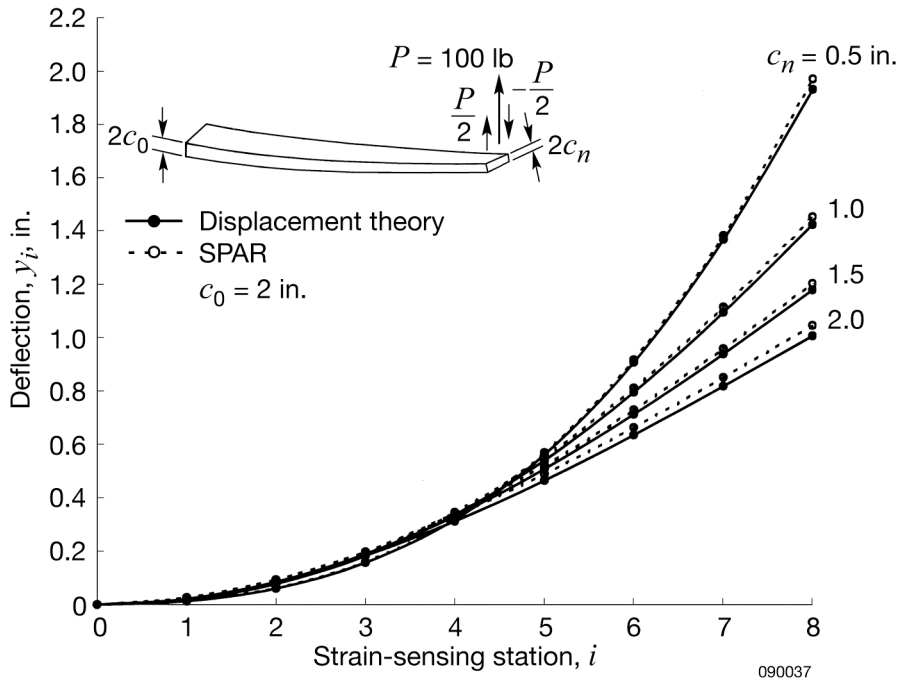

(a) Front strain-sensing line.

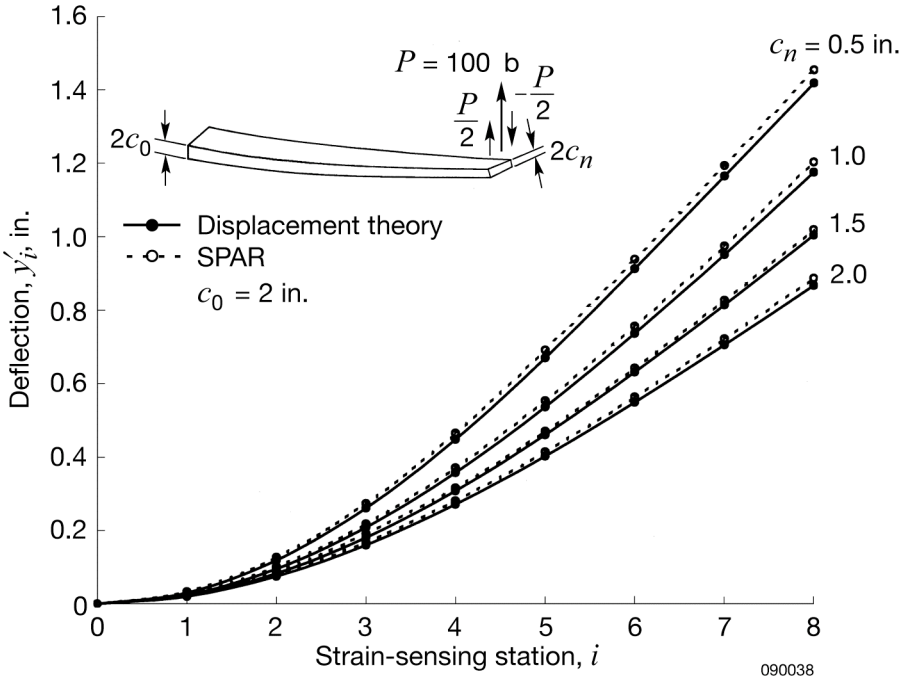

(b) Rear strain-sensing line.

Figure 22. Comparison of deflections, $\{y_i, y_i'\}$, along front and rear strain-sensing lines, calculated from Ko displacement theory with those calculated from SPAR program for different depth-tapered unswept wing boxes; $n = 8$; $P = 100$ lb; $T = 50 \times w$ in-lb (clockwise).

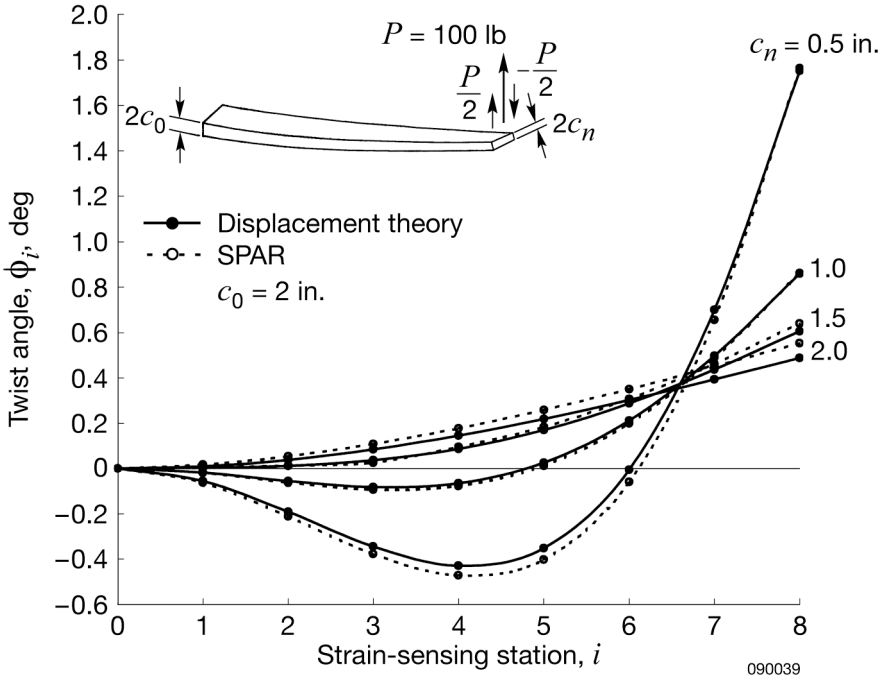

Figure 23. Comparison of cross-sectional twist angles calculated from Ko displacement theory with those calculated from SPAR program for different depth-tapered unswept wing boxes; $n = 8$; $P = 100$ lb; $T = 50 \times w$ in-lb (clockwise).

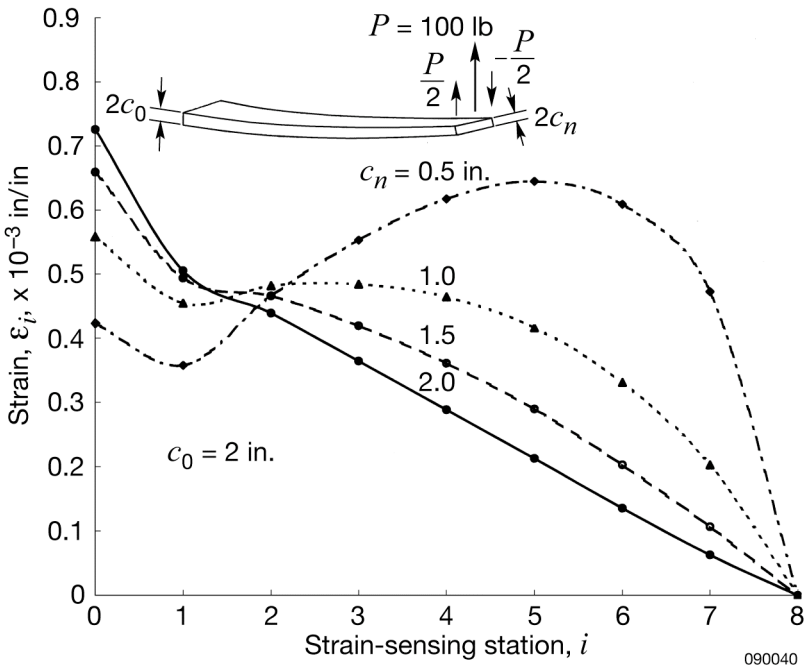

(a) Front strain-sensing line.

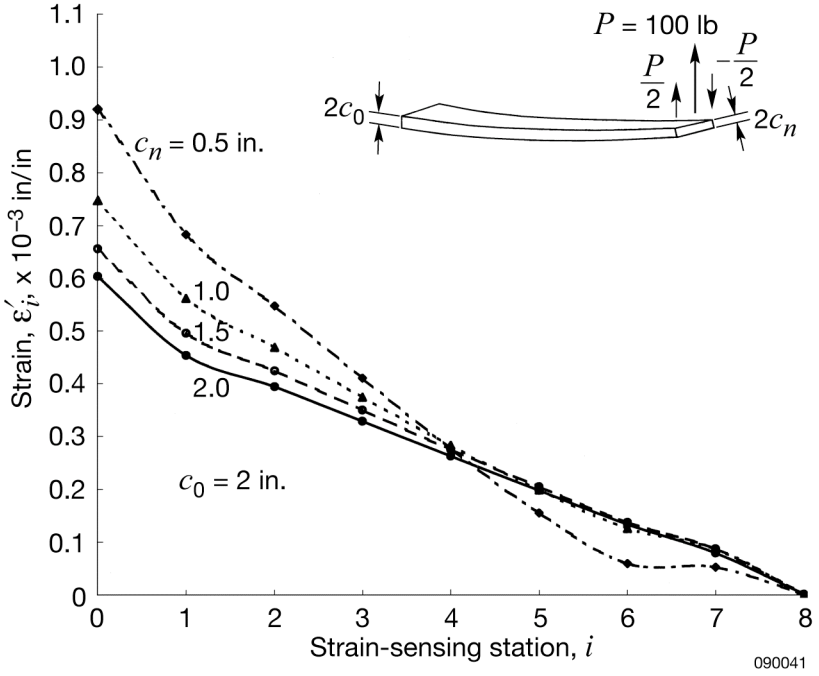

(b) Rear strain-sensing line.

Figure 24. SPAR-generated strains, $\{\varepsilon_i, \varepsilon_i'\}$, along front and rear strain-sensing lines on different depth-tapered swept wing boxes; $n = 8$; $P = 100$ lb; $T = 50 \times w$ in-lb (clockwise).

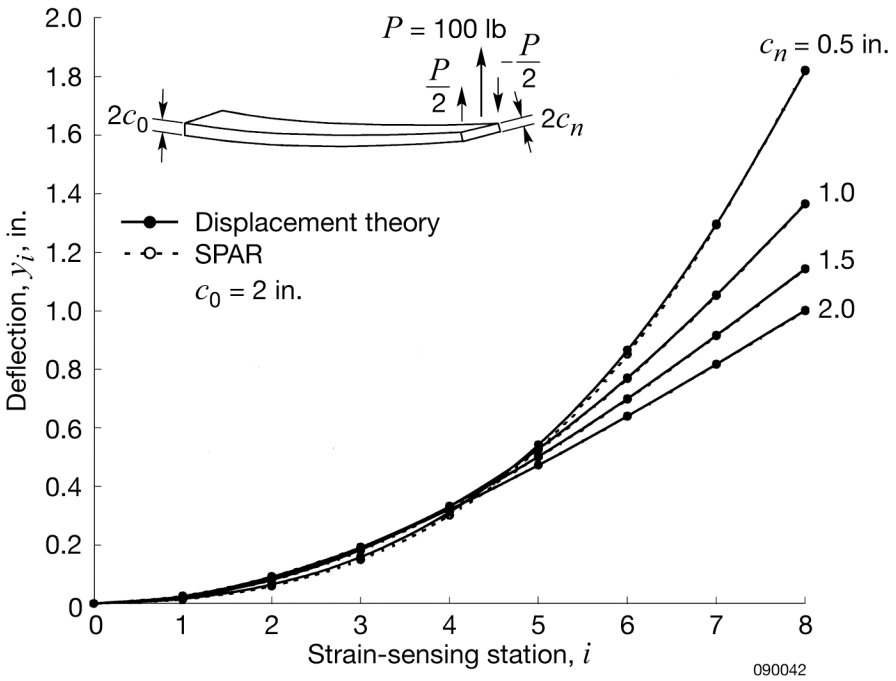

(a) Front strain-sensing line.

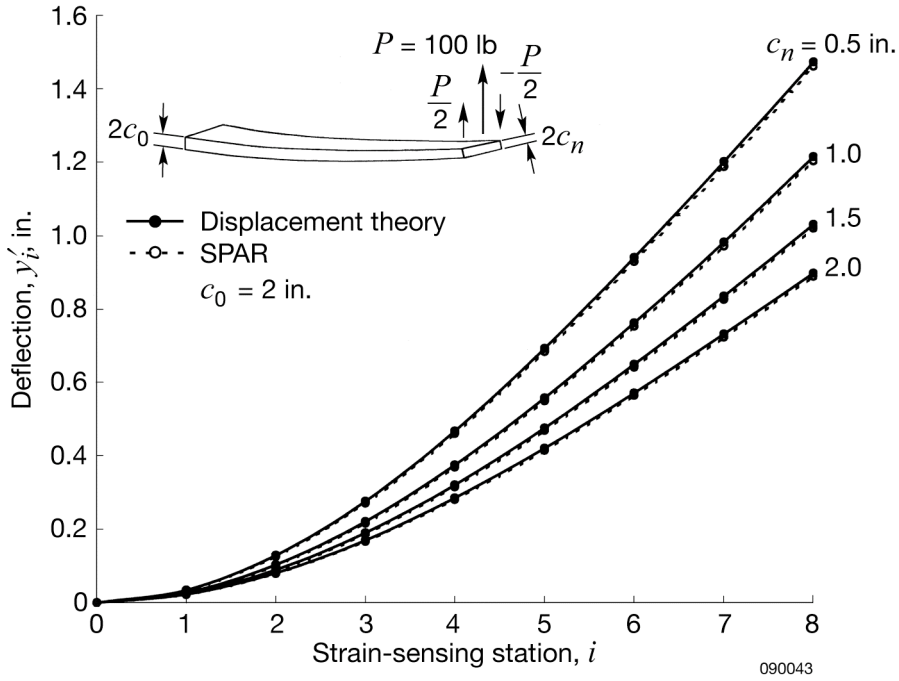

(b) Rear strain-sensing line.

Figure 25. Comparison of deflections, $\{y_i, y_i'\}$, along front and rear strain-sensing lines calculated from Ko displacement theory with those calculated from SPAR program for different depth-tapered swept wing boxes; $n = 8$; $P = 100$ lb; $T = 50 \times w$ in-lb (clockwise).

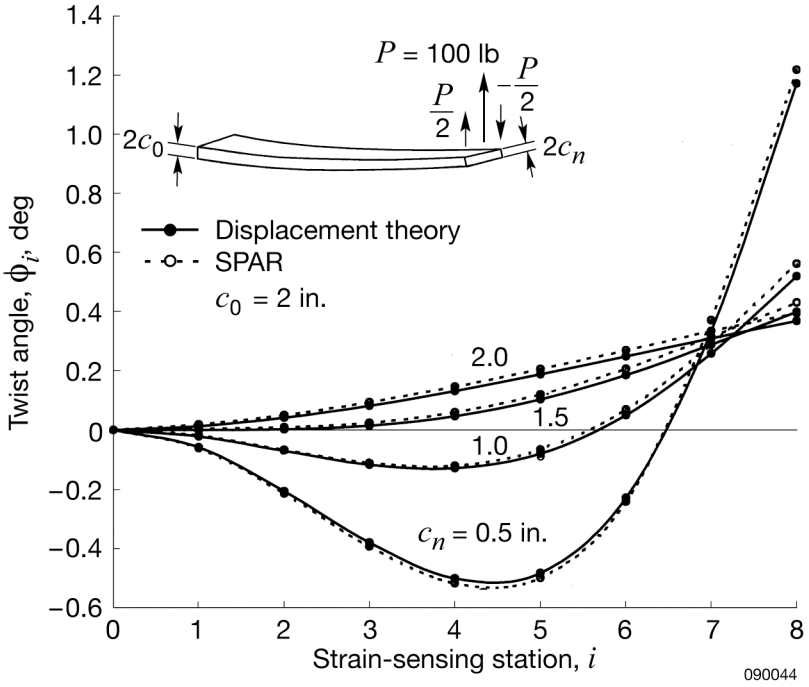

Figure 26. Comparison of cross-sectional twist angles calculated from Ko displacement theory with those calculated from SPAR program for different depth-tapered swept wing boxes; n = 8; P = 100 lb; $T = 50 \times w$ in-lb (clockwise).

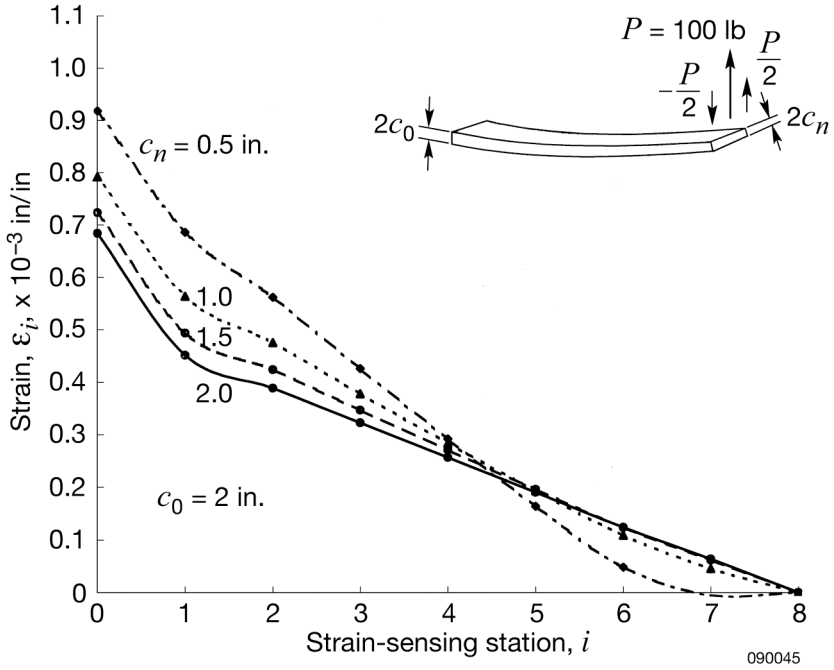

(a) Front strain-sensing line.

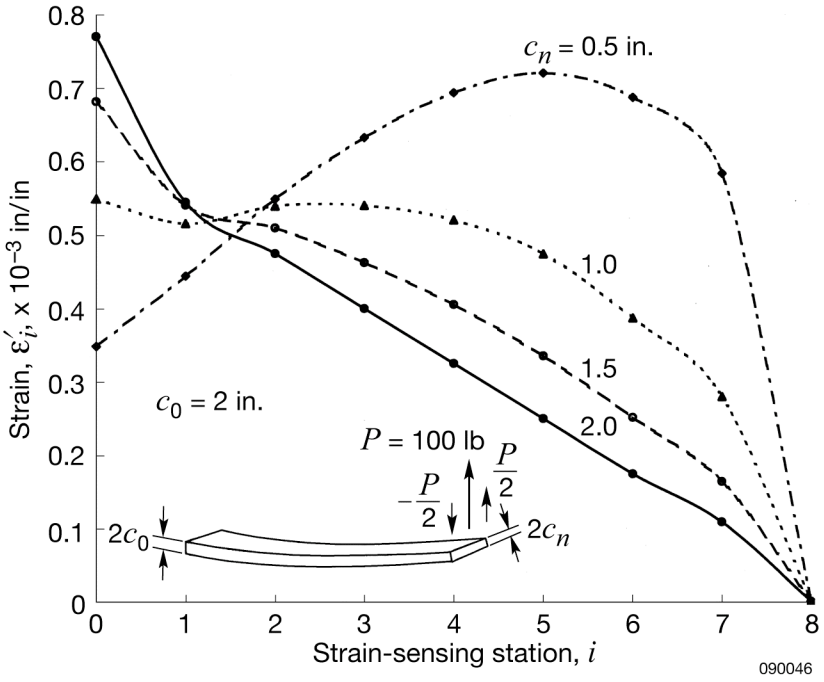

(b) Rear strain-sensing line.

Figure 27. SPAR-generated strains, $\{\varepsilon_i, \varepsilon_i'\}$, along front and rear strain-sensing lines on different depth-tapered swept wing boxes; $n = 8$; $P = 100$ lb; $T = -(50 \times w)$ in-lb (counterclockwise).

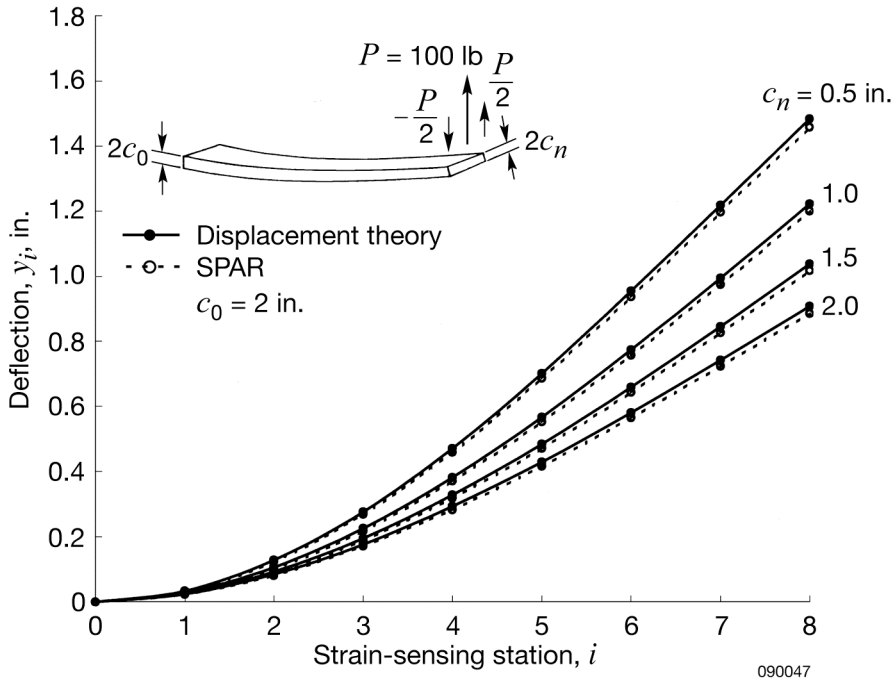

(a) Front strain-sensing line.

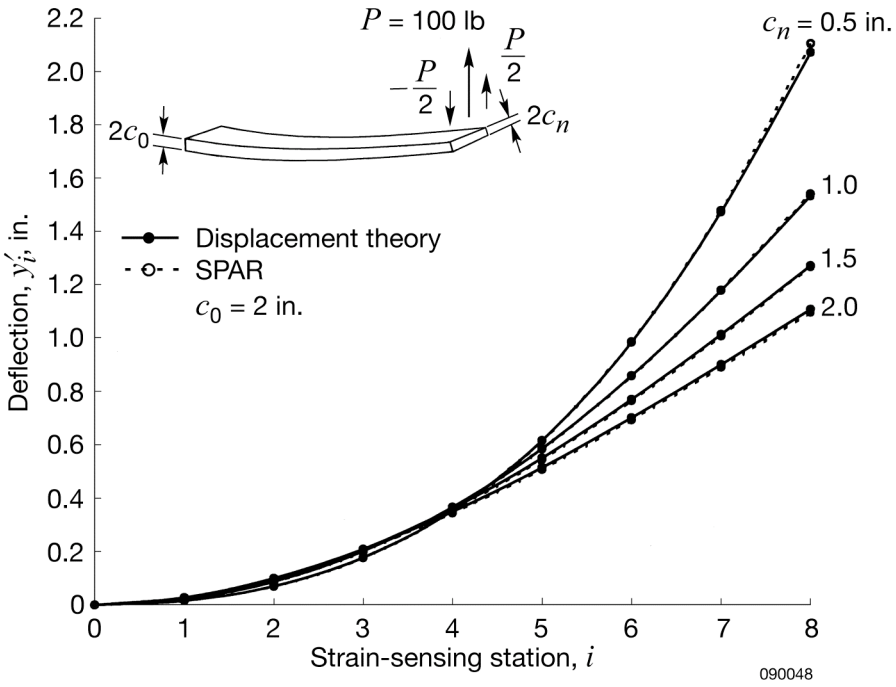

(b) Rear strain-sensing line.

Figure 28. Comparison of deflections, $\{ y_i, y_i' \}$, along front and rear strain-sensing lines calculated from Ko displacement theory with those calculated from SPAR program for different depth-tapered swept wing boxes; $n = 8$; $P = 100$ lb; $T = -(50 \times w)$ in-lb (counterclockwise).

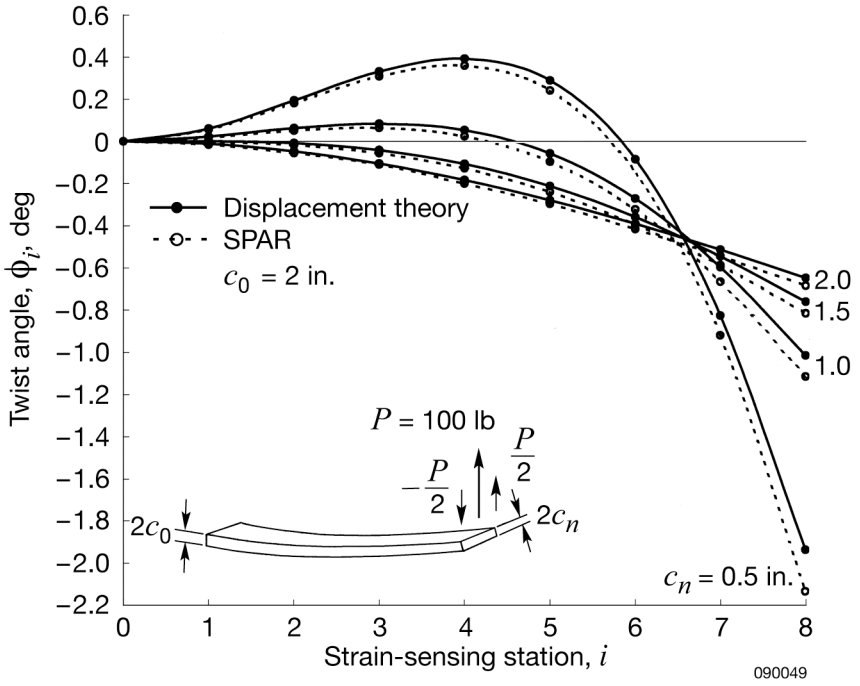

Figure 29. Comparison of cross-sectional twist angles calculated from Ko displacement theory with those calculated from SPAR program for different depth-tapered swept wing boxes; n = 8; P = 100 lb; $T = -(50 \times w)$ in-lb (counterclockwise).

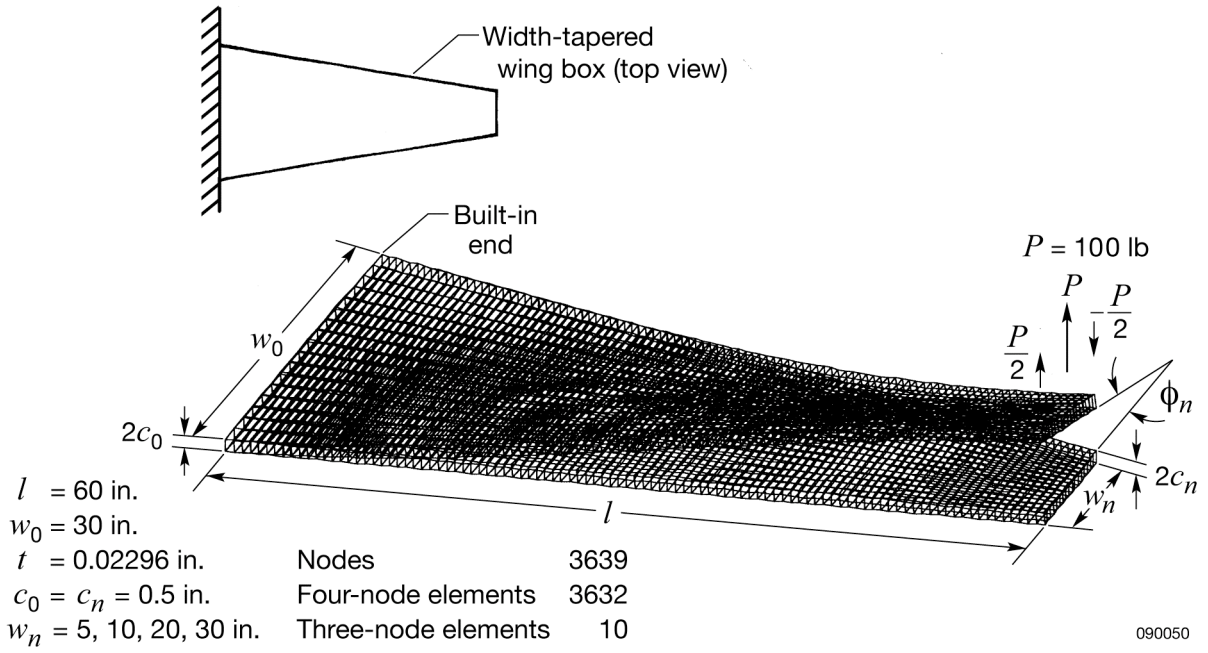

Figure 30. Finite-element model for a width-tapered unswept wing box subjected to bending and torsion; P = 100 lb; $T = 50 \times w_n$ in-lb.

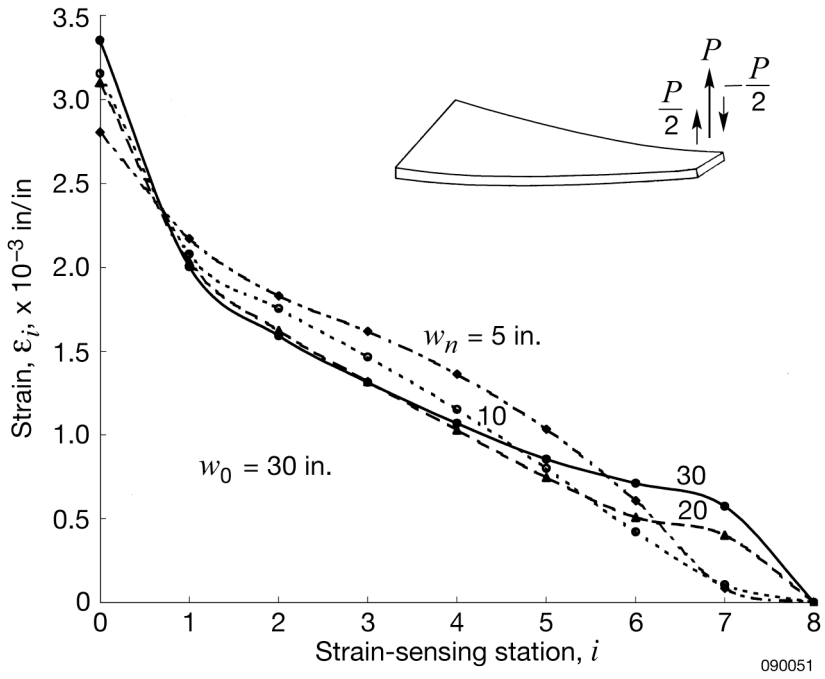

(a) Front strain-sensing line.

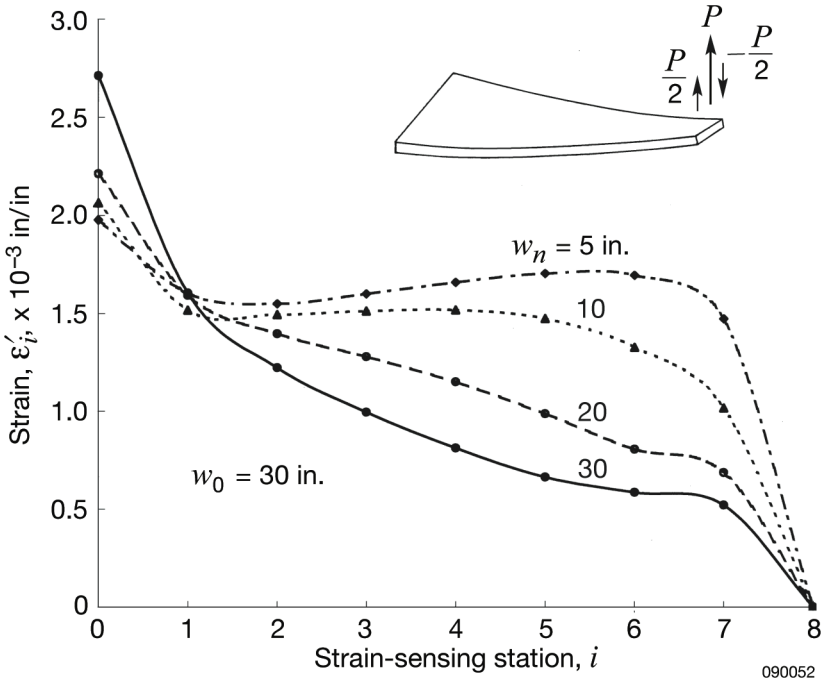

(b) Rear strain-sensing line.

Figure 31. SPAR-generated strains, $\{\varepsilon_i, \varepsilon'_i\}$, along front and rear strain-sensing lines on different width-tapered unswept wing boxes; n = 8; P = 100 lb; $T = 50 \times w_n$ in-lb (clockwise).

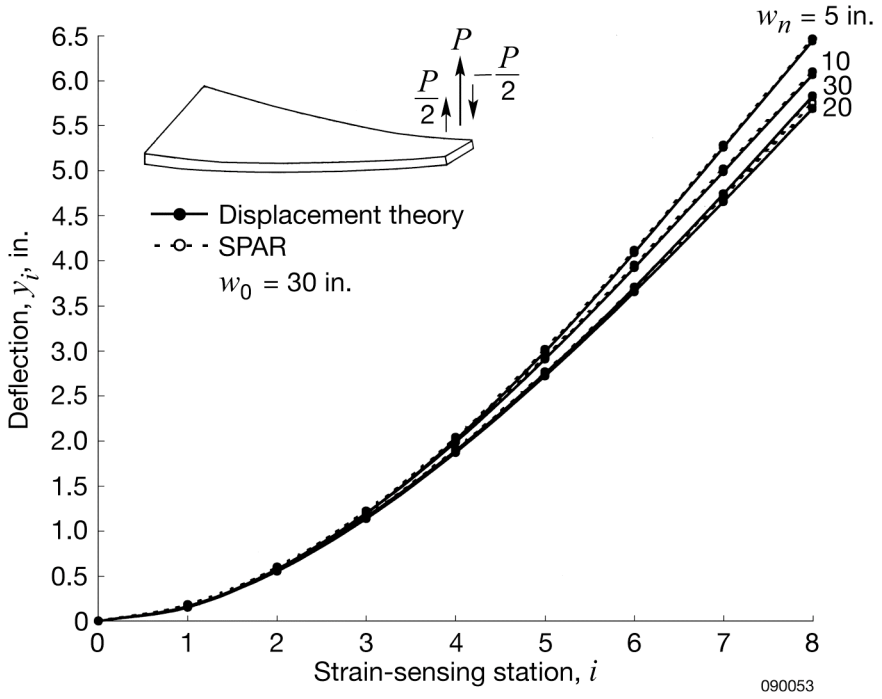

(a) Front strain-sensing line.

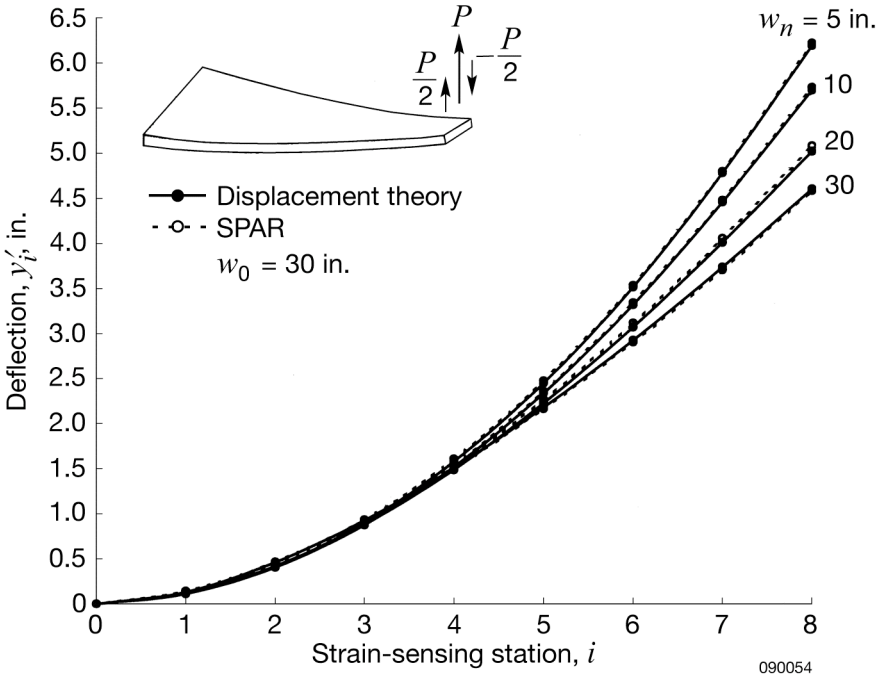

(b) Rear strain-sensing line.

Figure 32. Comparison of deflections, $\{y_i, y_i'\}$, along front and rear strain-sensing lines calculated from Ko displacement theory with those calculated from SPAR program for different width-tapered unswept wing boxes; $n = 8$; $P = 100$ lb; $T = 50 \times w_n$ in-lb (clockwise).

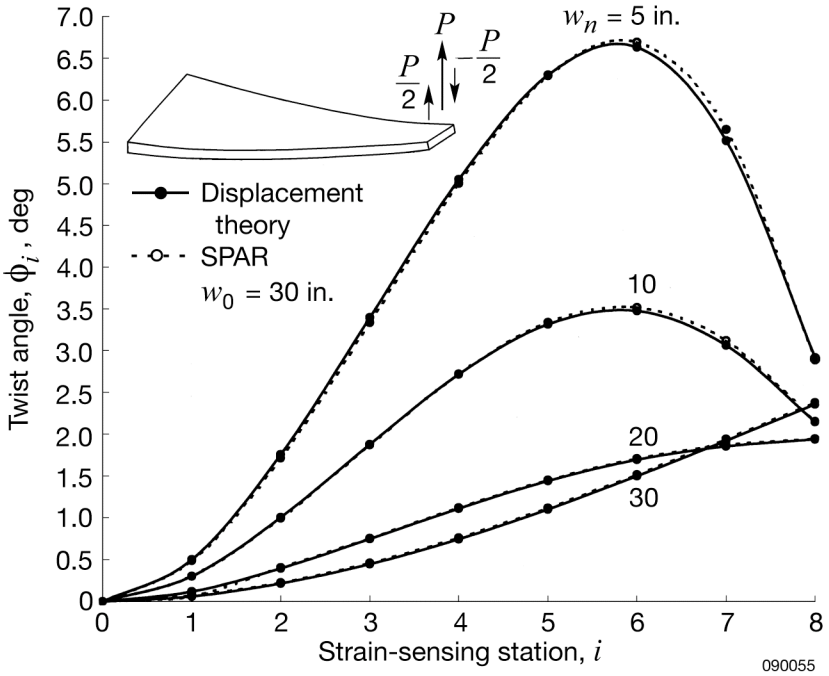

Figure 33. Comparison of cross-sectional twist angles calculated from Ko displacement theory with those calculated from SPAR program for different width-tapered unswept wing boxes; $n = 8$; $P = 100$ lb; $T = 50 \times w_n$ in-lb (clockwise).

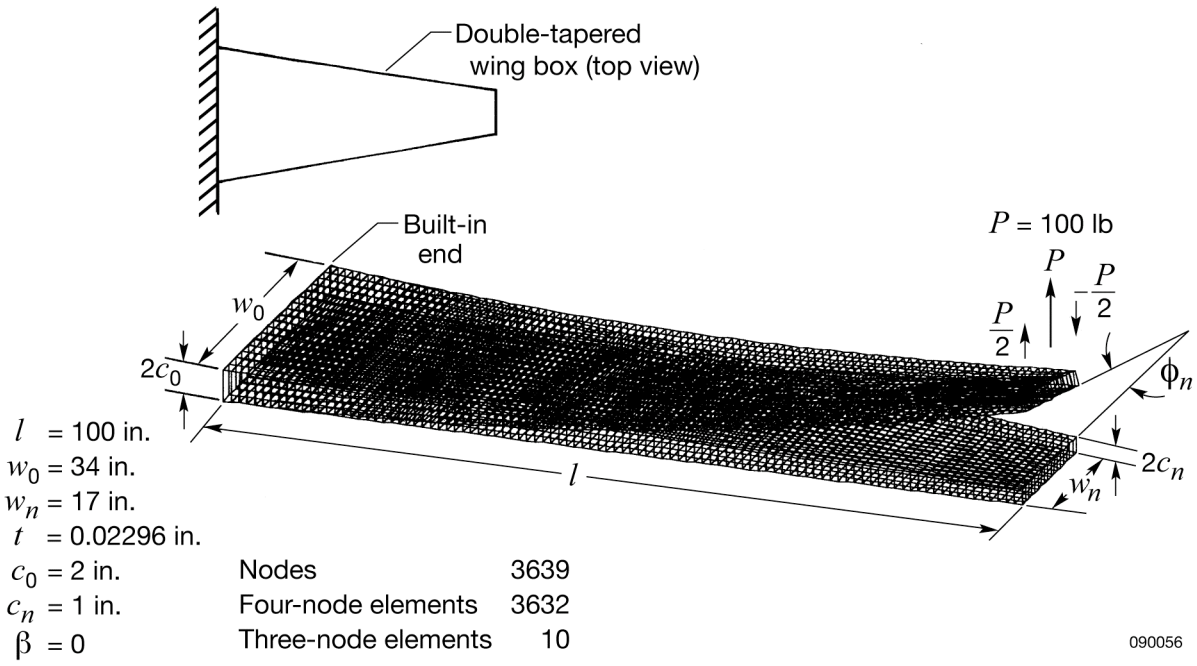

Figure 34. Finite-element model for a double-tapered wing box subjected to bending and torsion; P = 100 lb, $T = 50 \times w_n$ in-lb.

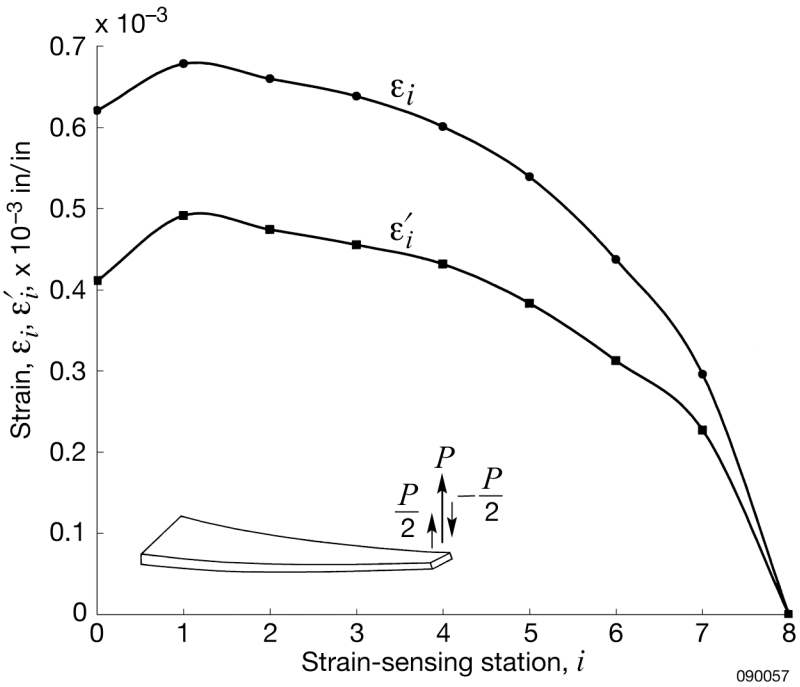

Figure 35. SPAR-generated strains, $\{\varepsilon_i, \varepsilon'_i\}$, along front and rear strain-sensing lines on a double-tapered unswept wing box; n = 8; P = 100 lb; $T = 50 \times w_n$ in-lb (clockwise).

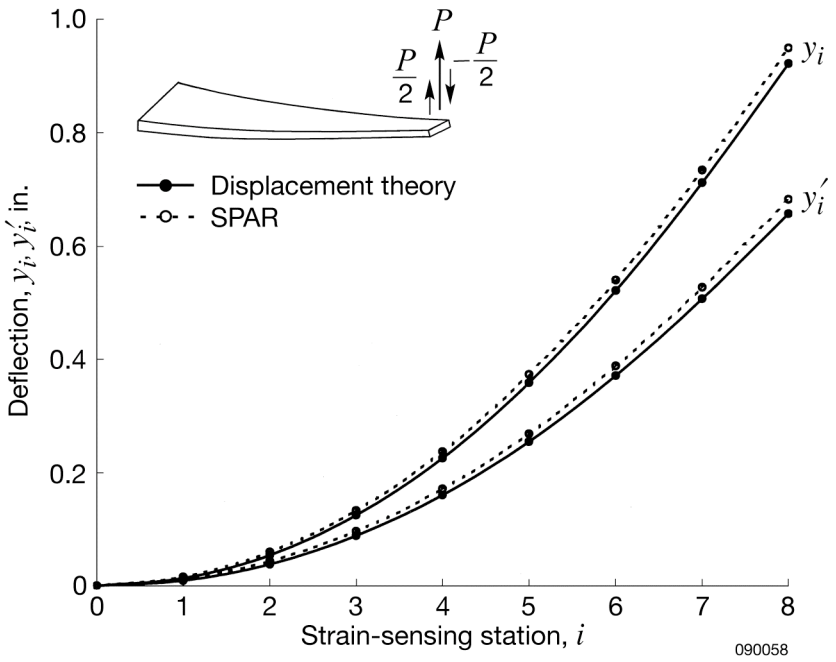

Figure 36. Comparison of deflections, $\{y_i, y_i'\}$, along front and rear strain-sensing lines calculated from Ko displacement theory with those calculated from SPAR program, for a double-tapered unswept wing box; $n = 8$; $P = 100$ lb; $T = 50 \times w_n$ in-lb (clockwise).

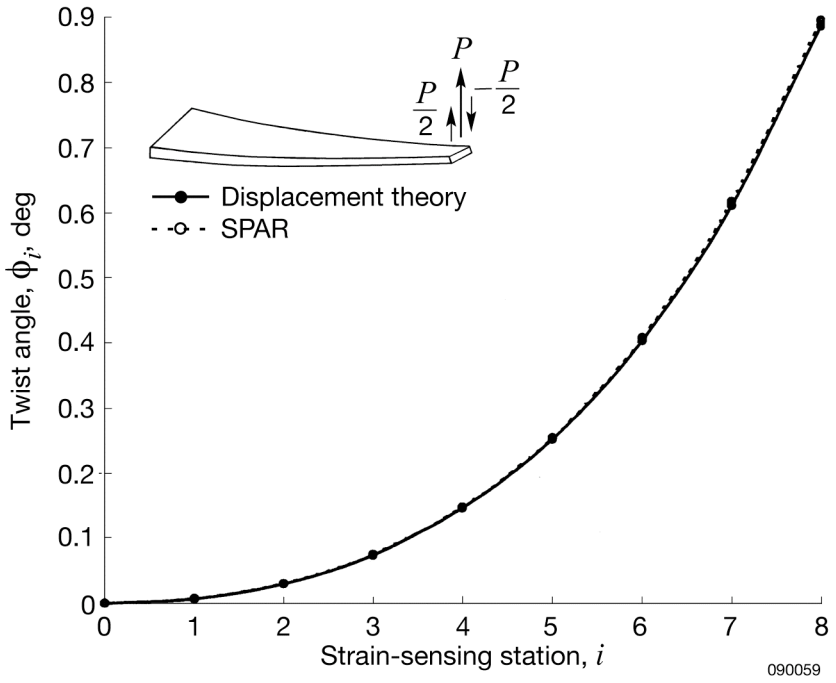

Figure 37. Comparison of cross-sectional twist angles calculated from Ko displacement theory with those calculated from SPAR program for a double-tapered unswept wing box; $n = 8$; $P = 100$ lb; $T = 50 \times w_n$ in-lb (clockwise).

APPENDIX A
DERIVATION OF DEFLECTION EQUATIONS FOR NONUNIFORM CANTILEVER BEAMS

Slope equation (11) and deflection equation (13) for nonuniform cantilever beams are duplicated here as follows:

Slope equation,

$$\tan\theta_i = \Delta l\left[\frac{\varepsilon_{i-1}-\varepsilon_i}{c_{i-1}-c_i}+\frac{\varepsilon_{i-1}c_i-\varepsilon_i c_{i-1}}{(c_{i-1}-c_i)^2}\log_e\frac{c_i}{c_{i-1}}\right]+\tan\theta_{i-1} \tag{A1}$$

Deflection equation,

$$y_i = (\Delta l)^2\left\{\frac{\varepsilon_{i-1}-\varepsilon_i}{2(c_{i-1}-c_i)}-\frac{\varepsilon_{i-1}c_i-\varepsilon_i c_{i-1}}{(c_{i-1}-c_i)^3}\left[c_i\log_e\frac{c_i}{c_{i-1}}+(c_{i-1}-c_i)\right]\right\}+y_{i-1}+\Delta l\tan\theta_{i-1} \tag{A2}$$

Writing out equation (A2) for different indices, *i,* and making use of the indicial relationships expressed in equations (A1) and (A2), we obtain the following:

For $i = 1$,

$$y_1 = (\Delta l)^2\left\{\frac{\varepsilon_0-\varepsilon_1}{2(c_0-c_1)}-\frac{\varepsilon_0 c_1-\varepsilon_1 c_0}{(c_0-c_1)^3}\left[c_1\log_e\frac{c_1}{c_0}+(c_0-c_1)\right]\right\}+y_0+\Delta l\tan\theta_0 \tag{A2-a}$$

For $i = 2$,

$$y_2 = (\Delta l)^2 \left\{ \frac{\varepsilon_1 - \varepsilon_2}{2(c_1 - c_2)} - \frac{\varepsilon_1 c_2 - \varepsilon_2 c_1}{(c_1 - c_2)^3} \left[c_2 \log_e \frac{c_2}{c_1} + (c_1 - c_2) \right] \right\} + y_1 + \Delta l \tan\theta_1$$

$$= (\Delta l)^2 \left\{ \frac{\varepsilon_1 - \varepsilon_2}{2(c_1 - c_2)} - \frac{\varepsilon_1 c_2 - \varepsilon_2 c_1}{(c_1 - c_2)^3} \left[c_2 \log_e \frac{c_2}{c_1} + (c_1 - c_2) \right] \right\}$$

$$+ \overbrace{(\Delta l)^2 \left\{ \frac{\varepsilon_0 - \varepsilon_1}{2(c_0 - c_1)} - \frac{\varepsilon_0 c_1 - \varepsilon_1 c_0}{(c_0 - c_1)^3} \left[c_1 \log_e \frac{c_1}{c_0} + (c_0 - c_1) \right] \right\}}^{y_1} + y_0 + \Delta l \tan\theta_0$$

$$+ \overbrace{(\Delta l)^2 \left[\frac{\varepsilon_0 - \varepsilon_1}{c_0 - c_1} + \frac{\varepsilon_0 c_1 - \varepsilon_1 c_0}{(c_0 - c_1)^2} \log_e \frac{c_1}{c_0} \right]}^{\Delta l \tan\theta_1} + \Delta l \tan\theta_0$$

$$= (\Delta l)^2 \left\{ \frac{\varepsilon_1 - \varepsilon_2}{2(c_1 - c_2)} - \frac{\varepsilon_1 c_2 - \varepsilon_2 c_1}{(c_1 - c_2)^3} \left[c_2 \log_e \frac{c_2}{c_1} + (c_1 - c_2) \right] + \frac{\varepsilon_0 - \varepsilon_1}{2(c_0 - c_1)} - \frac{\varepsilon_0 c_1 - \varepsilon_1 c_0}{(c_0 - c_1)^3} \left[c_1 \log_e \frac{c_1}{c_0} + (c_0 - c_1) \right] \right\}$$

$$+ (\Delta l)^2 \left[\frac{\varepsilon_0 - \varepsilon_1}{c_0 - c_1} + \frac{\varepsilon_0 c_1 - \varepsilon_1 c_0}{(c_0 - c_1)^2} \log_e \frac{c_1}{c_0} \right] + y_0 + 2\Delta l \tan\theta_0 \qquad \text{(A2-b)}$$

After the terms are grouped, equation (A2-b) becomes

$$y_2 = (\Delta l)^2 \left[\frac{\varepsilon_1 - \varepsilon_2}{2(c_1 - c_2)} + 3\frac{\varepsilon_0 - \varepsilon_1}{2(c_0 - c_1)} \right]$$

$$- (\Delta l)^2 \left\{ \frac{\varepsilon_1 c_2 - \varepsilon_2 c_1}{(c_1 - c_2)^3} \left[c_2 \log_e \frac{c_2}{c_1} + (c_1 - c_2) \right] + \frac{\varepsilon_0 c_1 - \varepsilon_1 c_0}{(c_0 - c_1)^3} \left[c_1 \log_e \frac{c_1}{c_0} + (c_0 - c_1) \right] \right\} \qquad \text{(A2-b′)}$$

$$+ (\Delta l)^2 \left[\frac{\varepsilon_0 c_1 - \varepsilon_1 c_0}{(c_0 - c_1)^2} \log_e \frac{c_1}{c_0} \right] + y_0 + 2\Delta l \tan\theta_0$$

For $i = 3$,

$$y_3 = (\Delta l)^2 \left\{ \frac{\varepsilon_2 - \varepsilon_3}{2(c_2 - c_3)} - \frac{\varepsilon_2 c_3 - \varepsilon_3 c_2}{(c_2 - c_3)^3} \left[c_3 \log_e \frac{c_3}{c_2} + (c_2 - c_3) \right] \right\} + y_2 + \Delta l \tan\theta_2$$

$$= (\Delta l)^2 \left\{ \frac{\varepsilon_2 - \varepsilon_3}{2(c_2 - c_3)} - \frac{\varepsilon_2 c_3 - \varepsilon_3 c_2}{(c_2 - c_3)^3} \left[c_3 \log_e \frac{c_3}{c_2} + (c_2 - c_3) \right] \right\}$$

$$+ \overbrace{\left\{ \begin{array}{l} (\Delta l)^2 \left\{ \frac{\varepsilon_1 - \varepsilon_2}{2(c_1 - c_2)} - \frac{\varepsilon_1 c_2 - \varepsilon_2 c_1}{(c_1 - c_2)^3} \left[c_2 \log_e \frac{c_2}{c_1} + (c_1 - c_2) \right] + \frac{\varepsilon_0 - \varepsilon_1}{2(c_0 - c_1)} - \frac{\varepsilon_0 c_1 - \varepsilon_1 c_0}{(c_0 - c_1)^3} \left[c_1 \log_e \frac{c_1}{c_0} + (c_0 - c_1) \right] \right\} \\ + (\Delta l)^2 \left[\frac{\varepsilon_0 - \varepsilon_1}{c_0 - c_1} + \frac{\varepsilon_0 c_1 - \varepsilon_1 c_0}{(c_0 - c_1)^2} \log_e \frac{c_1}{c_0} \right] + y_0 + 2\Delta l \tan\theta_0 \end{array} \right\}}^{y_2}$$

$$+ \overbrace{(\Delta l)^2 \left[\frac{\varepsilon_1 - \varepsilon_2}{c_1 - c_2} + \frac{\varepsilon_1 c_2 - \varepsilon_2 c_1}{(c_1 - c_2)^2} \log_e \frac{c_2}{c_1} + \frac{\varepsilon_0 - \varepsilon_1}{c_0 - c_1} + \frac{\varepsilon_0 c_1 - \varepsilon_1 c_0}{(c_0 - c_1)^2} \log_e \frac{c_1}{c_0} \right] + \Delta l \tan\theta_0}^{\Delta l \tan\theta_2}$$

$$= (\Delta l)^2 \left\{ \frac{\varepsilon_2 - \varepsilon_3}{2(c_2 - c_3)} - \frac{\varepsilon_2 c_3 - \varepsilon_3 c_2}{(c_2 - c_3)^3} \left[c_3 \log_e \frac{c_3}{c_2} + (c_2 - c_3) \right] + \frac{\varepsilon_1 - \varepsilon_2}{2(c_1 - c_2)} - \frac{\varepsilon_1 c_2 - \varepsilon_2 c_1}{(c_1 - c_2)^3} \left[c_2 \log_e \frac{c_2}{c_1} + (c_1 - c_2) \right] \right.$$
$$\left. + \frac{\varepsilon_0 - \varepsilon_1}{2(c_0 - c_1)} - \frac{\varepsilon_0 c_1 - \varepsilon_1 c_0}{(c_0 - c_1)^3} \left[c_1 \log_e \frac{c_1}{c_0} + (c_0 - c_1) \right] \right\}$$
$$+ (\Delta l)^2 \left[\frac{\varepsilon_1 - \varepsilon_2}{c_1 - c_2} + \frac{\varepsilon_1 c_2 - \varepsilon_2 c_1}{(c_1 - c_2)^2} \log_e \frac{c_2}{c_1} + 2\frac{\varepsilon_0 - \varepsilon_1}{c_0 - c_1} + 2\frac{\varepsilon_0 c_1 - \varepsilon_1 c_0}{(c_0 - c_1)^2} \log_e \frac{c_1}{c_0} \right] + y_0 + 3\Delta l \tan\theta_0 \qquad \text{(A2-c)}$$

After the terms are grouped, equation (A2-c) becomes

$$y_3 = (\Delta l)^2 \left[\frac{\varepsilon_2 - \varepsilon_3}{2(c_2 - c_3)} + 3\frac{\varepsilon_1 - \varepsilon_2}{2(c_1 - c_2)} + 5\frac{\varepsilon_0 - \varepsilon_1}{2(c_0 - c_1)} \right]$$
$$- (\Delta l)^2 \left\{ \frac{\varepsilon_2 c_3 - \varepsilon_3 c_2}{(c_2 - c_3)^3} \left[c_3 \log_e \frac{c_3}{c_2} + (c_2 - c_3) \right] + \frac{\varepsilon_1 c_2 - \varepsilon_2 c_1}{(c_1 - c_2)^3} \left[c_2 \log_e \frac{c_2}{c_1} + (c_1 - c_2) \right] \right.$$
$$\left. + \frac{\varepsilon_0 c_1 - \varepsilon_1 c_0}{(c_0 - c_1)^3} \left[c_1 \log_e \frac{c_1}{c_0} + (c_0 - c_1) \right] \right\} \qquad \text{(A2-c′)}$$
$$+ (\Delta l)^2 \left[\frac{\varepsilon_1 c_2 - \varepsilon_2 c_1}{(c_1 - c_2)^2} \log_e \frac{c_2}{c_1} + 2\frac{\varepsilon_0 c_1 - \varepsilon_1 c_0}{(c_0 - c_1)^2} \log_e \frac{c_1}{c_0} \right] + y_0 + 3\Delta l \tan\theta_0$$

For $i = 4$,

$$y_4 = (\Delta l)^2 \left\{ \frac{\varepsilon_3 - \varepsilon_4}{2(c_3 - c_4)} - \frac{\varepsilon_3 c_4 - \varepsilon_4 c_3}{(c_3 - c_4)^3} \left[c_4 \log_e \frac{c_4}{c_3} + (c_3 - c_4) \right] \right\} + y_3 + \Delta l \tan\theta_3$$

$$= (\Delta l)^2 \left\{ \frac{\varepsilon_3 - \varepsilon_4}{2(c_3 - c_4)} - \frac{\varepsilon_3 c_4 - \varepsilon_4 c_3}{(c_3 - c_4)^3} \left[c_4 \log_e \frac{c_4}{c_3} + (c_3 - c_4) \right] \right\}$$

$$+ \overbrace{\left\{ \begin{array}{l} (\Delta l)^2 \left\{ \frac{\varepsilon_2 - \varepsilon_3}{2(c_2 - c_3)} - \frac{\varepsilon_2 c_3 - \varepsilon_3 c_2}{(c_2 - c_3)^3} \left[c_3 \log_e \frac{c_3}{c_2} + (c_2 - c_3) \right] + \frac{\varepsilon_1 - \varepsilon_2}{2(c_1 - c_2)} - \frac{\varepsilon_1 c_2 - \varepsilon_2 c_1}{(c_1 - c_2)^3} \left[c_2 \log_e \frac{c_2}{c_1} + (c_1 - c_2) \right] \right. \\ \left. \quad + \frac{\varepsilon_0 - \varepsilon_1}{2(c_0 - c_1)} - \frac{\varepsilon_0 c_1 - \varepsilon_1 c_0}{(c_0 - c_1)^3} \left[c_1 \log_e \frac{c_1}{c_0} + (c_0 - c_1) \right] \right\} + \\ + (\Delta l)^2 \left[\frac{\varepsilon_1 - \varepsilon_2}{c_1 - c_2} + \frac{\varepsilon_1 c_2 - \varepsilon_2 c_1}{(c_1 - c_2)^2} \log_e \frac{c_2}{c_1} + 2\frac{\varepsilon_0 - \varepsilon_1}{c_0 - c_1} + 2\frac{\varepsilon_0 c_1 - \varepsilon_1 c_0}{(c_0 - c_1)^2} \log_e \frac{c_1}{c_0} \right] + y_0 + 3\Delta l \tan\theta_0 \end{array} \right\}}^{y_3}$$

$$+ \overbrace{\left\{ \begin{array}{l} (\Delta l)^2 \left[\frac{\varepsilon_2 - \varepsilon_3}{c_2 - c_3} + \frac{\varepsilon_2 c_3 - \varepsilon_3 c_2}{(c_2 - c_3)^2} \log_e \frac{c_3}{c_2} + \frac{\varepsilon_1 - \varepsilon_2}{c_1 - c_2} + \frac{\varepsilon_1 c_2 - \varepsilon_2 c_1}{(c_1 - c_2)^2} \log_e \frac{c_2}{c_1} \right. \\ \left. \quad + \frac{\varepsilon_0 - \varepsilon_1}{c_0 - c_1} + \frac{\varepsilon_0 c_1 - \varepsilon_1 c_0}{(c_0 - c_1)^2} \log_e \frac{c_1}{c_0} \right] + \Delta l \tan\theta_0 \end{array} \right\}}^{\Delta l \tan\theta_3}$$

$$= (\Delta l)^2 \left\{ \frac{\varepsilon_3 - \varepsilon_4}{2(c_3 - c_4)} - \frac{\varepsilon_3 c_4 - \varepsilon_4 c_3}{(c_3 - c_4)^3} \left[c_4 \log_e \frac{c_4}{c_3} + (c_3 - c_4) \right] + \frac{\varepsilon_2 - \varepsilon_3}{2(c_2 - c_3)} - \frac{\varepsilon_2 c_3 - \varepsilon_3 c_2}{(c_2 - c_3)^3} \left[c_3 \log_e \frac{c_3}{c_2} + (c_2 - c_3) \right] \right.$$
$$\left. + \frac{\varepsilon_1 - \varepsilon_2}{2(c_1 - c_2)} - \frac{\varepsilon_1 c_2 - \varepsilon_2 c_1}{(c_1 - c_2)^3} \left[c_2 \log_e \frac{c_2}{c_1} + (c_1 - c_2) \right] + \frac{\varepsilon_0 - \varepsilon_1}{2(c_0 - c_1)} - \frac{\varepsilon_0 c_1 - \varepsilon_1 c_0}{(c_0 - c_1)^3} \left[c_1 \log_e \frac{c_1}{c_0} + (c_0 - c_1) \right] \right\}$$
$$+ (\Delta l)^2 \left[\frac{\varepsilon_2 - \varepsilon_3}{c_2 - c_3} + \frac{\varepsilon_2 c_3 - \varepsilon_3 c_2}{(c_2 - c_3)^2} \log_e \frac{c_3}{c_2} + 2\frac{\varepsilon_1 - \varepsilon_2}{c_1 - c_2} + 2\frac{\varepsilon_1 c_2 - \varepsilon_2 c_1}{(c_1 - c_2)^2} \log_e \frac{c_2}{c_1} + 3\frac{\varepsilon_0 - \varepsilon_1}{c_0 - c_1} + 3\frac{\varepsilon_0 c_1 - \varepsilon_1 c_0}{(c_0 - c_1)^2} \log_e \frac{c_1}{c_0} \right]$$
$$+ y_0 + 4\Delta l \tan\theta_0 \qquad \text{(A2-d)}$$

After the terms are grouped, equation (A2-d) becomes

$$
\begin{aligned}
y_4 = (\Delta l)^2 & \left[\frac{\varepsilon_3 - \varepsilon_4}{2(c_3 - c_4)} + 3\frac{\varepsilon_2 - \varepsilon_3}{2(c_2 - c_3)} + 5\frac{\varepsilon_1 - \varepsilon_2}{2(c_1 - c_2)} + 7\frac{\varepsilon_0 - \varepsilon_1}{2(c_0 - c_1)} \right] \\
& - (\Delta l)^2 \left\{ \frac{\varepsilon_3 c_4 - \varepsilon_4 c_3}{(c_3 - c_4)^3} \left[c_4 \log_e \frac{c_4}{c_3} + (c_3 - c_4) \right] + \frac{\varepsilon_2 c_3 - \varepsilon_3 c_2}{(c_2 - c_3)^3} \left[c_3 \log_e \frac{c_3}{c_2} + (c_2 - c_3) \right] \right. \\
& \qquad \left. + \frac{\varepsilon_1 c_2 - \varepsilon_2 c_1}{(c_1 - c_2)^3} \left[c_2 \log_e \frac{c_2}{c_1} + (c_1 - c_2) \right] + \frac{\varepsilon_0 c_1 - \varepsilon_1 c_0}{(c_0 - c_1)^3} \left[c_1 \log_e \frac{c_1}{c_0} + (c_0 - c_1) \right] \right\} \\
& + (\Delta l)^2 \left[\frac{\varepsilon_2 c_3 - \varepsilon_3 c_2}{(c_2 - c_3)^2} \log_e \frac{c_3}{c_2} + 2\frac{\varepsilon_1 c_2 - \varepsilon_2 c_1}{(c_1 - c_2)^2} \log_e \frac{c_2}{c_1} + 3\frac{\varepsilon_0 c_1 - \varepsilon_1 c_0}{(c_0 - c_1)^2} \log_e \frac{c_1}{c_0} \right] + y_0 + 4\Delta l \tan\theta_0
\end{aligned}
\qquad \text{(A2-d′)}
$$

Based on the indicial progression patterns in equations (A2-a)–(A2-d), the deflection, y_i, can be written in a generalized form with two summations (with different summation limits) as

$$
\begin{aligned}
y_i = (\Delta l)^2 & \sum_{j=1}^{i} \left\{ \frac{\varepsilon_{j-1} - \varepsilon_j}{2(c_{j-1} - c_j)} - \frac{\varepsilon_{j-1} c_j - \varepsilon_j c_{j-1}}{(c_{j-1} - c_j)^3} \left[c_j \log_e \frac{c_j}{c_{j-1}} + (c_{j-1} - c_j) \right] \right\} \\
& + (\Delta l)^2 \sum_{j=1}^{i-1} (i - j) \left[\frac{\varepsilon_{j-1} - \varepsilon_j}{c_{j-1} - c_j} + \frac{\varepsilon_{j-1} c_j - \varepsilon_j c_{j-1}}{(c_{j-1} - c_j)^2} \log_e \frac{c_j}{c_{j-1}} \right] + y_0 + (i)\Delta l \tan\theta_0
\end{aligned}
\qquad \text{(A2-e)}
$$

which is equation (15).

Alternatively, based on the progression of indices in equations (A2-a′)–(A2-d′), the generalized deflection equation can be rewritten in an alternative form as

$$
\begin{aligned}
y_i = (\Delta l)^2 & \sum_{j=1}^{i} \left\{ [2(i - j) + 1] \frac{\varepsilon_{j-1} - \varepsilon_j}{2(c_{j-1} - c_j)} - \frac{\varepsilon_{j-1} c_j - \varepsilon_j c_{j-1}}{(c_{j-1} - c_j)^3} \left[c_j \log_e \frac{c_j}{c_{j-1}} + (c_{j-1} - c_j) \right] \right\} \\
& + (\Delta l)^2 \sum_{j=1}^{i-1} (i - j) \left[\frac{\varepsilon_{j-1} c_j - \varepsilon_j c_{j-1}}{(c_{j-1} - c_j)^2} \log_e \frac{c_j}{c_{j-1}} \right] + y_0 + (i)\Delta l \tan\theta_0
\end{aligned}
\qquad \text{(A2-f)}
$$

which is equation (16).

The general deflection equation (A2-f) is checked for accuracy using $i = 4$ as follows:

$$
\begin{aligned}
y_4 = {} & (\Delta l)^2 \left\{ [2(4-1)+1] \frac{\varepsilon_{1-1} - \varepsilon_1}{2(c_{1-1} - c_1)} - \frac{\varepsilon_{1-1} c_1 - \varepsilon_1 c_{1-1}}{(c_{1-1} - c_1)^3} \left[c_1 \log_e \frac{c_1}{c_{1-1}} + (c_{1-1} - c_1) \right] \right\} \\
& + (\Delta l)^2 \left\{ [2(4-2)+1] \frac{\varepsilon_{2-1} - \varepsilon_2}{2(c_{2-1} - c_2)} - \frac{\varepsilon_{2-1} c_2 - \varepsilon_2 c_{2-1}}{(c_{2-1} - c_2)^3} \left[c_2 \log_e \frac{c_2}{c_{2-1}} + (c_{2-1} - c_2) \right] \right\} \\
& + (\Delta l)^2 \left\{ [2(4-3)+1] \frac{\varepsilon_{3-1} - \varepsilon_3}{2(c_{3-1} - c_3)} - \frac{\varepsilon_{3-1} c_2 - \varepsilon_3 c_{3-1}}{(c_{3-1} - c_2)^3} \left[c_3 \log_e \frac{c_3}{c_{3-1}} + (c_{3-1} - c_3) \right] \right\} \\
& + (\Delta l)^2 \left\{ [2(4-4)+1] \frac{\varepsilon_{4-1} - \varepsilon_4}{2(c_{4-1} - c_4)} - \frac{\varepsilon_{4-1} c_4 - \varepsilon_4 c_{4-1}}{(c_{4-1} - c_4)^3} \left[c_4 \log_e \frac{c_4}{c_{4-1}} + (c_{4-1} - c_4) \right] \right\} \\
& + 3(\Delta l)^2 \left[\frac{\varepsilon_{1-1} c_1 - \varepsilon_1 c_{1-1}}{(c_{1-1} - c_1)^2} \log_e \frac{c_1}{c_{1-1}} \right] + 2(\Delta l)^2 \left[\frac{\varepsilon_{2-1} c_2 - \varepsilon_2 c_{2-1}}{(c_{2-1} - c_2)^2} \log_e \frac{c_2}{c_{2-1}} \right] \\
& + (1)(\Delta l)^2 \left[\frac{\varepsilon_{3-1} c_3 - \varepsilon_3 c_{3-1}}{(c_{3-1} - c_3)^2} \log_e \frac{c_3}{c_{3-1}} \right] + y_0 + 4 \Delta l \tan \theta_0
\end{aligned}
$$

Finally,

$$
\begin{aligned}
y_4 = {} & (\Delta l)^2 \left[(1) \frac{\varepsilon_3 - \varepsilon_4}{2(c_3 - c_4)} + (3) \frac{\varepsilon_2 - \varepsilon_3}{2(c_2 - c_3)} + (5) \frac{\varepsilon_1 - \varepsilon_2}{2(c_1 - c_2)} + (7) \frac{\varepsilon_0 - \varepsilon_1}{2(c_0 - c_1)} \right] \\
& + (\Delta l)^2 \left\{ \frac{\varepsilon_0 c_1 - \varepsilon_1 c_0}{(c_0 - c_1)^3} \left[c_1 \log_e \frac{c_1}{c_0} + (c_0 - c_1) \right] + \frac{\varepsilon_1 c_2 - \varepsilon_2 c_1}{(c_1 - c_2)^3} \left[c_2 \log_e \frac{c_2}{c_1} + (c_1 - c_2) \right] \right. \\
& \qquad \left. + \frac{\varepsilon_2 c_2 - \varepsilon_3 c_2}{(c_2 - c_2)^3} \left[c_3 \log_e \frac{c_3}{c_2} + (c_2 - c_3) \right] + \frac{\varepsilon_3 c_4 - \varepsilon_4 c_3}{(c_3 - c_4)^3} \left[c_4 \log_e \frac{c_4}{c_3} + (c_3 - c_4) \right] \right\} \\
& + (\Delta l)^2 \left[3 \frac{\varepsilon_0 c_1 - \varepsilon_1 c_{1-1}}{(c_0 - c_1)^2} \log_e \frac{c_1}{c_0} + 2 \frac{\varepsilon_1 c_2 - \varepsilon_2 c_1}{(c_1 - c_2)^2} \log_e \frac{c_2}{c_1} + \frac{\varepsilon_2 c_3 - \varepsilon_3 c_2}{(c_2 - c_3)^2} \log_e \frac{c_3}{c_2} \right] \\
& + y_0 + 4 \Delta l \tan \theta_0
\end{aligned}
\qquad \text{(A3)}
$$

which agrees with equation (A2-d′).

APPENDIX B
EXPANSION OF LOGARITHMIC TERMS

This appendix discusses the mathematical processes of expanding the logarithmic terms (taken from Appendix E of reference 2).

When the cantilever beam is slightly tapered (that is, $c_i \to c_{i-1}$), the logarithmic terms in slope equation (14) and deflection equation (16) will approach zero (that is, $\log_e(c_i/c_{i-1}) \to 0$). Therefore, the perturbation method must be used to expand the logarithmic term, $\log_e(c_i/c_{i-1})$, in the neighborhood of $(c_i/c_{i-1}) \approx 1$ to yield nonzero mathematical expressions, which are derived in the following sections.

Expansion of $\log_e(c_i/c_{i-1})$ for Slope Equation

When the beam is slightly tapered (that is, $c_i \to c_{i-1}$), the logarithmic term, $\log_e(c_i/c_{i-1})$, can be expanded in the neighborhood of $(c_i/c_{i-1}) \approx 1$ (that is, $\log_e(c_i/c_{i-1}) \approx 0$) (ref. 6) as follows:

$$\log_e \frac{c_i}{c_{i-1}} \approx \left(\frac{c_i}{c_{i-1}} - 1\right) - \frac{1}{2}\left(\frac{c_i}{c_{i-1}} - 1\right)^2 + \frac{1}{3}\left(\frac{c_i}{c_{i-1}} - 1\right)^3 - \ldots.$$
$$\approx \frac{c_i - c_{i-1}}{c_{i-1}}\left[1 - \frac{c_i - c_{i-1}}{2c_{i-1}} + \frac{(c_i - c_{i-1})^2}{3c_{i-1}^2}\right] - \ldots. \quad ; \quad \frac{c_i}{c_{i-1}} \to 1 \tag{B1}$$

Carrying out the expansion and retaining up to the second-order terms in $(c_{i-1} - c_i)^2$ causes the logarithmic term, $\log_e(c_i/c_{i-1})$, to take on the following form when c_i approaches c_{i-1} ($c_i \to c_{i-1}$):

$$\log_e \frac{c_i}{c_{i-1}} \approx \frac{c_{i-1} - c_i}{2c_{i-1}^2}(c_i - 3c_{i-1}) \quad ; \quad \frac{c_i}{c_{i-1}} \to 1 \tag{B2}$$

Equation B2 is equation (17).

Expansion of $\left[c_i \log_e(c_i/c_{i-1}) + (c_{i-1} - c_i)\right]$ for Deflection Equation

When the beam is slightly tapered (that is, $c_i \to c_{i-1}$), the term, $\left[c_i \log_e(c_i/c_{i-1}) + (c_{i-1} - c_i)\right]$, in deflection equation (16) can be expanded in the neighborhood of $(c_i/c_{i-1}) \approx 1$ (that is, $\log_e(c_i/c_{i-1}) \approx 0$). In light of the $\log_e(c_i/c_{i-1})$ expansion equation (B1), the expansion, $\left[c_i \log_e(c_i/c_{i-1}) + (c_{i-1} - c_i)\right]$, can be carried out up to the third-order terms in $(c_{i-1} - c_i)^3$ when c_i approaches c_{i-1} ($c_i \to c_{i-1}$) (ref. 6) as

$$\left[c_i \log_e \frac{c_i}{c_{i-1}} + (c_{i-1} - c_i)\right] \approx c_i \left[\left(\frac{c_i}{c_{i-1}} - 1\right) - \frac{1}{2}\left(\frac{c_i}{c_{i-1}} - 1\right)^2 + \frac{1}{3}\left(\frac{c_i}{c_{i-1}} - 1\right)^3 - \ldots.\right] + (c_{i-1} - c_i)$$

$$\approx -\frac{c_i}{c_{i-1}}\left[(c_{i-1} - c_i) + \frac{(c_{i-1} - c_i)^2}{2c_{i-1}} + \frac{(c_{i-1} - c_i)^3}{3c_{i-1}^2} + \ldots. - \frac{c_{i-1}}{c_i}(c_{i-1} - c_i)\right]$$

$$\approx -\frac{c_i}{c_{i-1}}\left[(c_{i-1} - c_i)\left(1 - \frac{c_{i-1}}{c_i}\right) + \frac{(c_{i-1} - c_i)^2}{2c_{i-1}} + \frac{(c_{i-1} - c_i)^3}{3c_{i-1}^2} + \ldots.\right]$$

$$\approx -\frac{c_i}{c_{i-1}}\left[-\frac{(c_{i-1} - c_i)^2}{c_i} + \frac{(c_{i-1} - c_i)^2}{2c_{i-1}} + \frac{(c_{i-1} - c_i)^3}{3c_{i-1}^2} + \ldots.\right]$$

$$\approx -\frac{(c_{i-1} - c_i)^2}{6c_{i-1}}\left[-6 + 3\frac{c_i}{c_{i-1}} + 2\frac{c_i}{c_{i-1}^2}(c_{i-1} - c_i) + \ldots.\right]$$

$$\approx \frac{(c_{i-1} - c_i)^2}{6c_{i-1}}\left[3 + 3 - 3\frac{c_i}{c_{i-1}} - 2\frac{c_i}{c_{i-1}^2}(c_{i-1} - c_i) - \ldots.\right]$$

$$\approx \frac{(c_{i-1} - c_i)^2}{6c_{i-1}}\left[3 + 3\frac{(c_{i-1} - c_i)}{c_{i-1}} - 2\frac{c_i}{c_{i-1}^2}(c_{i-1} - c_i) - \ldots.\right]$$

$$\approx \frac{(c_{i-1} - c_i)^2}{6c_{i-1}}\left[3 + \frac{(c_{i-1} - c_i)}{c_{i-1}} + 2\frac{(c_{i-1} - c_i)}{c_{i-1}} - 2\frac{c_i}{c_{i-1}^2}(c_{i-1} - c_i) - \ldots.\right]$$

$$\approx \frac{(c_{i-1} - c_i)^2}{6c_{i-1}}\left[3 + \frac{(c_{i-1} - c_i)}{c_{i-1}} + 2\frac{(c_{i-1} - c_i)^2}{c_{i-1}^2} - \ldots.\right] \quad ; \quad \frac{c_i}{c_{i-1}} \to 1 \qquad \text{(B3)}$$

Neglecting the fourth-order term in $(c_{i-1}-c_i)^4$, we obtain the final expression for $\left[c_i \log_e(c_i/c_{i-1})+\left(c_{i-1}-c_i\right)\right]$ when c_i approaches c_{i-1} ($c_i \to c_{i-1}$) as

$$\left[\log_e \frac{c_i}{c_{i-1}}+(c_{i-1}-c_i)\right] \approx \frac{(c_{i-1}-c_i)^2}{6c_{i-1}}\left[3+\frac{(c_{i-1}-c_i)}{c_{i-1}}\right] \quad ; \quad \frac{c_i}{c_{i-1}} \to 1 \tag{B4}$$

which is equation (20).

APPENDIX C
DERIVATIONS OF DEFLECTION EQUATION FOR SLIGHTLY NONUNIFORM CANTILEVER BEAMS

Deflection equation (21) for the slightly nonuniform cantilever beam contains the slope term, $\Delta l \tan\theta_{i-1}$, as follows:

$$y_i = \frac{(\Delta l)^2}{6c_{i-1}}\left[\left(3-\frac{c_i}{c_{i-1}}\right)\varepsilon_{i-1}+\varepsilon_i\right]+y_{i-1}+\Delta l\tan\theta_{i-1} \tag{C1}$$

In light of equation (18), the slope, $\tan\theta_{i-1}$, can be written as

$$\tan\theta_{i-1} = \frac{\Delta l}{2c_{i-2}}\left[\left(2-\frac{c_{i-1}}{c_{i-2}}\right)\varepsilon_{i-2}+\varepsilon_{i-1}\right]+\tan\theta_{i-2} \tag{C2}$$

Writing out both equations (C1) and (C2) for different indices (i = 1, 2 , 3, 4, 5), we obtain

$$y_1 = \frac{(\Delta l)^2}{6c_0}\left[\left(3-\frac{c_1}{c_0}\right)\varepsilon_0+\varepsilon_1\right]+y_0+\Delta l\tan\theta_0 \quad ; \quad y_0=0 \ ; \ \Delta l\tan\theta_0=0 \tag{C3-a}$$

$$y_2 = \frac{(\Delta l)^2}{6c_1}\left[\left(3-\frac{c_2}{c_1}\right)\varepsilon_1+\varepsilon_2\right]+y_1+\Delta l\tan\theta_1 \quad ; \quad \tan\theta_1 = \frac{\Delta l}{2c_0}\left[\left(2-\frac{c_1}{c_0}\right)\varepsilon_0+\varepsilon_1\right]+\tan\theta_0 \tag{C3-b}$$

$$y_3 = \frac{(\Delta l)^2}{6c_2}\left[\left(3-\frac{c_3}{c_2}\right)\varepsilon_2+\varepsilon_3\right]+y_2+\Delta l\tan\theta_2 \quad ; \quad \tan\theta_2 = \frac{\Delta l}{2c_1}\left[\left(2-\frac{c_2}{c_1}\right)\varepsilon_1+\varepsilon_2\right]+\tan\theta_1 \tag{C3-c}$$

$$y_4 = \frac{(\Delta l)^2}{6c_3}\left[\left(3-\frac{c_4}{c_3}\right)\varepsilon_3+\varepsilon_4\right]+y_3+\Delta l\tan\theta_3 \quad ; \quad \tan\theta_3 = \frac{\Delta l}{2c_2}\left[\left(2-\frac{c_3}{c_2}\right)\varepsilon_2+\varepsilon_3\right]+\tan\theta_2 \tag{C3-d}$$

$$y_5 = \frac{(\Delta l)^2}{6c_4}\left[\left(3-\frac{c_5}{c_4}\right)\varepsilon_4+\varepsilon_5\right]+y_4+\Delta l\tan\theta_4 \quad ; \quad \tan\theta_4 = \frac{\Delta l}{2c_3}\left[\left(2-\frac{c_4}{c_3}\right)\varepsilon_3+\varepsilon_4\right]+\tan\theta_3 \tag{C3-e}$$

Based on equations (C3-a)–(C3-e), the deflection, y_i, can be rewritten for different values of i as follows:

For $i = 2$, equation (C3-b) becomes

$$y_2 = \frac{(\Delta l)^2}{6c_1}\left[\left(3-\frac{c_2}{c_1}\right)\varepsilon_1+\varepsilon_2\right]+y_1+\Delta l\tan\theta_1$$

$$= \frac{(\Delta l)^2}{6c_1}\left[\left(3-\frac{c_2}{c_1}\right)\varepsilon_1+\varepsilon_2\right]+\overbrace{\frac{(\Delta l)^2}{6c_0}\left[\left(3-\frac{c_1}{c_0}\right)\varepsilon_0+\varepsilon_1\right]+y_0+\Delta l\tan\theta_0}^{y_1}+\overbrace{\frac{(\Delta l)^2}{2c_0}\left[\left(2-\frac{c_1}{c_0}\right)\varepsilon_0+\varepsilon_1\right]+\Delta l\tan\theta_0}^{\Delta l\tan\theta_1}$$

$$= \frac{(\Delta l)^2}{6}\left\{\frac{1}{c_1}\left[\left(3-\frac{c_2}{c_1}\right)\varepsilon_1+\varepsilon_2\right]+\frac{1}{c_0}\left[\left(3-\frac{c_1}{c_0}\right)\varepsilon_0+\varepsilon_1\right]\right\}+\frac{(\Delta l)^2}{2c_0}\left[\left(2-\frac{c_1}{c_0}\right)\varepsilon_0+\varepsilon_1\right] \qquad \text{(C4-a)}$$
$$+ y_0 + 2\Delta l\tan\theta_0$$

$$= \frac{(\Delta l)^2}{6c}\left\{\frac{1}{c_1}\left[\left(3-\frac{c_2}{c_1}\right)\varepsilon_1+\varepsilon_2\right]+\frac{1}{c_0}\left[\left(9-4\frac{c_1}{c_0}\right)\varepsilon_0+4\varepsilon_1\right]\right\}+y_0+2\Delta l\tan\theta_0$$

(C4- a′)

For $i = 3$, equation (C3-c) becomes

$$y_3 = \frac{(\Delta l)^2}{6c_2}\left[\left(3-\frac{c_3}{c_2}\right)\varepsilon_2+\varepsilon_3\right]+y_2+\Delta l\tan\theta_2$$

$$= \frac{(\Delta l)^2}{6c_2}\left[\left(3-\frac{c_3}{c_2}\right)\varepsilon_2+\varepsilon_3\right]$$

$$+\overbrace{\frac{(\Delta l)^2}{6c_1}\left[\left(3-\frac{c_2}{c_1}\right)\varepsilon_1+\varepsilon_2\right]+\frac{(\Delta l)^2}{6c_0}\left[\left(3-\frac{c_1}{c_0}\right)\varepsilon_0+\varepsilon_1\right]+\frac{(\Delta l)^2}{2c_0}\left[\left(2-\frac{c_1}{c_0}\right)\varepsilon_0+\varepsilon_1\right]+y_0+2\Delta l\tan\theta_0}^{y_2}$$

$$+\overbrace{\frac{(\Delta l)^2}{2c_1}\left[\left(2-\frac{c_2}{c_1}\right)\varepsilon_1+\varepsilon_2\right]+\frac{(\Delta l)^2}{2c_0}\left[\left(2-\frac{c_1}{c_0}\right)\varepsilon_0+\varepsilon_1\right]+\Delta l\tan\theta_0}^{\Delta l\tan\theta_2}$$

$$= \frac{(\Delta l)^2}{6}\left\{\frac{1}{c_2}\left[\left(3-\frac{c_3}{c_2}\right)\varepsilon_2+\varepsilon_3\right]+\frac{1}{c_1}\left[\left(3-\frac{c_2}{c_1}\right)\varepsilon_1+\varepsilon_2\right]+\frac{1}{c_0}\left[\left(3-\frac{c_1}{c_0}\right)\varepsilon_0+\varepsilon_1\right]\right\}$$
$$+\frac{(\Delta l)^2}{2}\left\{\frac{1}{c_1}\left[\left(2-\frac{c_2}{c_1}\right)\varepsilon_1+\varepsilon_2\right]+2\frac{1}{c_0}\left[\left(2-\frac{c_1}{c_0}\right)\varepsilon_0+\varepsilon_1\right]\right\}+y_0+3\Delta l\tan\theta_0 \qquad \text{(C4-b)}$$

$$= \frac{(\Delta l)^2}{6}\left\{\frac{1}{c_2}\left[\left(3-\frac{c_3}{c_2}\right)\varepsilon_2+\varepsilon_3\right]+\frac{1}{c_1}\left[\left(9-4\frac{c_2}{c_1}\right)\varepsilon_1+4\varepsilon_2\right]+\frac{1}{c_0}\left[\left(15-7\frac{c_1}{c_0}\right)\varepsilon_0+7\varepsilon_1\right]\right\} \qquad \text{(C4- b′)}$$
$$+ y_0 + 3\Delta l\tan\theta_0$$

For $i = 4$, equation (C3-d) becomes

$$y_4 = \frac{(\Delta l)^2}{6c_3}\left[\left(3-\frac{c_4}{c_3}\right)\varepsilon_3+\varepsilon_4\right] + y_3 + \Delta l \tan\theta_3$$

$$= \frac{(\Delta l)^2}{6c_3}\left[\left(3-\frac{c_4}{c_3}\right)\varepsilon_3+\varepsilon_4\right]$$

$$+ \overbrace{\left\{\begin{array}{l}\dfrac{(\Delta l)^2}{6c_2}\left[\left(3-\dfrac{c_3}{c_2}\right)\varepsilon_2+\varepsilon_3\right]+\dfrac{(\Delta l)^2}{6c_1}\left[\left(3-\dfrac{c_2}{c_1}\right)\varepsilon_1+\varepsilon_2\right]+\dfrac{(\Delta l)^2}{6c_0}\left[\left(3-\dfrac{c_1}{c_0}\right)\varepsilon_0+\varepsilon_1\right] \\ \quad +\dfrac{(\Delta l)^2}{2c_1}\left[\left(2-\dfrac{c_2}{c_1}\right)\varepsilon_1+\varepsilon_2\right]+2\dfrac{(\Delta l)^2}{2c_0}\left[\left(2-\dfrac{c_1}{c_0}\right)\varepsilon_0+\varepsilon_1\right]+y_0+3\Delta l\tan\theta_0\end{array}\right\}}^{y_3}$$

$$+ \overbrace{\frac{(\Delta l)^2}{2c_2}\left[\left(2-\frac{c_3}{c_2}\right)\varepsilon_2+\varepsilon_3\right]+\frac{(\Delta l)^2}{2c_1}\left[\left(2-\frac{c_2}{c_1}\right)\varepsilon_1+\varepsilon_2\right]+\frac{(\Delta l)^2}{2c_0}\left[\left(2-\frac{c_1}{c_0}\right)\varepsilon_0+\varepsilon_1\right]+\Delta l\tan\theta_0}^{\Delta l\tan\theta_3}$$

$$\begin{aligned}= \frac{(\Delta l)^2}{6}&\left\{\frac{(\Delta l)^2}{6c_3}\left[\left(3-\frac{c_4}{c_3}\right)\varepsilon_3+\varepsilon_4\right]+\frac{(\Delta l)^2}{6c_2}\left[\left(3-\frac{c_3}{c_2}\right)\varepsilon_2+\varepsilon_3\right]+\frac{(\Delta l)^2}{6c_1}\left[\left(3-\frac{c_2}{c_1}\right)\varepsilon_1+\varepsilon_2\right]\right. \\ &\left.+\frac{(\Delta l)^2}{6c_0}\left[\left(3-\frac{c_1}{c_0}\right)\varepsilon_0+\varepsilon_1\right]\right\} \\ &+\frac{(\Delta l)^2}{2}\left\{\frac{1}{c_2}\left[\left(2-\frac{c_3}{c_2}\right)\varepsilon_2+\varepsilon_3\right]+\frac{2}{c_1}\left[\left(2-\frac{c_2}{c_1}\right)\varepsilon_1+\varepsilon_2\right]+\frac{3}{c_0}\left[\left(2-\frac{c_1}{c_0}\right)\varepsilon_0+\varepsilon_1\right]\right\} \\ &+y_0+4\Delta l\tan\theta_0\end{aligned} \qquad \text{(C4-c)}$$

$$\begin{aligned}= \frac{(\Delta l)^2}{6c_3}&\left\{\frac{1}{c_3}\left[\left(3-\frac{c_4}{c_3}\right)\varepsilon_3+\varepsilon_4\right]+\frac{1}{c_2}\left[\left(9-4\frac{c_3}{c_2}\right)\varepsilon_2+4\varepsilon_3\right]+\frac{1}{c_1}\left[\left(15-7\frac{c_2}{c_1}\right)\varepsilon_1+7\varepsilon_2\right]\right. \\ &\left.+\frac{1}{c_0}\left[\left(21-10\frac{c_1}{c_0}\right)\varepsilon_0+10\varepsilon_1\right]\right\}+y_0+4\Delta l\tan\theta_0\end{aligned} \qquad \text{(C4-c′)}$$

For $i = 5$, equation (C3-e) becomes

$$y_5 = \frac{(\Delta l)^2}{6c_4}\left[\left(3-\frac{c_5}{c_4}\right)\varepsilon_4+\varepsilon_5\right] + y_4 + \Delta l\tan\theta_4$$

$$= \frac{(\Delta l)^2}{6c_4}\left[\left(3-\frac{c_5}{c_4}\right)\varepsilon_4+\varepsilon_5\right]$$

$$+\overbrace{\left\{\begin{array}{l}\frac{(\Delta l)^2}{6c_3}\left[\left(3-\frac{c_4}{c_3}\right)\varepsilon_3+\varepsilon_4\right]+\frac{(\Delta l)^2}{6c_2}\left[\left(3-\frac{c_3}{c_2}\right)\varepsilon_2+\varepsilon_3\right]+\frac{(\Delta l)^2}{6c_1}\left[\left(3-\frac{c_2}{c_1}\right)\varepsilon_1+\varepsilon_2\right]\\ +\frac{(\Delta l)^2}{6c_0}\left[\left(3-\frac{c_1}{c_0}\right)\varepsilon_0+\varepsilon_1\right]+\frac{(\Delta l)^2}{2c_2}\left[\left(2-\frac{c_3}{c_2}\right)\varepsilon_2+\varepsilon_3\right]+2\frac{(\Delta l)^2}{2c_1}\left[\left(2-\frac{c_2}{c_1}\right)\varepsilon_1+\varepsilon_2\right]\\ +3\frac{(\Delta l)^2}{2c_0}\left[\left(2-\frac{c_1}{c_0}\right)\varepsilon_0+\varepsilon_1\right]+y_0+4\Delta l\tan\theta_0\end{array}\right\}}^{y_4}$$

$$+\overbrace{\left\{\begin{array}{l}\frac{(\Delta l)^2}{2c_3}\left[\left(2-\frac{c_4}{c_3}\right)\varepsilon_3+\varepsilon_4\right]+\frac{(\Delta l)^2}{2c_2}\left[\left(2-\frac{c_3}{c_2}\right)\varepsilon_2+\varepsilon_3\right]+\frac{(\Delta l)^2}{2c_1}\left[\left(2-\frac{c_2}{c_1}\right)\varepsilon_1+\varepsilon_2\right]\\ +\frac{(\Delta l)^2}{2c_0}\left[\left(2-\frac{c_1}{c_0}\right)\varepsilon_0+\varepsilon_1\right]+\Delta l\tan\theta_0\end{array}\right\}}^{\Delta l\tan\theta_4}$$

$$= \frac{(\Delta l)^2}{6}\left\{\frac{1}{c_4}\left[\left(3-\frac{c_5}{c_4}\right)\varepsilon_4+\varepsilon_5\right]\frac{1}{c_3}\left[\left(3-\frac{c_4}{c_3}\right)\varepsilon_3+\varepsilon_4\right]+\frac{1}{c_2}\left[\left(3-\frac{c_3}{c_2}\right)\varepsilon_2+\varepsilon_3\right]\right.$$
$$\left.+\frac{1}{c_1}\left[\left(3-\frac{c_2}{c_1}\right)\varepsilon_1+\varepsilon_2\right]+\frac{1}{c_0}\left[\left(3-\frac{c_1}{c_0}\right)\varepsilon_0+\varepsilon_1\right]\right\}$$
$$+\frac{(\Delta l)^2}{2}\left\{\frac{1}{c_3}\left[\left(2-\frac{c_4}{c_3}\right)\varepsilon_3+\varepsilon_4\right]+\frac{2}{c_2}\left[\left(2-\frac{c_3}{c_2}\right)\varepsilon_2+\varepsilon_3\right]+\frac{3}{c_1}\left[\left(2-\frac{c_2}{c_1}\right)\varepsilon_1+\varepsilon_2\right]\right.$$
$$\left.+\frac{4}{c_0}\left[\left(2-\frac{c_1}{c_0}\right)\varepsilon_0+\varepsilon_1\right]\right\}+y_0+5\Delta l\tan\theta_0 \qquad \text{(C4-d)}$$

$$= \frac{(\Delta l)^2}{6}\left\{\frac{1}{c_4}\left[\left(3-\frac{c_5}{c_4}\right)\varepsilon_4+\varepsilon_5\right]+\frac{1}{c_3}\left[\left(9-4\frac{c_4}{c_3}\right)\varepsilon_3+4\varepsilon_4\right]+\frac{1}{c_2}\left[\left(15-7\frac{c_3}{c_2}\right)\varepsilon_2+7\varepsilon_3\right]\right.$$
$$\left.+\frac{1}{c_1}\left[\left(21-10\frac{c_2}{c_1}\right)\varepsilon_1+10\varepsilon_2\right]+\frac{1}{c_0}\left[\left(27-13\frac{c_1}{c_0}\right)\varepsilon_0+13\varepsilon_1\right]\right\}+y_0+5\Delta l\tan\theta_0 \qquad \text{(C4-d′)}$$

In summary,

$$y_1 = \frac{(\Delta l)^2}{6c_0}\left[\left(3-\frac{c_1}{c_0}\right)\varepsilon_0+\varepsilon_1\right]+y_0+\Delta l\tan\theta_0 \tag{C5-a}$$

$$\begin{aligned} y_2 = {} & \frac{(\Delta l)^2}{6}\left\{\frac{1}{c_1}\left[\left(3-\frac{c_2}{c_1}\right)\varepsilon_1+\varepsilon_2\right]+\frac{1}{c_0}\left[\left(3-\frac{c_1}{c_0}\right)\varepsilon_0+\varepsilon_1\right]\right\} \\ & +\frac{(\Delta l)^2}{2c_0}\left[\left(2-\frac{c_1}{c_0}\right)\varepsilon_0+\varepsilon_1\right]+y_0+2\Delta l\tan\theta_0 \end{aligned} \tag{C5-b}$$

or,

$$y_2 = \frac{(\Delta l)^2}{6}\left\{\frac{1}{c_1}\left[\left(3-\frac{c_2}{c_1}\right)\varepsilon_1+\varepsilon_2\right]+\frac{1}{c_0}\left[\left(9-4\frac{c_1}{c_0}\right)\varepsilon_0+4\varepsilon_1\right]\right\}+y_0+2\Delta l\tan\theta_0 \tag{C5-b′}$$

$$\begin{aligned} y_3 = {} & \frac{(\Delta l)^2}{6}\left\{\frac{1}{c_2}\left[\left(3-\frac{c_3}{c_2}\right)\varepsilon_2+\varepsilon_3\right]+\frac{1}{c_1}\left[\left(3-\frac{c_2}{c_1}\right)\varepsilon_1+\varepsilon_2\right]+\frac{1}{c_0}\left[\left(3-\frac{c_1}{c_0}\right)\varepsilon_0+\varepsilon_1\right]\right\} \\ & +\frac{(\Delta l)^2}{2}\left\{\frac{1}{c_1}\left[\left(2-\frac{c_2}{c_1}\right)\varepsilon_1+\varepsilon_2\right]+\frac{2}{c_0}\left[\left(2-\frac{c_1}{c_0}\right)\varepsilon_0+\varepsilon_1\right]\right\}+y_0+3\Delta l\tan\theta_0 \end{aligned} \tag{C5-c}$$

or,

$$\begin{aligned} y_3 = {} & \frac{(\Delta l)^2}{6}\left\{\frac{1}{c_2}\left[\left(3-\frac{c_3}{c_2}\right)\varepsilon_2+\varepsilon_3\right]+\frac{1}{c_1}\left[\left(9-4\frac{c_2}{c_1}\right)\varepsilon_1+4\varepsilon_2\right]+\frac{1}{c_0}\left[\left(15-7\frac{c_1}{c_0}\right)\varepsilon_0+7\varepsilon_1\right]\right\} \\ & +y_0+3\Delta l\tan\theta_0 \end{aligned} \tag{C5-c′}$$

$$\begin{aligned} y_4 = {} & \frac{(\Delta l)^2}{6}\left\{\frac{1}{c_3}\left[\left(3-\frac{c_4}{c_3}\right)\varepsilon_3+\varepsilon_4\right]+\frac{1}{c_2}\left[\left(3-\frac{c_3}{c_2}\right)\varepsilon_2+\varepsilon_3\right]+\frac{1}{c_1}\left[\left(3-\frac{c_2}{c_1}\right)\varepsilon_1+\varepsilon_2\right]\right. \\ & \left.+\frac{1}{c_0}\left[\left(3-\frac{c_1}{c_0}\right)\varepsilon_0+\varepsilon_1\right]\right\} \\ & +\frac{(\Delta l)^2}{2}\left\{\frac{1}{c_2}\left[\left(2-\frac{c_3}{c_2}\right)\varepsilon_2+\varepsilon_3\right]+\frac{2}{c_1}\left[\left(2-\frac{c_2}{c_1}\right)\varepsilon_1+\varepsilon_2\right]+\frac{3}{c_0}\left[\left(2-\frac{c_1}{c_0}\right)\varepsilon_0+\varepsilon_1\right]\right\} \\ & +y_0+4\Delta l\tan\theta_0 \end{aligned} \tag{C5-d}$$

or,

$$y_4 = \frac{(\Delta l)^2}{6}\left\{\frac{1}{c_3}\left[\left(3-\frac{c_4}{c_3}\right)\varepsilon_3+\varepsilon_4\right]+\frac{1}{c_2}\left[\left(9-4\frac{c_3}{c_2}\right)\varepsilon_2+4\varepsilon_3\right]+\frac{1}{c_1}\left[\left(15-7\frac{c_2}{c_1}\right)\varepsilon_1+7\varepsilon_2\right]\right.$$
$$\left.+\frac{1}{c_0}\left[\left(21-10\frac{c_1}{c_0}\right)\varepsilon_0+10\varepsilon_1\right]\right\}+y_0+4\Delta l\tan\theta_0 \qquad \text{(C5-d}'\text{)}$$

$$y_5 = \frac{(\Delta l)^2}{6}\left\{\frac{1}{c_4}\left[\left(3-\frac{c_5}{c_4}\right)\varepsilon_4+\varepsilon_5\right]+\frac{1}{c_3}\left[\left(3-\frac{c_4}{c_3}\right)\varepsilon_3+\varepsilon_4\right]+\frac{1}{c_2}\left[\left(3-\frac{c_3}{c_2}\right)\varepsilon_2+\varepsilon_3\right]\right.$$
$$\left.+\frac{1}{c_1}\left[\left(3-\frac{c_2}{c_1}\right)\varepsilon_1+\varepsilon_2\right]+\frac{1}{c_0}\left[\left(3-\frac{c_1}{c_0}\right)\varepsilon_0+\varepsilon_1\right]\right\}$$
$$+\frac{(\Delta l)^2}{2}\left\{\frac{1}{c_3}\left[\left(2-\frac{c_4}{c_3}\right)\varepsilon_3+\varepsilon_4\right]+\frac{2}{c_2}\left[\left(2-\frac{c_3}{c_2}\right)\varepsilon_2+\varepsilon_3\right]+\frac{3}{c_1}\left[\left(2-\frac{c_2}{c_1}\right)\varepsilon_1+\varepsilon_2\right]\right. \qquad \text{(C5-e)}$$
$$\left.+\frac{4}{c_0}\left[\left(2-\frac{c_1}{c_0}\right)\varepsilon_0+\varepsilon_1\right]\right\}+y_0+5\Delta l\tan\theta$$

or,

$$y_5 = \frac{(\Delta l)^2}{6c_4}\left\{\frac{1}{c_4}\left[\left(3-\frac{c_5}{c_4}\right)\varepsilon_4+\varepsilon_5\right]+\frac{1}{c_3}\left[\left(9-4\frac{c_4}{c_3}\right)\varepsilon_3+4\varepsilon_4\right]+\frac{1}{c_2}\left[\left(15-7\frac{c_3}{c_2}\right)\varepsilon_2+7\varepsilon_3\right]\right.$$
$$\left.+\frac{1}{c_1}\left[\left(21-10\frac{c_2}{c_1}\right)\varepsilon_1+10\varepsilon_2\right]+\frac{1}{c_0}\left[\left(27-13\frac{c_1}{c_0}\right)\varepsilon_0+13\varepsilon_1\right]\right\}+y_0+5\Delta l\tan\theta_0 \qquad \text{(C5-e}'\text{)}$$

……

Observing the indicial behavior in equations (C5-a)–(C5-e), we can establish a generalized displacement equation for any index, i (= 1, 2, 3, …, n) as

$$y_i = \frac{(\Delta l)^2}{6}\sum_{j=1}^{i}\frac{1}{c_{j-1}}\left[\left(3-\frac{c_j}{c_{j-1}}\right)\varepsilon_{j-1}+\varepsilon_j\right]+\frac{(\Delta l)^2}{2}\sum_{j=1}^{i-1}\frac{(i-j)}{c_{j-1}}\left[\left(2-\frac{c_j}{c_{j-1}}\right)\varepsilon_{j-1}+\varepsilon_j\right]+y_0+i\Delta l\tan\theta_0 \qquad \text{(C5-f)}$$
$$(i = 1, 2, 3, \ldots, n)$$

which is deflection equation (22).

Also, based on the indicial behavior in equations (C5-b′)–(C5-e′), the generalized deflection equation can be written in a more compact form with single summation as

$$y_i = \frac{(\Delta l)^2}{6}\sum_{j=1}^{i}\frac{1}{c_{i-j}}\left\{\left[3(2j-1)-(3j-2)\frac{c_{i-j+1}}{c_{i-j}}\right]\varepsilon_{i-j}+(3j-2)\varepsilon_{i-j+1}\right\}+y_0+i\Delta l\tan\theta_0 \qquad (i=1,2,3,\ldots,n) \qquad \text{(C5-f′)}$$

which is deflection equation (23).

The general deflection equation (C5-f) is checked for correctness by using i = 4. For i = 4, equation (C5-f) becomes

$$\begin{aligned} y_4 &= \frac{(\Delta l)^2}{6}\sum_{j=1}^{4}\frac{1}{c_{j-1}}\left[\left(3-\frac{c_j}{c_{j-1}}\right)\varepsilon_{j-1}+\varepsilon_j\right]+\frac{(\Delta l)^2}{2}\sum_{j=1}^{4-1}\frac{(4-j)}{c_{j-1}}\left[\left(2-\frac{c_j}{c_{j-1}}\right)\varepsilon_{j-1}+\varepsilon_j\right]+y_0+4\Delta l\tan\theta_0 \\ &= \frac{(\Delta l)^2}{6}\left\{\frac{1}{c_3}\left[\left(3-\frac{c_4}{c_3}\right)\varepsilon_3+\varepsilon_4\right]\frac{1}{c_2}\left[\left(3-\frac{c_3}{c_2}\right)\varepsilon_2+\varepsilon_3\right]+\frac{1}{c_1}\left[\left(3-\frac{c_2}{c_1}\right)\varepsilon_1+\varepsilon_2\right]+\frac{1}{c_0}\left[\left(3-\frac{c_1}{c_0}\right)\varepsilon_0+\varepsilon_1\right]\right\} \\ &\quad +\frac{(\Delta l)^2}{2}\left\{\frac{1}{c_2}\left[\left(2-\frac{c_3}{c_2}\right)\varepsilon_2+\varepsilon_3\right]+\frac{2}{c_1}\left[\left(2-\frac{c_2}{c_1}\right)\varepsilon_1+\varepsilon_2\right]+\frac{3}{c_0}\left[\left(2-\frac{c_1}{c_0}\right)\varepsilon_0+\varepsilon_1\right]\right\}+y_0+4\Delta l\tan\theta_0 \end{aligned} \qquad \text{(C6)}$$

which agrees perfectly with equation (C5-d) and thus confirms the accuracy of general deflection equation (C5-f).

Likewise, the alternative general deflection equation (C5-f′) is also checked for accuracy by using i = 4. For i = 4, equation (C5-f′) becomes

$$\begin{aligned} y_4 &= \frac{(\Delta l)^2}{6}\sum_{j=1}^{4}\frac{1}{c_{4-j}}\left\{\left[3(2j-1)-(3j-2)\frac{c_{4-j+1}}{c_{4-j}}\right]\varepsilon_{4-j}+(3j-2)\varepsilon_{4-j+1}\right\}+y_0+4\Delta l\tan\theta_0 \\ &= \frac{(\Delta l)^2}{6}\left\{\frac{1}{c_3}\left[\left(3-\frac{c_4}{c_3}\right)\varepsilon_3+\varepsilon_4\right]+\frac{1}{c_2}\left[\left(9-4\frac{c_3}{c_2}\right)\varepsilon_2+4\varepsilon_3\right]+\frac{1}{c_1}\left[\left(15-7\frac{c_2}{c_1}\right)\varepsilon_1+7\varepsilon_2\right]\right. \\ &\quad \left.+\frac{1}{c_0}\left[\left(21-10\frac{c_1}{c_0}\right)\varepsilon_0+10\varepsilon_1\right]\right\}+y_0+4\Delta l\tan\theta_0 \end{aligned} \qquad \text{(C7)}$$

which agrees with equation (C5-d′) and thus confirms the accuracy of the alternative general deflection equation (C5-d′).

APPENDIX D
DERIVATIONS OF DEFLECTION EQUATIONS FOR UNIFORM CANTILEVER BEAMS

When the nonuniformity of the beam diminishes (that is, $c_i = c_{i-1} = c$, as in the uniform cantilever beam case), slope equations (18) and (19) degenerate into the following forms:

$$\tan\theta_i = \frac{\Delta l}{2c}(\varepsilon_{i-1} + \varepsilon_i) + \tan\theta_{i-1} \tag{D1}$$

$$\tan\theta_i = \frac{\Delta l}{2c}\sum_{j=1}^{i}(\varepsilon_{j-1} + \varepsilon_j) + \tan\theta_0 \tag{D2}$$

Furthermore, deflection equations (21) and (23) take on the following forms:

$$y_i = \frac{(\Delta l)^2}{6c}(2\varepsilon_{i-1} + \varepsilon_i) + y_{i-1} + \Delta l\tan\theta_{i-1} \tag{D3}$$

$$y_i = \frac{(\Delta l)^2}{6c}\sum_{j=1}^{i}\left[(3j-1)\varepsilon_{i-j} + (3j-2)\varepsilon_{i-j+1}\right] + y_0 + i\Delta l\tan\theta_0 \qquad (i = 1, 2, 3, \ldots, n) \quad ; \quad \tan\theta_0 = 0 \tag{D4}$$

Writing out equation (D4) for indices, i = 1–5, we obtain

$$y_1 = \frac{(\Delta l)^2}{6c}(2\varepsilon_0 + \varepsilon_1) + y_0 + \Delta l\tan\theta_0 \tag{D4-a}$$

$$\begin{aligned} y_2 &= \frac{(\Delta l)^2}{6c}\left[(3-1)\varepsilon_{2-1} + (3-2)\varepsilon_{2-1+1} + (3\times 2-1)\varepsilon_{2-2} + (3\times 2-2)\varepsilon_{2-2+1}\right] \\ &\quad + y_0 + 2\Delta l\tan\theta_0 \\ &= \frac{(\Delta l)^2}{6c}\left(2\varepsilon_1 + \varepsilon_2 + 5\varepsilon_0 + 4\varepsilon_1\right) + y_0 + 2\Delta l\tan\theta_0 \\ &= \frac{(\Delta l)^2}{6c}\left(5\varepsilon_0 + 6\varepsilon_1 + +\varepsilon_2\right) + y_0 + 2\Delta l\tan\theta_0 \end{aligned} \tag{D4-b}$$

$$y_3 = \frac{(\Delta l)^2}{6c}\left\{\begin{array}{l}\left[(3-1)\varepsilon_{3-1} + (3-2)\varepsilon_{3-1+1}\right] + \left[(3\times 2-1)\varepsilon_{3-2} + (3\times 2-2)\varepsilon_{3-2+1}\right] \\ + \left[(3\times 3-1)\varepsilon_{3-3} + (3\times 3-2)\varepsilon_{3-3+1}\right]\end{array}\right\}$$
$$+ y_0 + 3\Delta l \tan\theta_0$$
$$= \frac{(\Delta l)^2}{6c}\left[\left(2\varepsilon_2 + \varepsilon_3\right) + \left(5\varepsilon_1 + 4\varepsilon_2\right) + \left(8\varepsilon_0 + 7\varepsilon_1\right)\right] + y_0 + 3\Delta l \tan\theta_0$$
$$= \frac{(\Delta l)^2}{6c}\left(8\varepsilon_0 + 12\varepsilon_1 + +6\varepsilon_2 + \varepsilon_3\right) + y_0 + 3\Delta l \tan\theta_0$$
$$= \frac{(\Delta l)^2}{6c}\left[8\varepsilon_0 + 6(2\varepsilon_1 + \varepsilon_2) + \varepsilon_3\right] + y_0 + 3\Delta l \tan\theta_0 \qquad \text{(D4-c)}$$

$$y_4 = \frac{(\Delta l)^2}{6c}\left\{\left[(3-1)\varepsilon_{4-1} + (3-2)\varepsilon_{4-1+1}\right] + \left[(3\times 2-1)\varepsilon_{4-2} + (3\times 2-2)\varepsilon_{4-2+1}\right]\right.$$
$$\left. + \left[(3\times 3-1)\varepsilon_{4-3} + (3\times 3-2)\varepsilon_{4-3+1}\right] + \left[(3\times 4-1)\varepsilon_{4-4} + (3\times 4-2)\varepsilon_{4-4+1}\right]\right\}$$
$$+ y_0 + 4\Delta l \tan\theta_0$$
$$= \frac{(\Delta l)^2}{6c}\left[\left(2\varepsilon_3 + \varepsilon_4\right) + \left(5\varepsilon_2 + 4\varepsilon_3\right) + \left(8\varepsilon_1 + 7\varepsilon_2\right) + \left(11\varepsilon_0 + 10\varepsilon_1\right)\right] + y_0 + 4\Delta l \tan\theta_0$$
$$= \frac{(\Delta l)^2}{6c}\left(11\varepsilon_0 + 18\varepsilon_1 + 12\varepsilon_2 + 6\varepsilon_3 + \varepsilon_4\right) + y_0 + 4\Delta l \tan\theta_0$$
$$= \frac{(\Delta l)^2}{6c}\left[11\varepsilon_0 + 6\left(3\varepsilon_1 + 2\varepsilon_2 + \varepsilon_3\right) + \varepsilon_4\right] + y_0 + 4\Delta l \tan\theta_0 \qquad \text{(D4-d)}$$

$$y_5 = \frac{(\Delta l)^2}{6c}\left\{\left[(3-1)\varepsilon_{5-1} + (3-2)\varepsilon_{5-1+1}\right] + \left[(3\times 2-1)\varepsilon_{5-2} + (3\times 2-2)\varepsilon_{5-2+1}\right]\right.$$
$$+ \left[(3\times 3-1)\varepsilon_{5-3} + (3\times 3-2)\varepsilon_{5-3+1}\right] + \left[(3\times 4-1)\varepsilon_{5-4} + (3\times 4-2)\varepsilon_{5-4+1}\right]$$
$$\left. + \left[(3\times 5-1)\varepsilon_{5-5} + (3\times 5-2)\varepsilon_{5-5+1}\right]\right\} + y_0 + 5\Delta l \tan\theta_0$$
$$= \frac{(\Delta l)^2}{6c}\left[\left(2\varepsilon_4 + \varepsilon_5\right) + \left(5\varepsilon_3 + 4\varepsilon_4\right) + \left(8\varepsilon_2 + 7\varepsilon_3\right) + \left(11\varepsilon_1 + 10\varepsilon_2\right) + \left(14\varepsilon_0 + 13\varepsilon_1\right)\right]$$
$$+ y_0 + 5\Delta l \tan\theta_0$$
$$= \frac{(\Delta l)^2}{6c}\left(14\varepsilon_0 + 24\varepsilon_1 + 18\varepsilon_2 + 12\varepsilon_3 + 6\varepsilon_4\right) + y_0 + 5\Delta l \tan\theta_0$$
$$= \frac{(\Delta l)^2}{6c}\left[14\varepsilon_0 + 6\left(4\varepsilon_1 + 3\varepsilon_2 + 2\varepsilon_3 + \varepsilon_4\right) + \varepsilon_5\right] + y_0 + 5\Delta l \tan\theta_0 \qquad \text{(D4-e)}$$

Based on these indicial progressions, deflection equations (D4-a)–(D4-e) can be written in generalized forms for the indices, i, as

$$y_i = \frac{(\Delta l)^2}{6c}\left[(3i-1)\varepsilon_0 + 6\sum_{j=1}^{i-1}(i-j)\varepsilon_j + \varepsilon_i\right] + y_0 + i\Delta l\tan\theta_0 \qquad \text{(D4-f)}$$

which is identical to equation (28).

APPENDIX E
RELATIVE MAGNITUDES OF STRAIN TERMS FOR UNIFORM CANTILEVER BEAMS

For the study of relative magnitudes of the strain terms in uniform beam deflection equation (28), beam tip deflection equation (28f), duplicated as follows, is used:

$$y_n = \frac{(\Delta l)^2}{6c}\left[(3n-1)\varepsilon_0 + 6\sum_{j=1}^{n-1}(n-j)\varepsilon_j + \varepsilon_n\right] + y_0 + n\Delta l \tan\theta_0 \tag{E1}$$

The classical case of a uniform cantilever beam of a length, l, subjected to a tip vertical load, P, is considered in the analysis. For this case, the bending strain, $\varepsilon(x)$, is a linearly decreasing function of x, with a maximum at the fixed end and zero at the free end according to the expression

$$\varepsilon(x) = \left(1 - \frac{x}{l}\right)\varepsilon_0 \tag{E2}$$

in which ε_0 is the maximum bending strain at the built-in end.

The beam tip deflection, y_n, for different values of n (= 1, 2, 4, 8) are provided in the remainder of this appendix.

For n = 1, the strain at the beam tip is $\varepsilon_1 = 0 \times \varepsilon_0$, and equation (E1) yields

$$\begin{aligned} y_1 &= \frac{(\Delta l)^2}{6c}(2\varepsilon_0 + \varepsilon_1) = \frac{l^2}{3c}(1+0)\varepsilon_0 \\ &= \frac{l^2}{3c}\varepsilon_0 = \frac{l^2}{3c}\frac{M(0)c}{EI} = \frac{l^2}{3c}\frac{(Pl)c}{EI} = \frac{Pl^3}{3EI} \end{aligned} \tag{E3}$$

in which the strain, ε_0, is expressed in terms of the moment, $M(0)$, using the strain-moment relationship (eq. (4)).

For n = 2, the strains at strain-sensing stations, i = 1–2, are $\varepsilon_1 = \frac{1}{2}\varepsilon_0$, $\varepsilon_2 = \frac{0}{2}\varepsilon_0$, and equation (E1) yields

$$\begin{aligned} y_2 &= \frac{(\Delta l)^2}{6c}\left(5\varepsilon_0 + 6\varepsilon_1 + +\varepsilon_2\right) = \frac{1}{6c}\left(\frac{l^2}{2^2}\right)\left(5\varepsilon_0 + 6\frac{1}{2}\varepsilon_0 + \frac{0}{2}\varepsilon_0\right) \\ &= \frac{l^2}{3c}\varepsilon_0\left(\underbrace{0.625}_{\text{maximum}} + 0.375 + 0\right) \\ &= \frac{l^2}{3c}\varepsilon_0(1) = \frac{Pl^3}{3EI} \end{aligned} \tag{E4}$$

For n = 4, the strains at strain-sensing stations, i = 1–4, are $\varepsilon_1 = \frac{3}{4}\varepsilon_0,\ \varepsilon_2 = \frac{2}{4}\varepsilon_0,\ \varepsilon_3 = \frac{1}{4}\varepsilon_0, \varepsilon_4 = \frac{0}{4}\varepsilon_0,$ and equation (E1) yields

$$
\begin{aligned}
y_4 &= \frac{(\Delta l)^2}{6c}\left[11\varepsilon_0 + 6\left(3\varepsilon_1 + 2\varepsilon_2 + \varepsilon_3\right) + \varepsilon_4\right] \\
&= \frac{1}{6c}\left(\frac{l^2}{4^2}\right)\left[11\varepsilon_0 + 6\left(3\frac{3}{4}\varepsilon_0 + 2\frac{2}{4}\varepsilon_0 + \frac{1}{4}\varepsilon_0\right) + \frac{0}{4}\varepsilon_0\right] \\
&= \frac{l^2}{3c}\varepsilon_0\left(0.34375 + \underbrace{0.421875}_{\text{maximum}} + 0.1875 + 0.046875 + 0\right) \\
&= \frac{l^2}{3c}\varepsilon_0(1) = \frac{Pl^3}{3EI}
\end{aligned}
\tag{E5}
$$

For n = 8, the strains at strain-sensing stations, i = 1–8, are $\varepsilon_1 = \frac{7}{8}\varepsilon_0,\ \varepsilon_2 = \frac{6}{8}\varepsilon_0,\ \varepsilon_3 = \frac{5}{8}\varepsilon_0,\ \varepsilon_4 = \frac{4}{8}\varepsilon_0,$ $\varepsilon_5 = \frac{3}{8}\varepsilon_0,\ \varepsilon_6 = \frac{2}{8}\varepsilon_0,\ \varepsilon_7 = \frac{1}{8}\varepsilon_0,\ \varepsilon_8 = \frac{0}{8}\varepsilon_0$, and equation (E1) yields

$$
\begin{aligned}
y_8 &= \frac{(\Delta l)^2}{6c}\left[23\varepsilon_0 + 6\left(7\varepsilon_1 + 6\varepsilon_2 + 5\varepsilon_3 + 4\varepsilon_4 + 3\varepsilon_5 + 2\varepsilon_6 + \varepsilon_7\right) + \varepsilon_8\right] \\
&= \frac{1}{6c}\left(\frac{l^2}{8^2}\right)\left[23\varepsilon_0 + 6\left(7\frac{7}{8}\varepsilon_0 + 6\frac{6}{8}\varepsilon_0 + 5\frac{5}{8}\varepsilon_0 + 4\frac{4}{8}\varepsilon_0 + 3\frac{3}{8}\varepsilon_0 + 2\frac{2}{8}\varepsilon_0 + 1\frac{1}{8}\varepsilon_0\right) + \frac{0}{8}\varepsilon_0\right] \\
&= \frac{l^2}{3c}\varepsilon_0\left(0.17969 + \underbrace{0.28711}_{\text{maximum}} + 0.21094 + 0.14648 + 0.09375 + 0.05273 + 0.02344 + 0.00586 + 0\right) \\
&= \frac{l^2}{3c}\varepsilon_0(1) = \frac{Pl^3}{3EI}
\end{aligned}
\tag{E6}
$$

REFERENCES

1. DeAngelis, V. Michael, and Robert Fodale, "Electro-Optical Flight Deflection Measurement System," *Society of Flight Test Engineers 18th Annual Symposium*, Paper No. 22, Amsterdam, Netherlands, Sept. 1987.

2. Ko, William L., W. L. Richards, and Van T. Tran, *Displacement Theories for In-Flight Deformed Shape Predictions of Aerospace Structures*, NASA/TP-2007-214612, 2007.

3. Ko, William L., and William Lance Richards, *Method for Real-Time Structure Shape-Sensing,* U.S. Patent No. 7,520,176, issued April 21, 2009.

4. Roark, Raymond J., *Formulas for Stress and Strain*, Third Edition, McGraw-Hill Book Company, Inc., New York, 1954.

5. Faupel, Joseph, H., *Engineering Design: A Synthesis of Stress Analysis and Materials Engineering,* John Wiley and Sons, Inc., New York, 1964.

6. Hodgman, Charles D., *Standard Mathematical Tables*, Eleventh Edition, Chemical Rubber Publishing Company, Cleveland, Ohio, 1957.

7. Whetstone, W.D., *SPAR Structural Analysis System Reference Manual*, System Level 13A,Vol. 1, Program Execution, NASA CR-158970-1, 1978.

REPORT DOCUMENTATION PAGE

Form Approved
OMB No. 0704-0188

1. REPORT DATE *(DD-MM-YYYY)*	2. REPORT TYPE	3. DATES COVERED *(From - To)*
01-09-2009	Technical Publication	

4. TITLE AND SUBTITLE
Further Development of Ko Displacement Theory for Deformed Shape Predictions of Nonuniform Aerospace Structures

5a. CONTRACT NUMBER

5b. GRANT NUMBER

5c. PROGRAM ELEMENT NUMBER

6. AUTHOR(S)
William L. Ko and Van Tran Fleischer

5d. PROJECT NUMBER

5e. TASK NUMBER

5f. WORK UNIT NUMBER

7. PERFORMING ORGANIZATION NAME(S) AND ADDRESS(ES)
NASA Dryden Flight Research Center
P.O. Box 273
Edwards, California 93523-0273

8. PERFORMING ORGANIZATION REPORT NUMBER
H-2889

9. SPONSORING/MONITORING AGENCY NAME(S) AND ADDRESS(ES)
National Aeronautics and Space Administration
Washington, DC 20546-0001

10. SPONSORING/MONITOR'S ACRONYM(S)
NASA

11. SPONSORING/MONITORING REPORT NUMBER
NASA/TP-2009-214643

12. DISTRIBUTION/AVAILABILITY STATEMENT
Unclassified -- Unlimited
Subject Category 39 Availability: NASA CASI (443) 757-5802 Distribution: Standard

13. SUPPLEMENTARY NOTES
Ko and Fleischer, NASA Dryden Flight Research Center.

14. ABSTRACT

The Ko displacement theory previously formulated for deformed shape predictions of nonuniform beam structures is further developed mathematically. The further-developed displacement equations are expressed explicitly in terms of geometrical parameters of the beam and bending strains at equally spaced strain-sensing stations along the multiplexed fiber-optic sensor line installed on the bottom surface of the beam. The bending strain data can then be input into the displacement equations for calculations of local slopes, deflections, and cross-sectional twist angles for generating the overall deformed shapes of the nonuniform beam. The further-developed displacement theory can also be applied to the deformed shape predictions of nonuniform two-point supported beams, nonuniform panels, nonuniform aircraft wings and fuselages, and so forth. The high degree of accuracy of the further-developed displacement theory for nonuniform beams is validated by finite-element analysis of various nonuniform beam structures. Such structures include tapered tubular beams, depth-tapered unswept and swept wing boxes, width-tapered wing boxes, and double-tapered wing boxes, all under combined bending and torsional loads. The Ko displacement theory, combined with the fiber-optic strain-sensing system, provide a powerful tool for in-flight deformed shape monitoring of unmanned aerospace vehicles by ground-based pilots to maintain safe flights.

15. SUBJECT TERMS
Deflection equations, Displacement theories, Embedded strain sensing, In-flight shape predictions, Slope equations

16. SECURITY CLASSIFICATION OF:			17. LIMITATION OF ABSTRACT	18. NUMBER OF PAGES	19b. NAME OF RESPONSIBLE PERSON
a. REPORT	b. ABSTRACT	c. THIS PAGE			STI Help Desk (email:help@sti.nasa.gov)
					19b. TELEPHONE NUMBER *(Include area code)*
U	U	U	UU	86	(443) 757-5802